CENTER FOR GEOTECHNICAL MODELING

PM4SAND (VERSION 3.3): A SAND PLASTICITY MODEL FOR EARTHQUAKE ENGINEERING APPLICATIONS

BY

R. W. BOULANGER

K. ZIOTOPOULOU

UCDAVIS

DEPARTMENT OF CIVIL & ENVIRONMENTAL ENGINEERING
COLLEGE OF ENGINEERING
UNIVERSITY OF CALIFORNIA AT DAVIS

June 2023

PM4Sand (Version 3.3):
A Sand Plasticity Model for Earthquake Engineering Applications

by

Ross W. Boulanger

and

Katerina Ziotopoulou

Report No. UCD/CGM-23/01

Center for Geotechnical Modeling
Department of Civil and Environmental Engineering
University of California
Davis, California

June 2023

First Edition (PM4Sand Version 1) June 2010

Second Edition (PM4Sand Version 2) May 2012

      Revised July 2012

Third Edition (PM4Sand Version 3) March 2015

      Revised (PM4Sand Version 3.1) October 2017

      Revised January 2018

      Revised March 2018

      Revised July 2018

      Revised September 2018

      Revised (PM4Sand Version 3.2) July 2022

      Revised (PM4Sand Version 3.3) June 2023
            Compiled as *modelpm4sand005_64.dll* for FLAC 8.1 (Itasca 2019)
            Compiled as *cmodelPM4Sand2D009.dll* for FLAC2D 9.00 (Itasca 2023)

ABSTRACT

The sand plasticity model PM4Sand for geotechnical earthquake engineering applications is presented. The model follows the basic framework of the stress ratio-controlled, critical state-based, bounding surface plasticity model for sand presented by Dafalias and Manzari (2004). Modifications to the model were developed and implemented by Boulanger (2010, Version 1), Boulanger and Ziotopoulou (2012, Version 2), Boulanger and Ziotopoulou (2015, Version 3; 2017, Version 3.1; 2022, Version 3.2) and further herein (Version 3.3) to improve its ability to approximate the stress-strain responses important to geotechnical earthquake engineering applications; in essence, the model was calibrated at the equation level to provide for better approximation of the trends observed across a set of experimentally- and case history-based design correlations. These constitutive modifications included: revising the fabric formation/destruction to depend on plastic shear rather than plastic volumetric strains; adding fabric history and cumulative fabric formation terms; modifying the plastic modulus relationship and making it dependent on fabric; modifying the dilatancy relationships to include dependence on fabric and fabric history, and to provide more distinct control of volumetric contraction versus expansion behavior; providing a constraint on the dilatancy during volumetric expansion so that it is consistent with Bolton's (1986) dilatancy relationship; modifying the elastic modulus relationship to include dependence on stress ratio and fabric history; modifying the logic for tracking previous initial back-stress ratios (i.e., loading history effect); recasting the critical state framework to be in terms of a relative state parameter index; simplifying the formulation by restraining it to plane strain without Lode angle dependency for the bounding and dilatancy surfaces; incorporating a methodology for improved modeling of post-liquefaction reconsolidation strains; and providing default values for all but three primary input parameters. The model is coded as a user defined material in a dynamic link library (DLL) for use with the commercial program FLAC 8.1 (Itasca 2019) and FLAC2D 9.00 (Itasca 2023). The numerical implementation and DLL module are described. The behavior of the model is illustrated by simulations of element loading tests covering a broad range of conditions, including drained and undrained, cyclic, and monotonic loading under a range of initial confining and shear stress conditions, which can then be compared to typical design relationships. The model is shown to provide reasonable approximations of desired behaviors and to be relatively easy to calibrate.

TABLE OF CONTENTS

PM4Sand (Version 3.3):
A Sand Plasticity Model for Earthquake Engineering Applications

1. INTRODUCTION

Nonlinear deformation analyses for problems involving liquefaction are increasingly common in earthquake engineering practice. Constitutive models for sand that have been used in practice range from relatively simplified, uncoupled cycle-counting models to more complex plasticity models (e.g., Wang et al. 1990, Cubrinovski and Ishihara 1998, Dawson et al. 2001, Papadimitriou et al. 2001, Yang et al. 2003, Byrne et al. 2004, Dafalias and Manzari 2004, Tasiopoulou and Gerolymos 2016, Khosravifar et al. 2018, Liu et al. 2020, Yang et al. 2022). Each constitutive model has certain advantages and limitations that can be illustrated for potential users by documents showing the constitutive response of the model in element tests that cover a broad range of the conditions that may be important to various applications in practice (e.g., Beaty 2009). Considerations in selecting and calibrating constitutive models for nonlinear dynamic analyses and the documentation of results are discussed in Boulanger and Beaty (2016), Boulanger and Ziotopoulou (2018), and Boulanger 2022).

The information available for the calibration of constitutive models in design practice most commonly includes basic classification index tests (e.g., grain size distributions), penetration resistances (e.g., SPT or CPT), and shear wave velocity (V_s) measurements. More detailed laboratory tests, such as triaxial or direct simple shear tests, are almost never available due to the problems with overcoming sampling disturbance effects and the challenge of identifying representative samples from highly heterogeneous deposits.

Constitutive models for geotechnical earthquake engineering applications must be able to approximate a broad mix of conditions in the field. For example, a single geotechnical structure like the schematic earth dam shown in Figure 1.1 can have strata or zones of sand ranging from very loose to dense under a wide range of confining stresses, initial static shear stresses (e.g., at different points beneath the slope), drainage conditions (e.g., above and below the water table), and loading conditions (e.g., various levels of shaking). The engineering effort is greatly reduced if the constitutive model can reasonably approximate the predicted stress-strain behaviors under all these different conditions. If the model cannot approximate the trends across all these conditions, then extra engineering effort is required in deciding what behaviors should be prioritized in the calibration process, and sometimes by the need to repeat the calibrations for the effects of different initial stress conditions within the same geotechnical structure.

The PM4Sand (Version 3.3) plasticity model for geotechnical earthquake engineering applications is presented herein. The PM4Sand model follows the basic framework of the stress ratio-controlled, critical state-based, bounding surface plasticity model for sand initially presented by Manzari and Dafalias (1997) and later extended by Dafalias and Manzari (2004). Modifications to the Dafalias-Manzari model were developed and implemented to improve its ability to approximate engineering design relationships that are used to estimate the stress-strain behaviors that are important to predicting liquefaction-induced ground deformations during earthquakes. These developments are described in the manuals (Version 1 in Boulanger 2010, Version 2 in Boulanger and Ziotopoulou 2012, Version 3 in Boulanger and Ziotopoulou 2015, Version 3.1 in Boulanger and Ziotopoulou 2017, Version 3.2 in

Boulanger and Ziotopoulo 2022, and Version 3.3 herein) and associated publications (Boulanger and Ziotopoulou 2013, Ziotopoulou and Boulanger 2013a, Ziotopoulou 2014, Ziotopoulou and Boulanger 2016). The model is coded as a dynamic link library (DLL) for use with the commercial program FLAC 8.1 (Itasca 2019) and FLAC2D 9.00 (Itasca 2023).

It is unlikely that any one model can be developed or calibrated to simultaneously fit a full set of applicable design correlations for monotonic and cyclic, drained and undrained behaviors of sand, in part because the various design correlations are not necessarily physically consistent with each other; e.g., they may include a mix of laboratory test-based and case history-based relationships, or they have been empirically derived from laboratory data sets for different sands. Nonetheless, it is desirable that a model, after calibration to the design relationship that is of primary importance to a specific project, be able to produce behaviors that are reasonably consistent with the general magnitudes and trends in other applicable design correlations or typical experimental data.

Stress-strain behaviors of sand that are most commonly the focus in design are listed below, along with reference to a figure showing an example design correlation or typical experimental test result.

- The cyclic resistance ratio (CRR) against triggering of liquefaction, which is commonly estimated based on SPT and CPT penetration resistances with case history-based liquefaction correlations (e.g., Figure 1.2). The CRR is the cyclic stress ratio (e.g., $CSR = \tau_{cyc}/\sigma'_{vc}$, with τ_{cyc} = horizontal cyclic shear stress, σ'_{vc} = vertical consolidation stress) that is required to trigger liquefaction in a specified number of equivalent uniform loading cycles.

- The response under the irregular cyclic loading histories produced by earthquakes, which is approximately represented by the relationship between CRR and number of equivalent uniform loading cycles (e.g., Figure 1.3). This aspect of behavior also directly relates to the magnitude scaling factors (MSF) that are used with liquefaction correlations in practice.

- The dependence of CRR on effective confining stresses and sustained static shear stresses. These aspects of behavior are represented by the K_σ (Figure 1.4) and K_α (Figure 1.5) correction factors, respectively, which are used with liquefaction correlations in practice.

- The accumulation of shear strains after triggering of liquefaction. Evaluations of reasonable behavior are often based on comparisons to laboratory tests results for similar soils in the literature (e.g., Figure 1.6).

- The strength loss as a consequence of liquefaction, which may involve explicitly modeling phenomena such as void redistribution or empirically accounting for it through case history-based residual strength correlations (e.g., Figure 1.7).

- The small-strain shear modulus which can be obtained through in-situ shear wave velocity measurements.

- The shear modulus reduction and equivalent damping ratio relationships prior to triggering of liquefaction. These aspects of behavior are commonly estimated using empirical correlations derived from laboratory test results for similar soils in the literature (e.g., Figure 1.8).

- Drained monotonic shear strengths and stress-strain behavior (e.g., Figure 1.9). Peak friction angles may be estimated using relationships such as Bolton's (1986) relative dilatancy index, I_R (Figure 1.10) or correlations to SPT and CPT penetration resistances.

- Undrained monotonic shear strengths and stress-strain behavior (e.g., Figure 1.11), which may be

estimated using correlations to SPT and CPT penetration resistances.

- The volumetric strains during drained cyclic loading (Figure 1.12 and Figure 1.13) or due to reconsolidation following triggering of liquefaction (e.g., Figure 1.14), both of which may be estimated using empirical correlations derived from laboratory test results for similar soils in the literature.

The constitutive model described herein was developed for earthquake engineering applications, with specific goals being: (1) the ability to reasonably approximate empirical correlations used in practice, and (2) an ability to be calibrated within a reasonable amount of engineering effort. In essence, the approach taken was to calibrate the constitutive model at the equation level, such that the functional forms for the various constitutive relationships were chosen for their ability to approximate the important trends embodied in the extensive laboratory-based and case history-based empirical correlations that are commonly used in practice.

The organization of this report is structured as follows:

- Section 2 of this report contains a description of the model formulation.
- Section 3 contains a description of the model's implementation as a user defined material in a dynamic link library for use in the commercial program FLAC 8.1 (Itasca 2019) and FLAC2D 9.00 (Itasca 2023).
- Section 4 of this report contains a summary of the model input parameters, guidance on model parameter selections, and then illustrations of the model responses to a broad range of elemental loading conditions.
- Section 5 contains summary remarks regarding the model and its use in practice.

1.1 Revisions

Revisions to PM4Sand in Version 3, relative to Version 2, included: (1) revised dependency of dilatancy and plastic modulus on fabric and fabric history, (2) modifications to the initial back-stress ratio tracking logic, (3) modifications for improved modeling of post-liquefaction reconsolidation strains after the end of strong shaking in a simulation, (4) addition of a minor cohesion term to reduce potential hour-glassing and improve behavior of zones near a free surface, (5) a more efficient tensor library which reduces computational time, and (6) re-calibration of the model, resulting in changes to the default values for some secondary parameters.

Revisions to PM4Sand in Version 3.1, relative to Version 3, were minor. They included: (1) recompiling to run with FLAC 8.0 (Itasca 2016), (2) changes to the logic for input of secondary parameters, (3) a minor correction to the algorithm for post-liquefaction reconsolidation strains, and (4) renaming of some tracking variables. For boundary value problem simulations not involving post-liquefaction reconsolidation, these revisions have been found to have no effect on simulation results.

The report for Version 3.1 provided, relative to the one for Version 3, clarifications on some aspects of the model formulation and implementation in response to questions from users, corrected typographic errors, and described the above revisions to the input logic for secondary parameters.

Revision 1 to Version 3.1 (posted January 2018) documented that the Version 3.1 DLL module was recompiled on November 28, 2017 with a modification to the initialization scheme that prevents a problem that can arise with the use of the static solver during model initialization (i.e., introduction of

PM4Sand into a model) with certain sequences of commands. Note that it is still recommended that PM4Sand only be used with the dynamic solver, especially for any conditions involving significant applied loading, as explained in Section 3.6.

Revisions to PM4Sand Version 3.2 relative to Version 3.1, include a revision to the initial back-stress ratio initialization routine, a modification to the elastic shear modulus equation, a recalibration of the F_{sedmin} secondary parameter as well as a proper renaming of its input string for FLAC from `F_sed` to `F_sedmin`. The initial back-stress ratio at the time of model initialization is now limited to have a magnitude that is no greater than 90% of the bounding surface stress ratio (M^b); this constraint eliminates a problem that can occur when the model is initialized with consolidation stress states that are outside the bounding surface. The equation for the elastic shear modulus includes a C_{SR} term that reduces the elastic shear modulus at stress ratios close to the bounding surface. The C_{SR} term is normalized in Version 3.2 to produce a value of unity at the time of model initialization, which simplifies the calibration of the model. These changes do not significantly affect the general features of model responses but do affect responses for a given set of calibration parameters. Therefore, calibrations using PM4Sand Version 3.1 need to be revised when switching to Version 3.2. Furthermore, the manual was revised to reflect these changes as well as address minor typos and inconsistencies.

Revision to PM4Sand to Version 3.3 relative to Version 3.2 was adding a restriction that C_{SR} be less or equal to unity. In addition, the model was compiled for use with FLA2D 9.00. The DLL module for FLAC 8.1 *modelpm4sand005_64.dll* was compiled on June 12, 2023 using Microsoft Visual Studio Community 2015 C++. The DLL module for FLAC2D 9.00 *cmodelPM4Sand2D009.dll* was compiled on June 12, 2023 using Microsoft Visual Studio Community 2022 C++. Note that the compilation date and version are included in the properties of the DLL file. The simulations presented in this report were prepared using PM4Sand Version 3.3 in FLAC 8.1. PM4Sand Version 3.3 in FLAC2D 9.00 produced the same results.
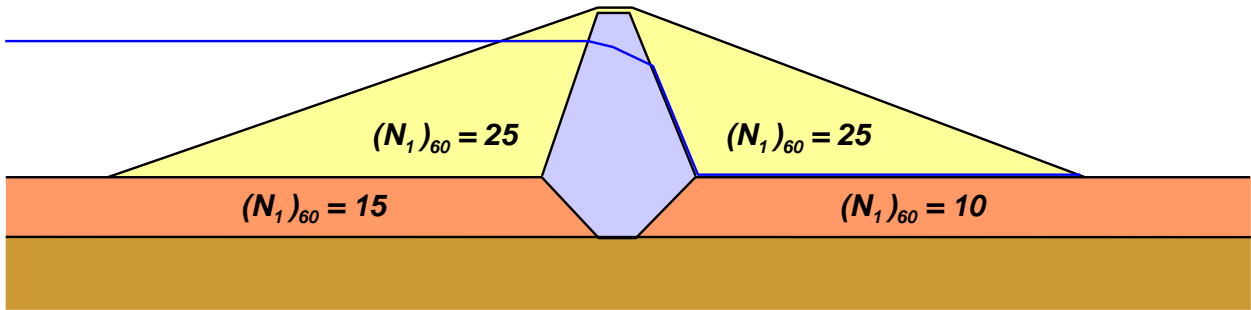
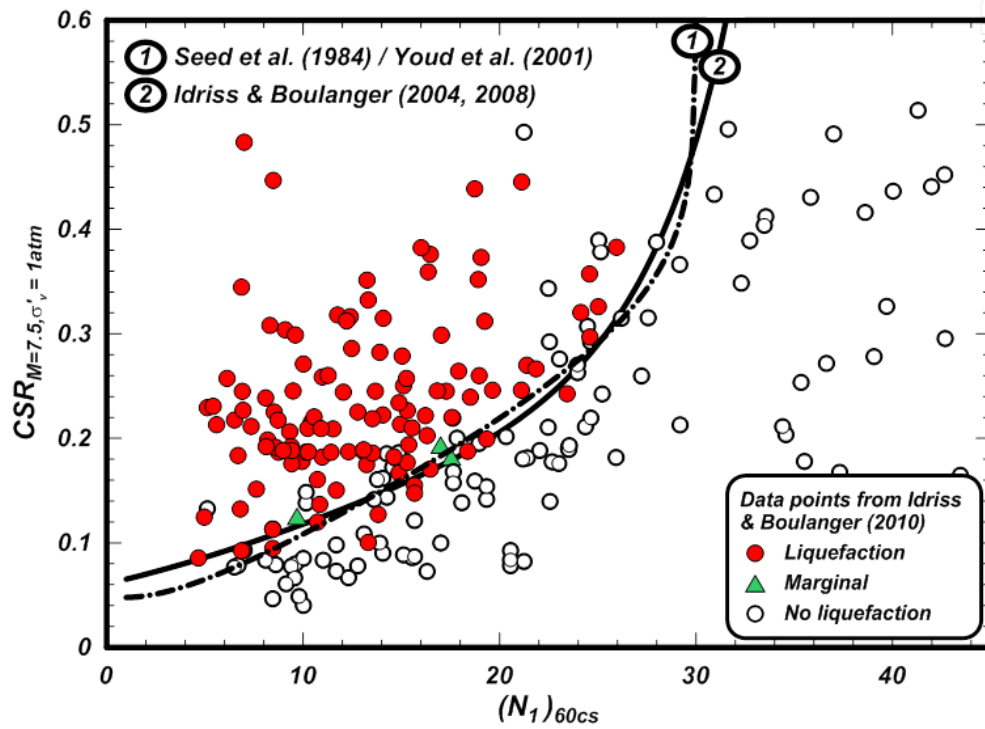Figure 1.1. Schematic cross-section for an earth dam.

Figure 1.2. Correlations for cyclic resistance ratio (CRR) from SPT data
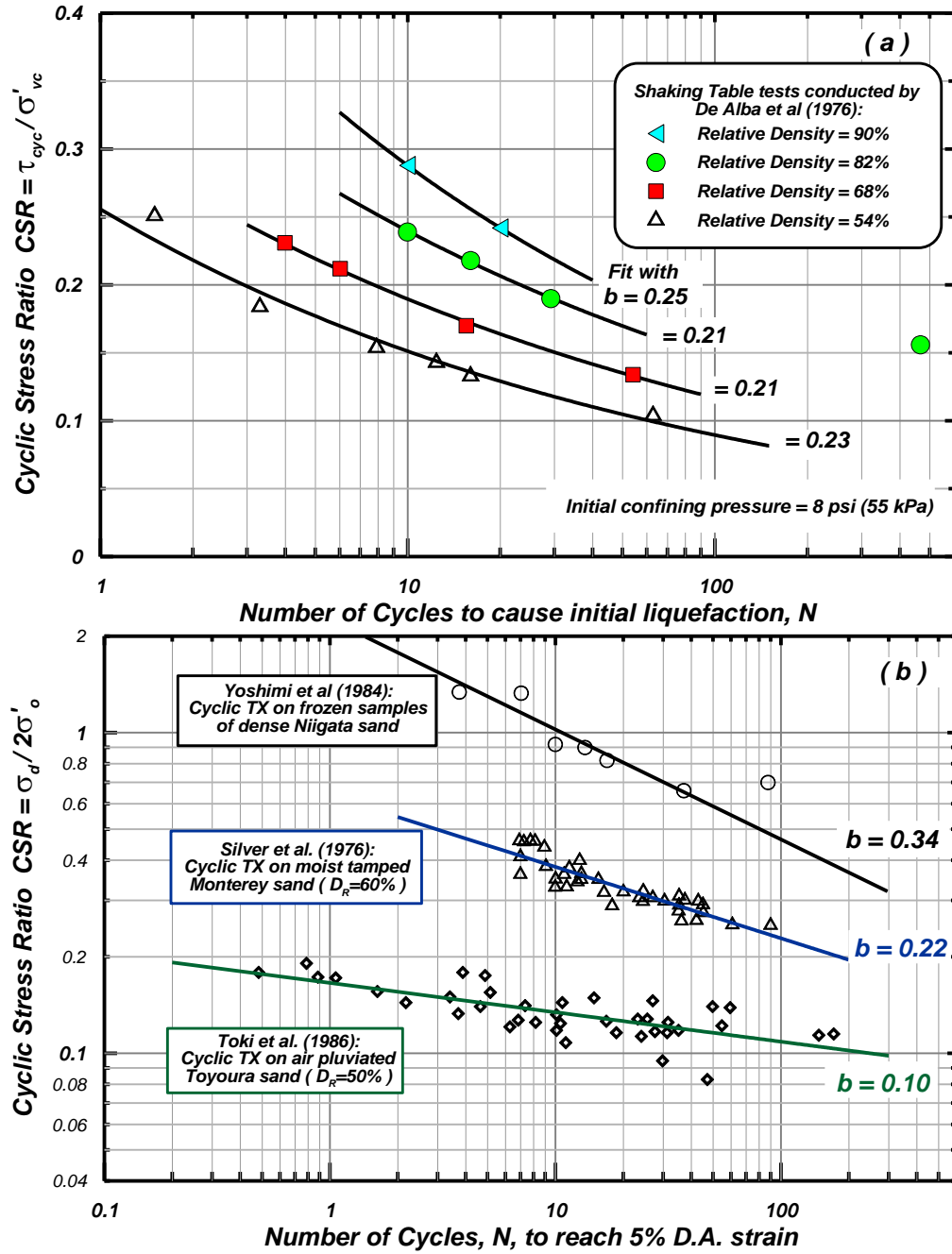(after Idriss and Boulanger 2010).

Figure 1.3. Relationships between cyclic resistance ratio (CRR) and number of equivalent uniform loading cycles for undrained loading of reconstituted and undisturbed samples of clean sand (from Ziotopoulou and Boulanger 2012).
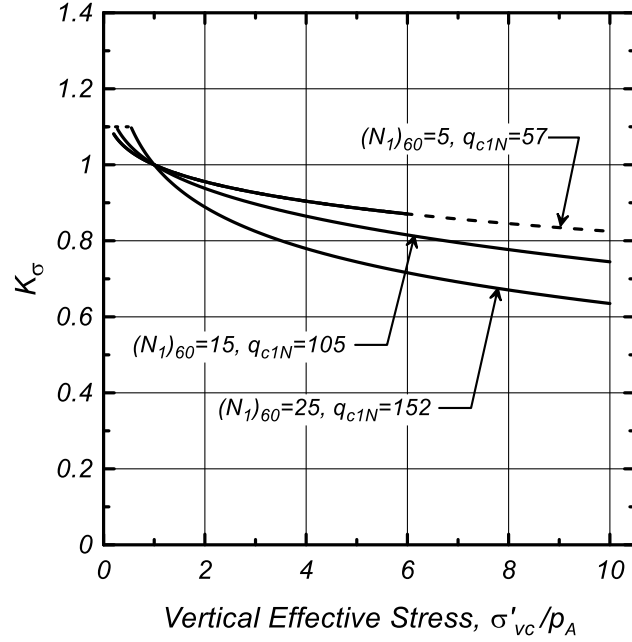
Figure 1.4. K_σ factor describing the effect that effective overburden stress has on cyclic resistance ratio of sands (from Idriss and Boulanger 2008).
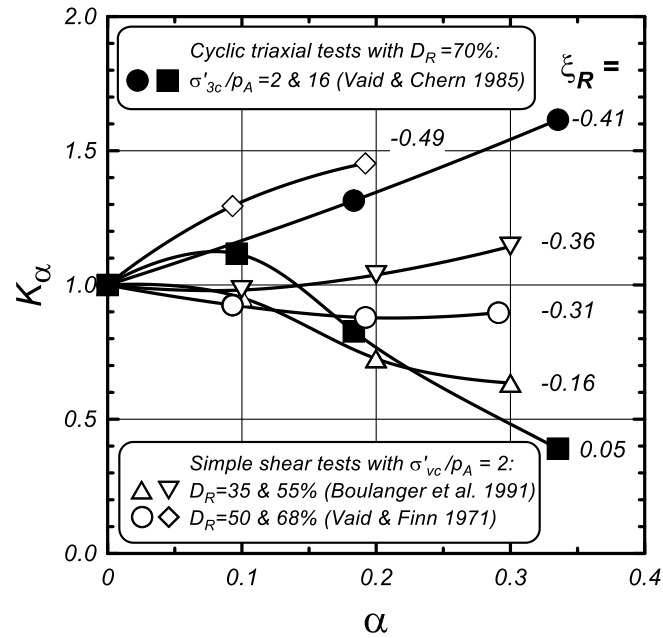
Figure 1.5. K_α factor describing the effect that sustained static shear stress ratio ($\alpha=\tau_s/\sigma'_{vc}$) has on cyclic resistance ratio of sands (Boulanger 2003a).

7
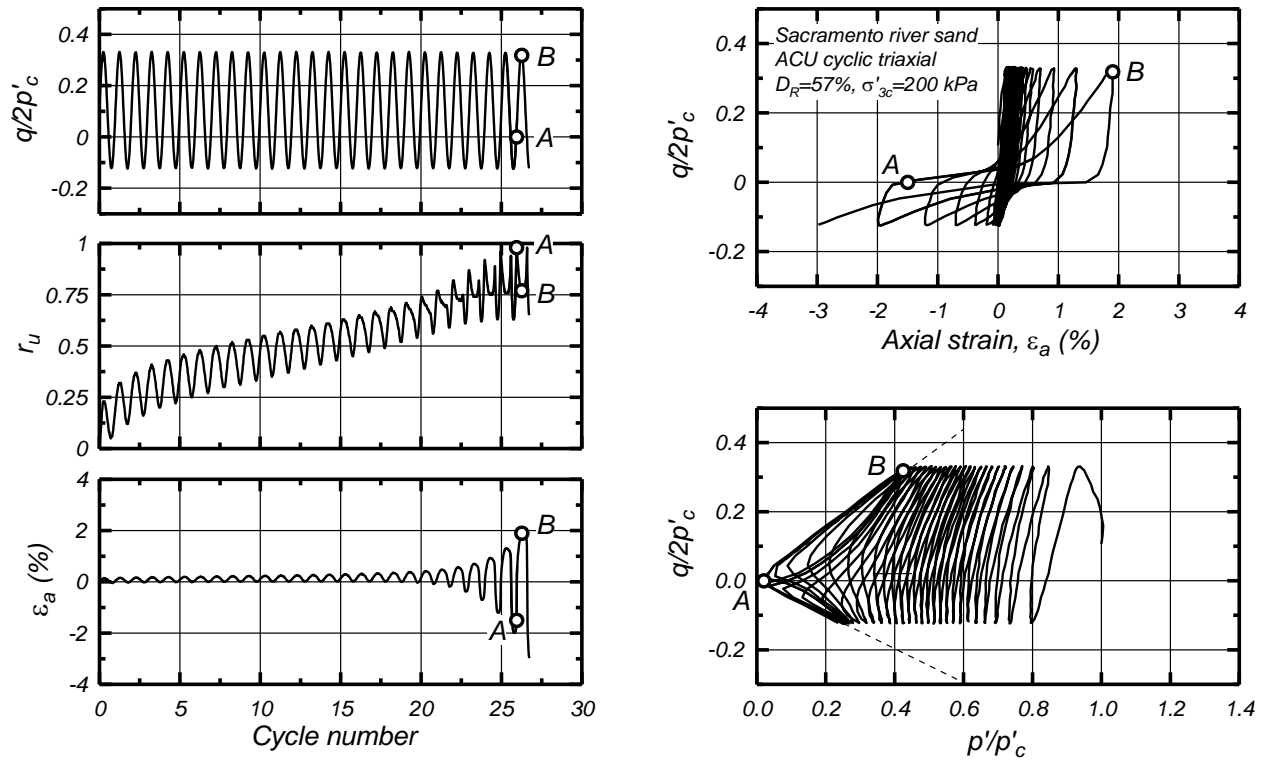
Figure 1.6. Undrained cyclic triaxial test on clean sand (test from Boulanger and Truman 1996; from Idriss and Boulanger 2008).

8
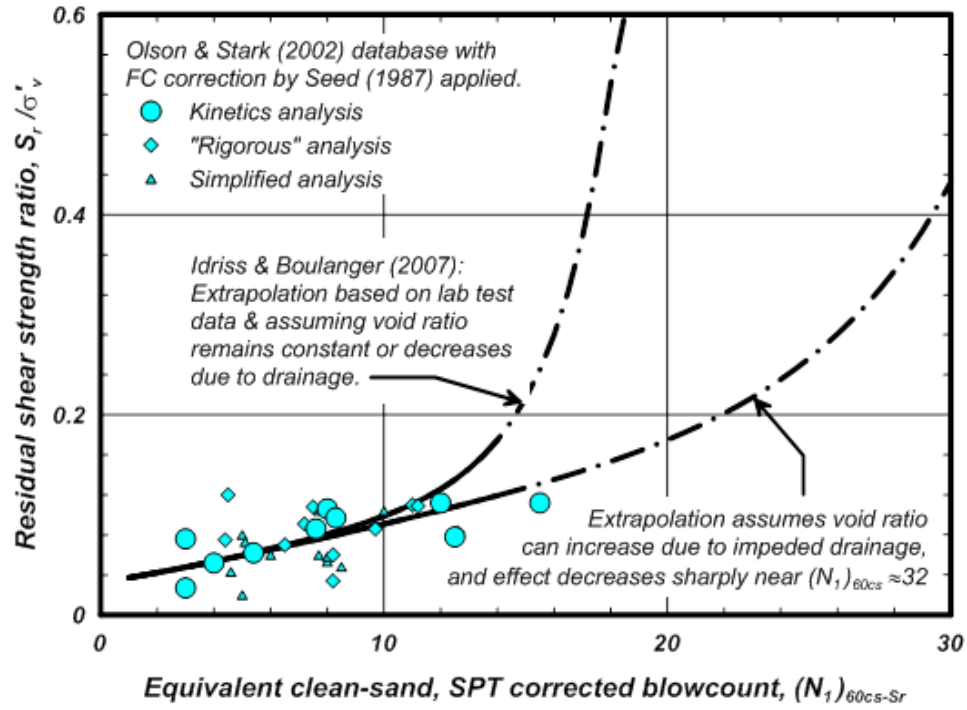
Figure 1.7. Empirical relationship for estimating residual strength of liquefied sands based on case histories (Boulanger and Idriss 2011).
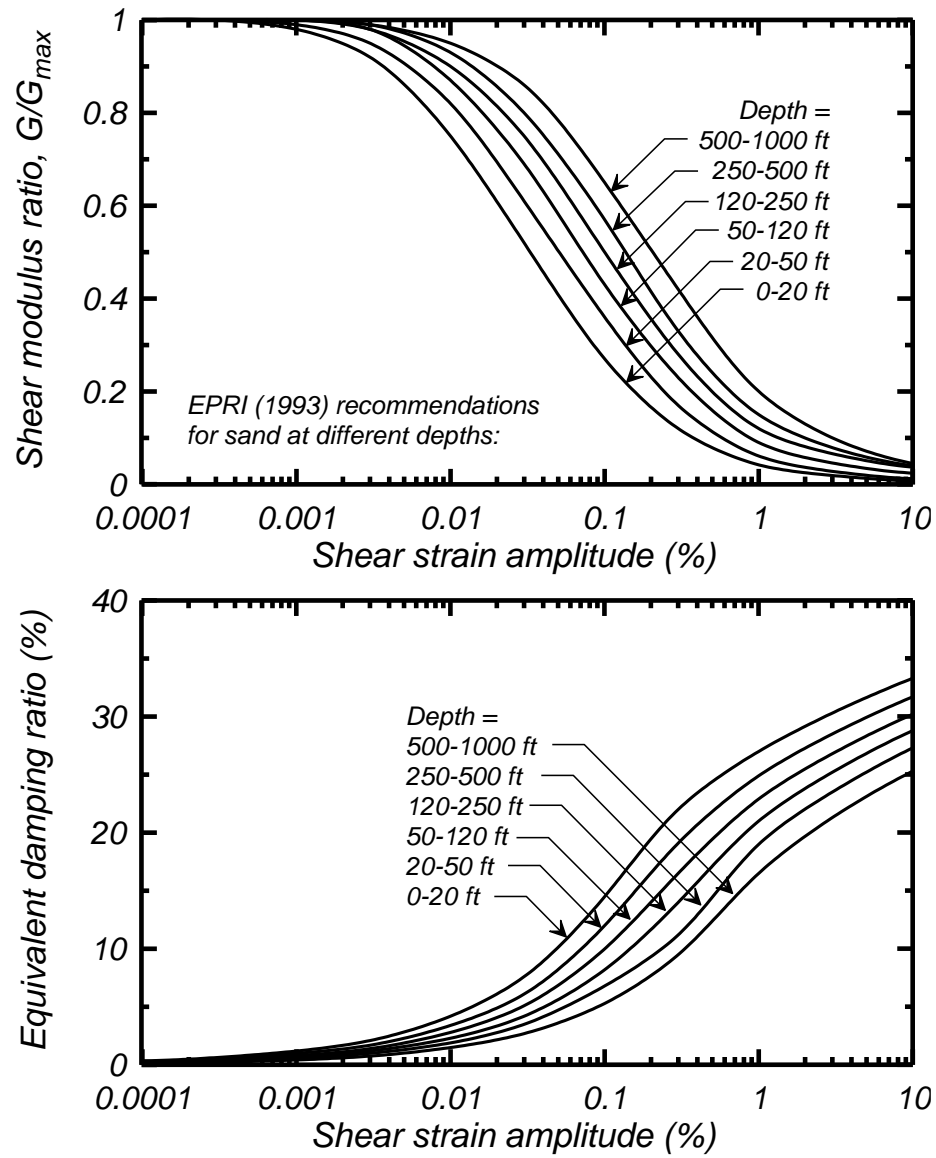
Figure 1.8. Shear modulus reduction and equivalent damping ratio relationship for sands, as recommended by EPRI (1993).
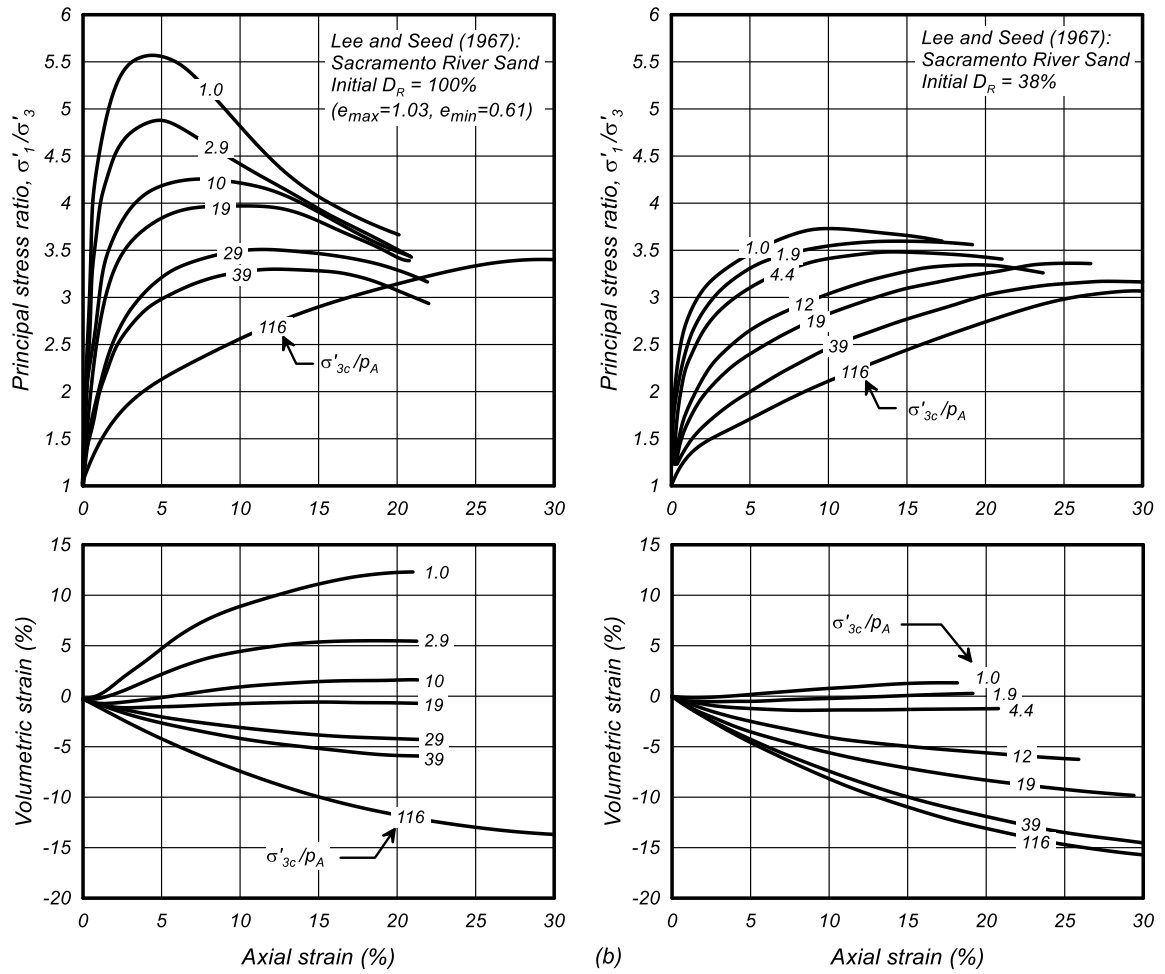
Figure 1.9. Drained triaxial compression tests on loose and dense sand specimens under a range of effective confining stresses (after Lee and Seed 1967; from Idriss and Boulanger 2008).
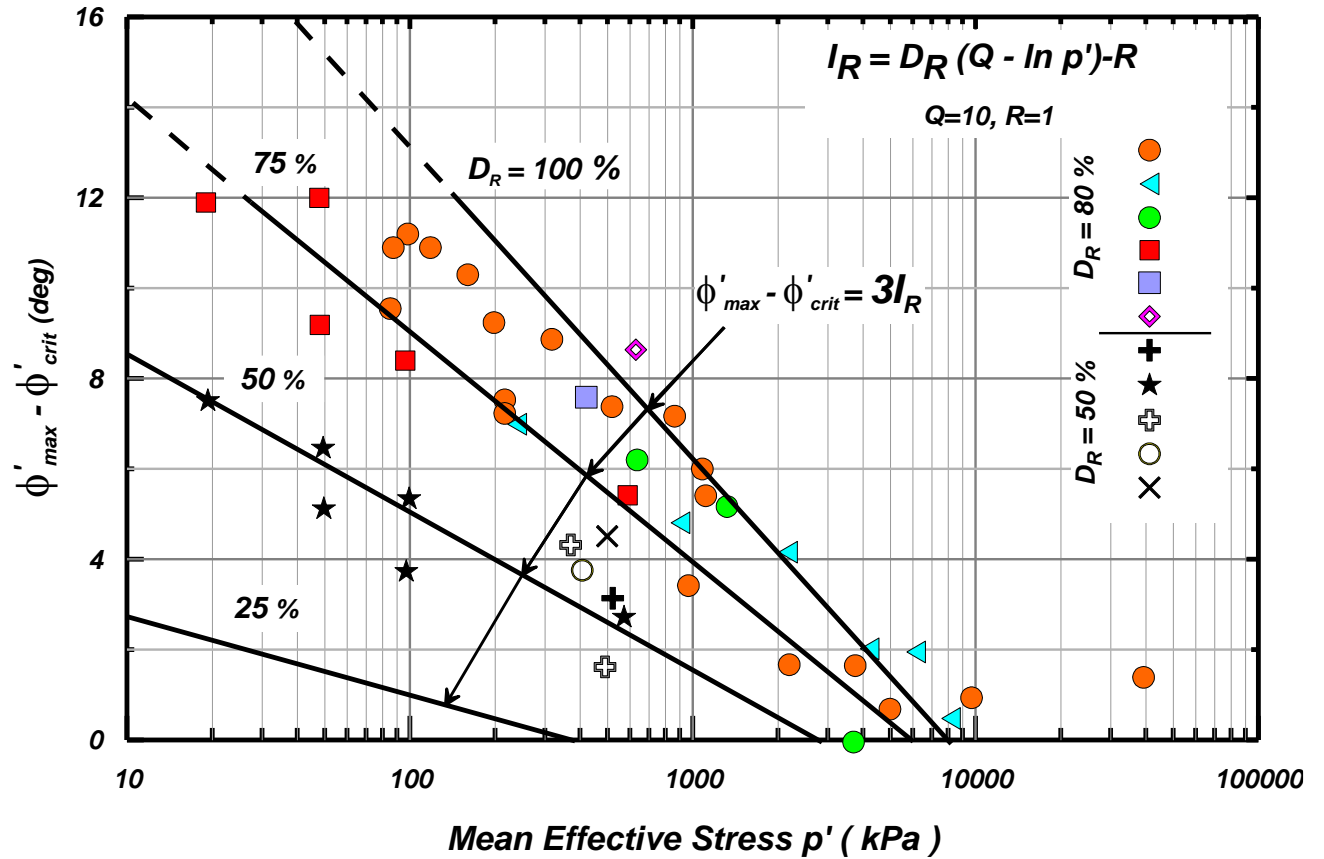
Figure 1.10. Triaxial test data for sands with initial relative densities in the vicinity of 80% or 50% failing at various mean effective stresses. The difference of peak friction angle from the critical friction angle is related to the relative dilatancy index (I_R) (after Bolton 1986).
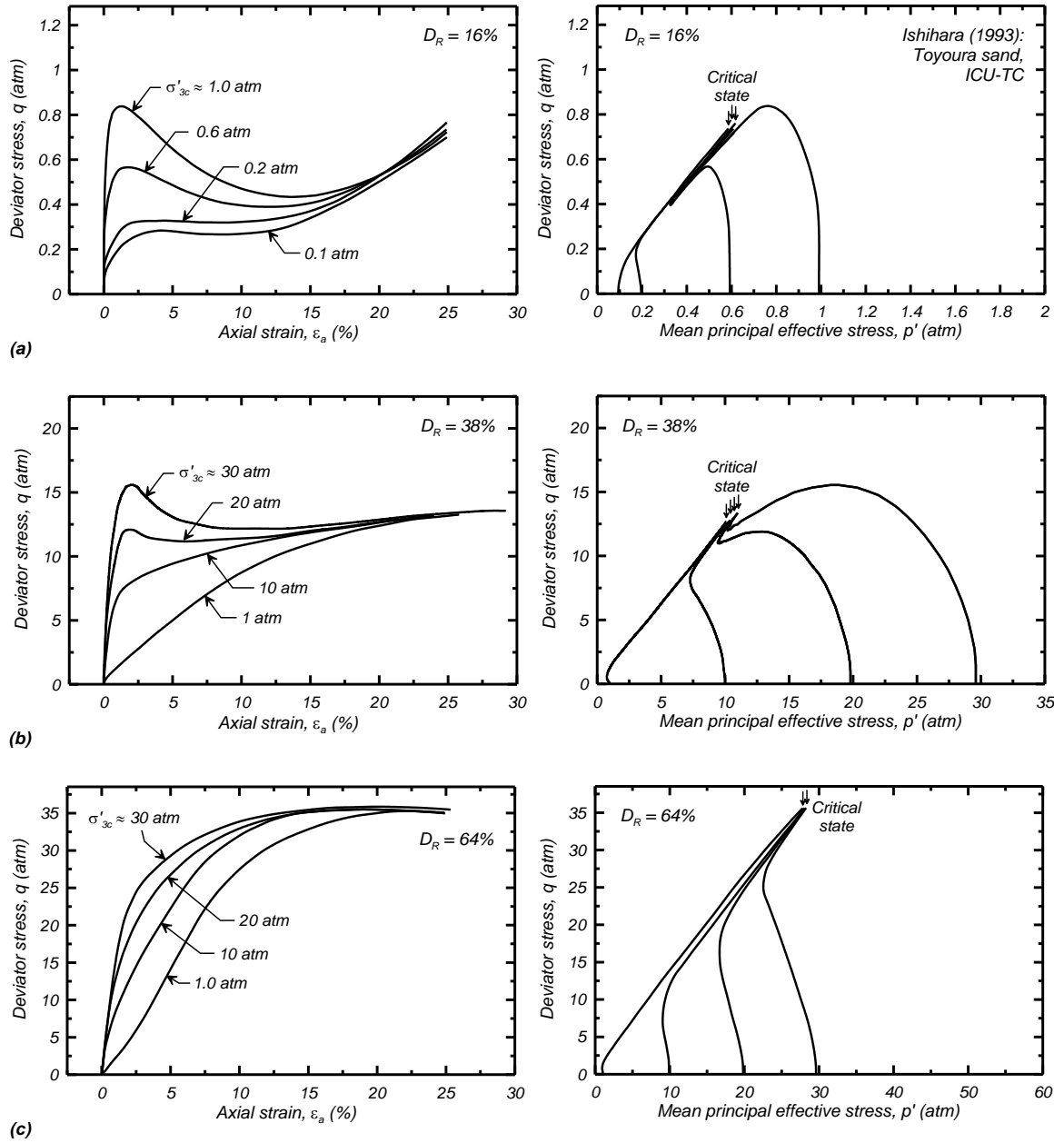
Figure 1.11. Undrained triaxial compression tests on very loose and loose sand specimens under a range of effective consolidation stresses (after Ishihara 1993; from Idriss and Boulanger 2008).
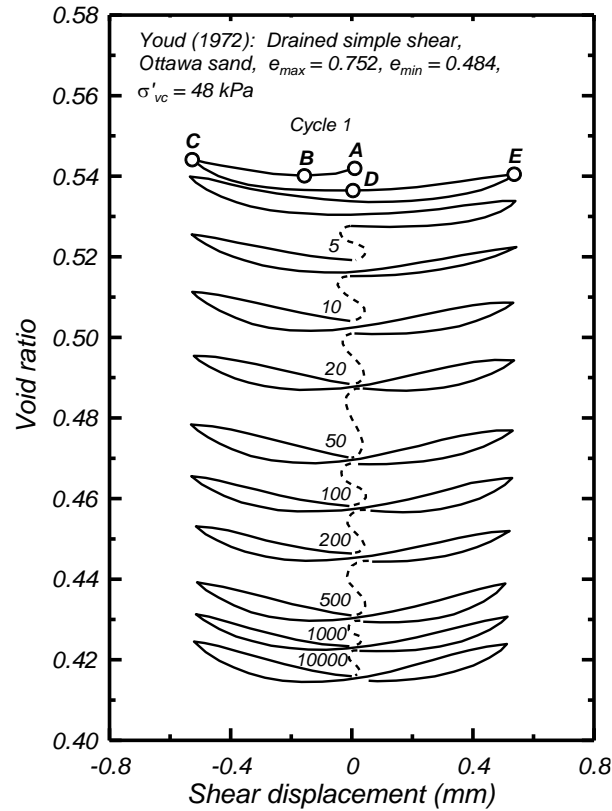
Figure 1.12. Drained cyclic simple shear test showing densification of a sand specimen with successive cycles of loading (after Youd 1972; from Idriss and Boulanger 2008).
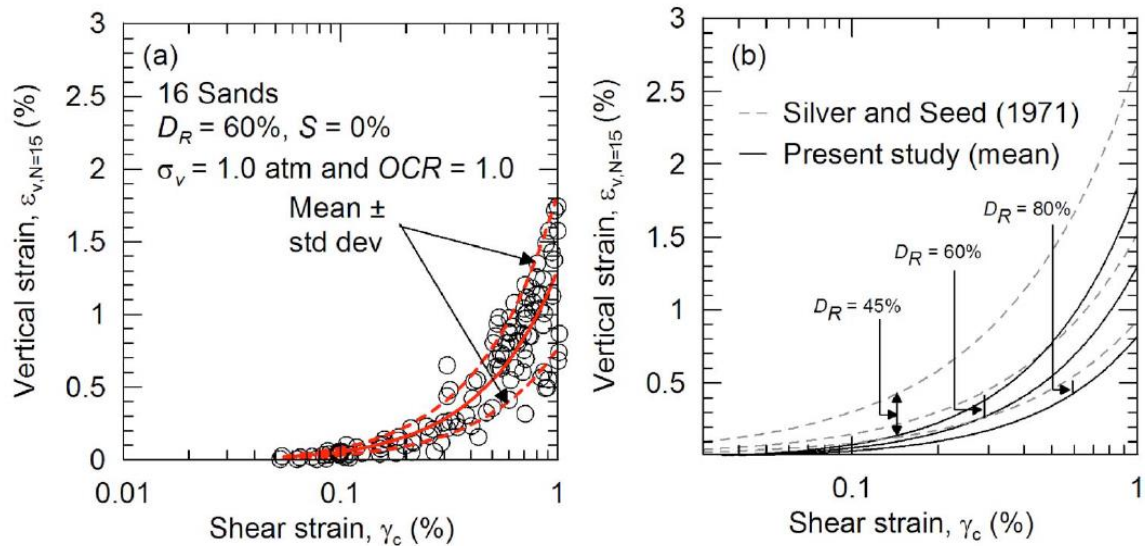
Figure 1.13. Volumetric strains in drained cyclic direct simple shear tests on clean sands (Duku et al. 2008): (a) Results from 16 sands at a relative density of about 60% with an overburden stress of 1.0 atm, and (b) Comparison of trends with earlier relationships by Silver and Seed (1971) for sands at relative densities of 45, 60, and 80%.

14
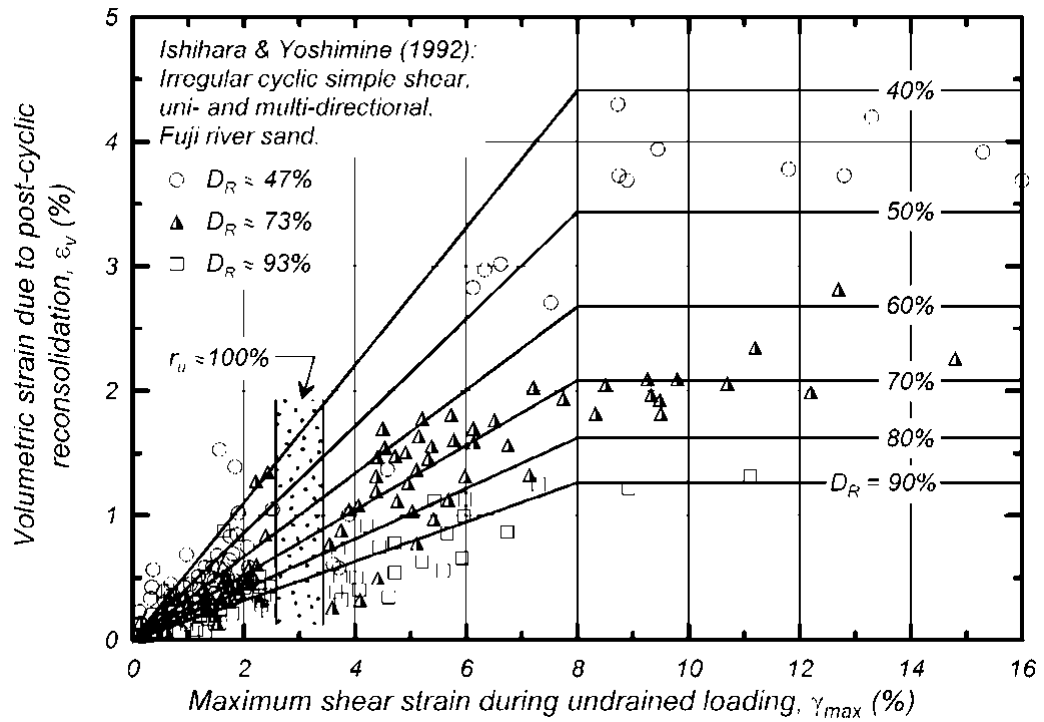
Figure 1.14. Relationship between post-liquefaction volumetric strain and the maximum shear strain induced during undrained cyclic loading of clean sand (after Ishihara and Yoshimine 1992; redrawn in Idriss and Boulanger 2008).

2. MODEL FORMULATION

The sand plasticity model presented herein follows the basic framework of the stress ratio-controlled, critical state-based, bounding surface plasticity model for sand presented by Dafalias and Manzari (2004). The Dafalias and Manzari (2004) model extended the previous work by Manzari and Dafalias (1997) by adding a fabric-dilatancy related tensor quantity to account for the effect of fabric changes during loading. The fabric-dilatancy related tensor was used to macroscopically model the effect that microscopically-observed changes in sand fabric during plastic dilation have on the contractive response upon reversal of loading direction. Dafalias and Manzari (2004) provide a detailed description of the motivation for the model framework, beginning with a triaxial formulation that simplifies its presentation and followed by a multi-axial formulation. The model described herein is presented in its multi-axial formulation, along with the original framework of the Dafalias-Manzari model for comparison.

2.1 Basic stress and strain terms

The basic stress and strain terms for the model are as follows. The model is based on effective stresses, with the conventional prime symbol dropped from the stress terms for convenience because all stresses are effective for the model. The stresses are represented by the tensor $\boldsymbol{\sigma}$, the principal effective stresses σ_1, σ_2, and $\sigma_3$, the mean effective stress p, the deviatoric stress tensor $\mathbf{s}$, and the deviatoric stress ratio tensor $\mathbf{r}$. The present implementation was further simplified by casting the various equations and relationships in terms of the in-plane stresses only. This limits the present implementation to plane-strain applications and is not correct for general cases, but it has the advantage of simplifying the implementation and improving computational speed by reducing the number of operations. Expanding the implementation to include the general case should not affect the general features of the model. Consequently, the relationships between the various stress terms can be summarized as follows:

$$\boldsymbol{\sigma} = \begin{pmatrix} \sigma_{xx} & \sigma_{xy} \\ \sigma_{xy} & \sigma_{yy} \end{pmatrix} \tag{1}$$

$$p = \frac{\sigma_{xx} + \sigma_{yy}}{2} \tag{2}$$

$$\mathbf{s} = \boldsymbol{\sigma} - p\mathbf{I} = \begin{pmatrix} s_{xx} & s_{xy} \\ s_{xy} & s_{yy} \end{pmatrix} = \begin{pmatrix} \sigma_{xx} - p & \sigma_{xy} \\ \sigma_{xy} & \sigma_{yy} - p \end{pmatrix} \tag{3}$$

$$r = \frac{s}{p} = \begin{pmatrix} r_{xx} & r_{xy} \\ r_{xy} & r_{yy} \end{pmatrix} = \begin{pmatrix} \dfrac{\sigma_{xx} - p}{p} & \dfrac{\sigma_{xy}}{p} \\ \dfrac{\sigma_{xy}}{p} & \dfrac{\sigma_{yy} - p}{p} \end{pmatrix} \tag{4}$$

Note that the deviatoric stress and deviatoric stress ratio tensors are symmetric with $r_{xx} = -r_{yy}$ and $s_{xx} = -s_{yy}$ (meaning a zero trace), and that $\mathbf{I}$ is the identity matrix.

The model strains are represented by a tensor ε, which can be separated into the volumetric strain ε_v and the deviatoric strain tensor $\mathbf{e}$. The volumetric strain in plane strain is,

$$\varepsilon_v = \varepsilon_{xx} + \varepsilon_{yy} \tag{5}$$

and the deviatoric strain tensor is,

$$e = \varepsilon - \frac{\varepsilon_v}{3} I = \begin{pmatrix} \varepsilon_{xx} - \dfrac{\varepsilon_v}{3} & \varepsilon_{xy} \\ \varepsilon_{xy} & \varepsilon_{yy} - \dfrac{\varepsilon_v}{3} \end{pmatrix} \tag{6}$$

In incremental form, the deviatoric and volumetric strain terms are decomposed into an elastic and a plastic part,

$$d e = d e^{el} + d e^{pl} \tag{7}$$

$$d \varepsilon_v = d \varepsilon_v^{el} + d \varepsilon_v^{pl} \tag{8}$$

where

$d e^{el}$ = elastic deviatoric strain increment tensor

$d e^{pl}$ = plastic deviatoric strain increment tensor

$d \varepsilon_v^{el}$ = elastic volumetric strain increment

$d \varepsilon_v^{pl}$ = plastic volumetric strain increment

2.2 Critical state

Dafalias and Manzari (2004), based on findings in Li and Wang (1998), used a power relationship to approximate the curving of the critical state line (Schofield and Wroth 1968) that occurs over a broad range of confining stresses,

$$e_{cs} = e_o - \lambda \left(\frac{p_{cs}}{p_A} \right)^m \tag{9}$$

where p_{cs} = mean stress at critical state, e_{cs} = critical state void ratio, and e_o, λ, and m are parameters controlling the position and shape of the critical state line. The state of the sand was then described using the state parameter (Been and Jefferies 1985), which is the difference between the current void ratio (e) and the critical state void ratio (e_{cs}) at the same mean effective stress (p_{cs}).

The model presented herein instead uses the relative state parameter index (ξ_R) as presented in Boulanger (2003a) and shown in Figure 2.1(a). The relative state parameter (Konrad 1988) is the state parameter normalized by the difference between the maximum void ratio (e_{max}) and minimum void ratio (e_{min}) values that are used to define relative density (D_R). The relative state parameter "index" is just the relative state parameter defined using an empirical relationship for the critical state line. Boulanger (2003a) used Bolton's (1986) dilatancy relationship to define the empirical critical state line and thus arrived at,

$$\xi_R = D_{R,cs} - D_R \tag{10}$$

$$D_{R,cs} = \frac{R}{Q - \ln \left(100 \frac{p}{p_A} \right)} \tag{11}$$

where $D_{R,cs}$ = relative density at critical state for the current mean effective stress. The parameters Q and R were shown by Bolton (1986) to be about 10 and 1.0, respectively, for quartzitic sands. Critical state lines using the above expression with Q values of 9 and 10, and with R values of 1.0 and 1.5 are shown in Figure 2.1.(b).

2.3 Bounding, dilatancy, and critical surfaces

The model incorporates bounding, dilatancy, and critical stress ratio surfaces following the form of Dafalias and Manzari (2004). The present model simplifies the surfaces by removing the Lode angle dependency (e.g., friction angles are the same for compression or extension loading) that was included in the Dafalias and Manzari model, such that the bounding (M^b) and dilatancy (M^d) ratios can be related to the critical stress ratio (M) by the following simpler expressions,

$$M^b = M \cdot \exp\left(-n^b \xi_R\right) \tag{12}$$

$$M^d = M \cdot \exp\left(n^d \xi_R\right) \tag{13}$$

18

where n^b and n^d are parameters determining the values of M^b and M^d, respectively. For the present implementation, the mean normal stress p is taken as the average of the in-plane normal stresses (Equation 2), q is the difference in the major and minor principal in-plane stresses, and the relationship for M is therefore reduced to,

$$M = 2 \cdot \sin\left(\phi_{cv}\right) \tag{14}$$

where ϕ_{cv} is the constant volume or critical state effective friction angle. The three surfaces can, for the simplifying assumptions described above, be conveniently visualized as linear lines on a q-p plot (where $q = \sigma_1 - \sigma_3$) as shown in Figure 2.2 or as circular surfaces on a stress ratio graph of r_{yy} versus r_{xy} as shown in Figure 2.3.

As the model is sheared toward critical state ($\xi_R = 0$), the values of M^b and M^d will both approach the value of M. Thus, the bounding and dilatancy surfaces move together during shearing until they coincide with the critical state surface when the soil has reached critical state.

The above functional form for the bounding stress ratio controls the relationship between peak friction angle and relative state, which is consistent with the forms and data previously proposed by Been and Jefferies (1985) and Konrad (1986). The data from those studies were primarily for sands that were dense-of-critical, and the above relationship can reasonably fit those data. The few data points for loose-of-critical sands show that the peak friction angles (presumably determined at the limit of strains possible within the laboratory tests) were only slightly smaller than the critical state values, such that extending the above relationships to loose-of-critical sands may tend to underestimate the peak friction angles. Consequently, the present model allows n^b and n^d to be different for loose-of-critical and dense-of-critical states for the same sand.

2.4 Yield surface and image back-stress ratio tensors

The yield surface and back-stress ratio tensor (α) follow those of the Dafalias and Manzari model, although their final form is considerably simplified by the prior assumption of removing any Lode angle dependency. The yield surface is a small cone in stress space, and is defined in stress terms by the following expression,

$$f = \left[(s - p\alpha):(s - p\alpha)\right]^{1/2} - \sqrt{1/2}\, pm = 0 \tag{15}$$

The back-stress ratio tensor α defines the center of the yield surface, and the parameter m defines the radius of the cone in terms of stress ratio. The yield function can be rewritten to emphasize the role of stress ratio terms as follows,

$$f = \sqrt{(r - \alpha):(r - \alpha)} - \sqrt{1/2}\, m = 0 \tag{16}$$

The yield function can then be visualized as related to the distance between the stress ratio **r** and the back-stress ratio α, as illustrated in Figure 2.3.

19

The bounding surface formulation now requires that bounding and dilatancy stress ratio tensors be defined. Dafalias and Manzari (2004) showed that it is more convenient to track back-stress ratios and to similarly define bounding and dilatancy surfaces in terms of back-stress ratios. An image back-stress ratio tensor for the bounding surface (α^b) is defined as,

$$\boldsymbol{\alpha}^b = \sqrt{\frac{1}{2}} \left[M^b - m \right] \boldsymbol{n} \tag{17}$$

where the tensor $\mathbf{n}$ is normal to the yield surface. An image back-stress ratio tensor for the dilatancy surface (α^d) is similarly defined as,

$$\boldsymbol{\alpha}^d = \sqrt{\frac{1}{2}} \left[M^d - m \right] \boldsymbol{n} \tag{18}$$

The computation of constitutive responses can now be more conveniently expressed in terms of back-stress ratios rather than in terms of stress ratios, as noted by Dafalias and Manzari (2004).

2.5 Stress reversal and initial back-stress ratio tensors

The bounding surface formulation, as described in Dafalias (1986) and adopted by Dafalias and Manzari (2004), keeps track of the initial back-stress ratio (α_{in}) and uses it in the computation of the plastic modulus K_p. This tracking of one instance in loading history is essentially a first-order method for tracking loading history. A reversal in loading direction is then identified, following traditional bounding surface practice, whenever,

$$\left(\boldsymbol{\alpha} - \boldsymbol{a}_{in} \right) : \boldsymbol{n} < 0 \tag{19}$$

A reversal causes the current stress ratio to become the initial stress ratio for subsequent loading. Small cycles of load reversal can reset the initial stress ratio and cause the plastic modulus K_p to increase accordingly, in which case the stress-strain response becomes overly stiff after a small load reversal. This is a well-known problem in bounding surface formulations for which various approaches offer different advantages and disadvantages.

The model presented herein tracks an initial back-stress ratio and a previous initial back-stress ratio (α_{in}^p), as illustrated in Figure 2.4a. When a reversal occurs, the previous initial back-stress ratio is updated to the initial back-stress ratio, and the initial back-stress ratio is updated to the current back-stress ratio.

In addition, the model tracks an apparent initial back-stress ratio tensor (α_{in}^{app}) as schematically illustrated in Figure 2.4b. The schematic in Figure 2.4b is similar to that of Figure 2.4a, except that the most recent loading reversals correspond to a small unload-reload cycle on an otherwise positive loading branch. The components of α_{in}^{app} are taken as: (i) for positive loading directions, the minimum value they have ever had, but no smaller than zero, and (ii) for negative loading directions, the maximum value they have ever had, but no greater than zero. Figure 2.5 further illustrates these scenarios for four different loading cases. These minimum and maximum past back-stress ratios are

stored for each component individually and for the entire loading history. The use of $\boldsymbol{\alpha}_{in}^{app}$ helps avoid the over-stiffening of the stress-strain response following small unload-reload cycles along an otherwise monotonically increasing branch of loading, without having to track the loading history through many cycles of load reversals.

The computation of K_p utilizes the values of $\boldsymbol{\alpha}_{in}^{app}$, $\boldsymbol{\alpha}_{in}^{true}$, and $\boldsymbol{\alpha}_{in}^{p}$, as defined in Figure 2.4b and Figure 2.5, to better approximate the stress-strain response during an unload-reload cycle. For the last positive loading branch in this figure, the value of K_p is initially most strongly controlled (inversely) by the distance $(\boldsymbol{\alpha} - \boldsymbol{\alpha}_{in}^{true}):\mathbf{n}$, such that the stiffness is initially large. As positive loading continues, the progressive reduction in K_p becomes increasingly dependent on $\boldsymbol{\alpha}_{in}^{app}$ as well. Once the positive loading exceeds the previous reversal point, the value of K_p becomes solely dependent on the distance $(\boldsymbol{\alpha} - \boldsymbol{\alpha}_{in}^{app}):\mathbf{n}$. Thus, the computation of K_p has the following dependencies,

$$
\begin{aligned}
if \ (\boldsymbol{\alpha} - \boldsymbol{\alpha}_{in}^{p}):\boldsymbol{n} < 0 &\Rightarrow K_p = f\left(\alpha_{in}^{true}, \alpha_{in}^{app}\right) \\
else \quad\quad &\Rightarrow K_p = f\left(\alpha_{in}^{app}\right)
\end{aligned}
\tag{20}
$$

The equations relating K_p to these back-stress ratios are given later in Section 2.7.

The impact of the above logic for defining $\boldsymbol{\alpha}_{in}$ on stress-strain responses is demonstrated in Figure 2.6 showing α_{xy} versus shear strain γ computed for two different drained DSS loading simulations. For these two examples, the reloading stiffness of the current loading branch (green line) is initially large because K_p is initially computed based on $\boldsymbol{\alpha}_{in} = \boldsymbol{\alpha}_{in}^{true}$. As the loading exceeds $\boldsymbol{\alpha}_{in}^{p}$, the loading stiffness becomes much softer because K_p is now computed based on $\boldsymbol{\alpha}_{in} = \boldsymbol{\alpha}_{in}^{app}$.

The initial back-stress ratio $(\boldsymbol{\alpha}_{in})$ is first established at initialization of the model or upon execution of FirstCall (see also Section 3). The value of $\boldsymbol{\alpha}_{in}$ is established as being equal to the current back-stress ratio, subject to the limitation that its corresponding stress ratio be $\leq 0.9 \ M^b$. This constraint on the magnitude of $\boldsymbol{\alpha}_{in}$ at initialization avoids a problem that can otherwise occur when the initial consolidation stress state is above the bounding surface. In such cases, $K_p = 0$ since $M^{cur} > M^b$ and $D = 0$ since $\boldsymbol{\alpha} - \boldsymbol{\alpha}_{in} = 0$, which can result in no stress changes during shearing and hence an incorrect response. Linearly scaling $\boldsymbol{\alpha}_{in}$ so its corresponding stress ratio is $\leq 0.9 \ M^b$ upon initialization ensures that $D > 0$ at the start of shearing whenever the initial consolidation stress state corresponds to a stress ratio $> 0.9 \ M^b$. Undrained shearing from such an initial consolidation stress state will thus be properly accompanied by contraction and associated strain softening.

2.6 Elastic strains and moduli

The elastic deviatoric strain and elastic volumetric strain increments are computed as,

$$
d\boldsymbol{e}^{el} = \frac{d\boldsymbol{s}}{2G}
\tag{21}
$$

$$d\varepsilon_v^{el} = \frac{dp}{K} \tag{22}$$

where G is the elastic shear modulus and K is the elastic bulk modulus. The elastic shear modulus in the model presented herein is dependent on the mean effective stress according to,

$$G = G_o p_A \left(\frac{p}{p_A} \right)^{\frac{1}{2}} C_{SR} \tag{23}$$

where G_o is a constant, p_A is the atmospheric pressure (101.3 kPa), and C_{SR} is a factor that accounts for stress ratio effects (described below).

Dafalias and Manzari (2004) had included dependence of G on void ratio following the form of Richart et al. (1970). This aspect was not included in the model herein because: (1) the effects of void ratio changes on G are small relative to those of confining stress, (2) the value of G is more strongly affected by environmental factors such as cementation and ageing, and (3) the calibration of G to in-situ shear wave velocity data is simplified by not including e.

Yu and Richart (1984) showed that the small-strain elastic shear modulus of sand is dependent on the stress ratio and stress ratio history. The effect of stress ratio was shown to generally be less than about 10% when the ratio of major to minor principal effective stresses is less than about 2.5, but to also increase to about 20-30% at higher principal stress ratios. They also showed that stress ratio history caused a reduction in the small-strain elastic shear modulus when the maximum previous stress-ratio was greater than the current stress ratio. The effect of stress ratio and stress ratio history on the elastic shear modulus was approximately accounted for in the present model by the factor C_{SR}. The following equation for C_{SR} is similar in form to that used by Yu and Richart (1984) to represent stress ratio effects, except that it uses stress ratio terms consistent with the present model. The equation for C_{SR} was further normalized in PM4Sand Version 3.2 to produce a value of unity at the time of model initialization, and restricted to values less than unity thereafter, as,

$$C_{SR} = \frac{1 - C_{SR,o} \cdot \left(\dfrac{M}{M^b} \right)^{m_{SR}}}{\left[1 - C_{SR,o} \cdot \left(\dfrac{M}{M^b} \right)^{m_{SR}} \right]_{initial}} \leq 1 \tag{24}$$

The numerator in the above equation is the same form used in Version 3.1 of the model, while the denominator retains the value of the numerator from the time of model initialization. Thus, C_{SR} = 1.0 at the time of initialization. The above equation approximates Yu and Richart's (1984) results for stress ratio effects when $C_{SR,0}$ = 0.3 and m_{SR} = 2. The effects of stress ratio history would cause further reductions, and are more complicated to represent. The calibration examples presented later in this report worked well with $C_{SR,0}$ = 0.5 and m_{SR} = 4, which keeps the effect of stress ratio on elastic

modulus small at small stress ratios, but lets the effect increase to a 60% reduction when the stress ratio is on the bounding surface.

The elastic bulk modulus is related to the shear modulus through the Poisson's ratio as,

$$K = \frac{2(1+v)}{3(1-2v)}G \tag{25}$$

as was done by Dafalias and Manzari (2004).

2.7 Plastic components without fabric effects

Loading index

The loading index (L) is used to compute the plastic component of the volumetric strain increment and the plastic deviatoric strain increment tensor as,

$$d\varepsilon_v^{pl} = \langle L \rangle D \tag{26}$$

$$de^{pl} = \langle L \rangle \boldsymbol{R}' \tag{27}$$

where D is the dilatancy, **R** is the direction of dε^{pl}, **R′** is the deviatoric component of **R**, and <> are Macaulay brackets that set negative values to zero [i.e., <L> = L if L ≥ 0, and <L> = 0 if L < 0]. The tensor **R** for the assumption of no Lode angle dependency is,

$$\boldsymbol{R} = \boldsymbol{n} + \frac{1}{3}D\boldsymbol{I} \tag{28}$$

where **n** is the unit normal to the yield surface (Figure 2.3). Note that the assumption of no Lode angle dependency also means that **R′** = **n**. The dilatancy D relates the incremental plastic volumetric strain to the incremental plastic deviatoric strain,

$$D = \frac{d\varepsilon_v^{pl}}{\left| de^{pl} \right|} \tag{29}$$

The dilatancy D can be also related to the conventional engineering shear strain in this plane strain approximation, as,

$$D = \frac{d\varepsilon_v^{pl}}{\sqrt{\frac{1}{2}}\left|d\gamma^{pl}\right|} \tag{30}$$

The loading index, as derived in Dafalias and Manzari (2004) is,

$$L = \frac{1}{K_p}\frac{\partial f}{\partial \boldsymbol{\sigma}} : d\boldsymbol{\sigma} = \frac{1}{K_p}\left[\boldsymbol{n} : d\boldsymbol{s} - \boldsymbol{n} : \boldsymbol{r}dp\right]$$

$$L = \frac{2G\boldsymbol{n} : d\boldsymbol{e} - \boldsymbol{n} : \boldsymbol{r}Kd\varepsilon_v}{K_p + 2G - KD\boldsymbol{n} : \boldsymbol{r}} \tag{31}$$

The stress increment for an imposed strain increment can then be computed as,

$$d\boldsymbol{\sigma} = 2Gd\boldsymbol{e} + Kd\varepsilon_v\boldsymbol{I} - \langle L\rangle\left(2G\boldsymbol{n} + KD\boldsymbol{I}\right) \tag{32}$$

Hardening and the update of the back-stress ratio

Updating of the back-stress ratio is dependent on the hardening aspects of the model. Dafalias and Manzari (2004) updated the back-stress ratio according to bounding surface practice as,

$$d\boldsymbol{\alpha} = \langle L\rangle\left(\frac{2}{3}\right)h\left(\boldsymbol{\alpha}^b - \boldsymbol{\alpha}\right) \tag{33}$$

where h is the hardening coefficient. The factor of 2/3 was included for convenience so that model constants would be the same in triaxial and multi-axial derivations. They subsequently showed that the consistency condition δf=0 was satisfied when the plastic modulus K_p was related to the hardening coefficient as,

$$K_p = \frac{2}{3}p\,h\left(\boldsymbol{\alpha}^b - \boldsymbol{\alpha}\right) : \boldsymbol{n} \tag{34}$$

This expression can be rearranged so as to show that the consistency equation can be satisfied by expressing the hardening coefficient as,

$$h = \frac{3}{2}\frac{K_p}{p\left(\boldsymbol{\alpha}^b - \boldsymbol{\alpha}\right) : \boldsymbol{n}} \tag{35}$$

The relationship for the plastic modulus can subsequently take a range of forms, provided that the hardening coefficient and updating of the back-stress ratio follow the above expressions.

Plastic modulus

The plastic modulus in the multi-axial generalized form of Dafalias and Manzari (2004), after substituting in their expression for the hardening coefficient, can be expressed as,

$$K_p = \frac{2}{3} G \, h_o \left[\frac{1+e}{(2.97-\text{e})^2} (1-C_h e) \right] \frac{(\boldsymbol{\alpha}^b - \boldsymbol{\alpha}):\boldsymbol{n}}{(\boldsymbol{\alpha} - \boldsymbol{\alpha}_{in}):\boldsymbol{n}} \tag{36}$$

where h_o and C_h are scalar parameters and e is the void ratio. Setting aside the secondary influence of void ratio, this form illustrates that K_p is proportional to G, proportional to the distance of the back-stress ratio to the bounding back-stress ratio, and inversely proportional to the distance of the back-stress ratio from the initial back-stress ratio.

The plastic modulus relationship was revised in the model presented herein to provide an improved approximation of empirical relationships for secant shear modulus and equivalent damping ratios during drained strain-controlled cyclic loading. The plastic modulus is computed as,

$$K_p = G \, h_o \, \frac{\left[(\boldsymbol{\alpha}^b - \boldsymbol{\alpha}):\boldsymbol{n} \right]^{0.5}}{\left[\exp\left[(\boldsymbol{\alpha} - \boldsymbol{\alpha}_{in}^{app}):\boldsymbol{n} \right] - 1 \right] + C_{\gamma 1}} C_{rev} \tag{37}$$

$$C_{rev} = \frac{(\boldsymbol{\alpha} - \boldsymbol{\alpha}_{in}^{app}):\boldsymbol{n}}{(\boldsymbol{\alpha} - \boldsymbol{\alpha}_{in}^{true}):\boldsymbol{n}} \quad for \quad (\boldsymbol{\alpha} - \boldsymbol{\alpha}_{in}^{p}):\boldsymbol{n} \leq 0$$
$$= 1 \quad otherwise \tag{38}$$

The factor C_{rev} accounts for the effect of unload-reload cycles as discussed in Section 2.5 and illustrated in Figures 2.4 and 2.5. The constant $C_{\gamma 1}$ in the denominator serves to avoid division by zero and has a slight effect on the nonlinearity and damping at small shear strains. If $C_{\gamma 1} = 0$, then the value of K_p will be infinite at the start of a loading cycle because $(\boldsymbol{\alpha} - \boldsymbol{\alpha}_{in}):\boldsymbol{n}$ will also be zero. In that case, nonlinearity will become noticeable only after $(\boldsymbol{\alpha} - \boldsymbol{\alpha}_{in}):\boldsymbol{n}$ becomes large enough to reduce K_p closer to the value of G (e.g., K_p/G closer to 100 or 200). Setting the value of $C_{\gamma 1} = h_o/200$ produces a reasonable response as will be demonstrated later with examples of modulus reduction and equivalent damping ratios. For stress ratios outside the bounding surface [i.e., loose-of-critical states with $(\boldsymbol{\alpha}^b - \boldsymbol{\alpha}):\boldsymbol{n} < 0$], the plastic modulus is set to zero rather than allowing for negative values. This restriction on the plastic modulus improved numerical stability while having little effect on computed stress-strain responses. The plastic modulus is further modified for the effects of fabric and fabric history, as described in a later section.

25

Plastic volumetric strains – Dilation

Plastic volumetric strains are related to plastic deviatoric strains through the dilatancy D (Equations 29 and 30), which is computed in the Dafalias and Manzari (2004) model and the base component of the model presented herein (with additional fabric effects described in a later section) as,

$$D = A_{do} \cdot \left[\left(\alpha^d - \alpha \right) : n \right] \tag{39}$$

Note that dilation (increasing void ratio) occurs whenever the term $(\alpha^d - \alpha):n$ is less than zero whereas contraction (decreasing void ratio) occurs when it is positive.

The constant A_{do} in this relationship can be related to the dilatancy relationship proposed by Bolton (1986), which follows from the work of Rowe (1962), through the following sequence of steps. Bolton showed that the difference between peak and constant volume friction angles could be approximated as,

$$\phi_{pk} - \phi_{cv} = -0.8\psi \tag{40}$$

with

$$\psi = \tan^{-1}\left(\frac{d\varepsilon_v^{pl}}{\left| d\gamma^{pl} \right|} \right) \tag{41}$$

Since $\psi \approx \tan(\psi)$ for ψ less than about 0.35 radians (20 degrees), the difference between peak and constant volume friction angles (in radians) can be approximated as,

$$\phi_{pk} - \phi_{cv} = -0.8\frac{d\varepsilon_v^{pl}}{\left| d\gamma^{pl} \right|} = -0.8\sqrt{\frac{1}{2}}D \tag{42}$$

The peak friction angle is mobilized at the bounding surface, so this can be written as,

$$\phi_{pk} - \phi_{cv} = -0.8\sqrt{\frac{1}{2}}A_{do} \cdot \left[\left(\alpha^d - \alpha \right) : n \right]$$

$$\phi_{pk} - \phi_{cv} = -0.8\sqrt{\frac{1}{2}}A_{do} \cdot \left[\left(\frac{M^d}{\sqrt{2}}n - \frac{M^b}{\sqrt{2}}n \right) : n \right] \tag{43}$$

The term $n:n$ is equal to unity, and the values of ϕ_{pk} and ϕ_{cv} (again in radians) can be replaced with expressions in terms of M^b and M as,

$$\sin^{-1}\left(\frac{M^b}{2}\right) - \sin^{-1}\left(\frac{M}{2}\right) = 0.4 A_{do} \cdot \left[M^b - M^d \right] \tag{44}$$

This expression can then be rearranged to solve for Ado as,

$$A_{do} = \frac{1}{0.4} \frac{\sin^{-1}\left(\dfrac{M^b}{2}\right) - \sin^{-1}\left(\dfrac{M}{2}\right)}{M^b - M^d} \tag{45}$$

where the angles returned by the sin^{-1} functions are in radians.

The parameter A_{do} should thus be chosen to be consistent with the n^d and n^b terms that control M^b, and M^d. For example, setting the parameters n^b and n^d equal to 0.5 and 0.1, respectively, results in A_{do} varying from 1.26 for ξ_R = -0.1 to 1.45 for ξ_R = -0.7. A default value for A_{do} is computed based on the above expression using the conditions at the time of model initialization in FLAC (as described in a later section). If an alternative value for A_{do} is manually input as a property of the model, then the default value will be deactivated.

Alternatively, the stress ratio terms can be replaced with friction angles (in radians) as follows,

$$\begin{aligned}
\phi_{pk} - \phi_{cv} &= 0.4 A_{do} \cdot \left[M^b - M^d \right] \\
\phi_{pk} - \phi_{cv} &= 0.4 A_{do} \cdot \left[M \exp(-n^b \xi_R) - M \exp(n^d \xi_R) \right] \\
\phi_{pk} - \phi_{cv} &= 0.4 A_{do} \cdot \left[2\sin(\phi_{pk}) - 2\sin(\phi_d) \right] \\
\phi_{pk} - \phi_{cv} &= 0.8 A_{do} \cdot \left[\sin(\phi_{pk}) - \sin(\phi_d) \right]
\end{aligned} \tag{46}$$

The sine terms can be replaced with Taylor series, which are quite accurate with just the first two terms as,

$$\sin(\phi) = \phi - \frac{(\phi)^3}{3!} \tag{47}$$

Substituting the Taylor series in the above equation gives,

$$\phi_{pk} - \phi_{cv} = 0.8 A_{do} \left[\left(\phi_{pk} - \frac{\left(\phi_{pk}\right)^3}{3!} \right) - \left(\phi_d - \frac{\left(\phi_d\right)^3}{3!} \right) \right] \tag{48}$$

The parameter A_{do} can then be solved for as,

$$A_{do} = \frac{\phi_{pk} - \phi_{cv}}{0.8 \left[\phi_{pk} - \phi_d - \frac{\left(\phi_{pk}\right)^3 - \left(\phi_d\right)^3}{6} \right]} \tag{49}$$

where the friction angles in the above expression are in radians. This expression provides an alternative view of how the parameter A_{do} relates to friction angles for a given set of n^b and n^d terms that control ϕ_{pk} and ϕ_d, respectively. For example, consider the case with the parameters n^b and n^d equal to 0.5 and 0.1, respectively, and assuming ϕ_{cv} = 33 degrees. For ξ_R = -0.1, we would obtain ϕ_d = 32.6 degrees, ϕ_{pk} = 34.9 degrees, and A_{do} = 1.26. For ξ_R = -0.7, we would obtain ϕ_d = 30.5 degrees, ϕ_{pk} = 50.6 degrees, and A_{do} = 1.45.

Plastic volumetric strains – Contraction

Plastic volumetric strains during contraction (i.e., whenever ($\boldsymbol{\alpha}^{\mathbf{d}}$ - $\boldsymbol{\alpha}$):$\mathbf{n}$ is greater than zero) are computed in the Dafalias and Manzari (2004) model using the same expression as used for dilatancy,

$$D = A_{do} \cdot \left[\left(\boldsymbol{\alpha}^d - \boldsymbol{\alpha} \right) : \boldsymbol{n} \right] \tag{50}$$

The use of this expression was found to limit the ability of the model to approximate a number of important loading responses; e.g., it greatly overestimated the slope of the cyclic resistance ratio (CRR) versus number of equivalent uniform loading cycles for undrained cyclic element tests (e.g., Figure 1.3).

Plastic volumetric strains during contraction for the model presented herein are computed using the following expression,

$$D = A_{dc} \cdot \left[\left(\boldsymbol{\alpha} - \boldsymbol{\alpha}_{in}^{app} \right) : \boldsymbol{n} + C_{in} \right]^2 \frac{\left(\boldsymbol{\alpha}^d - \boldsymbol{\alpha} \right) : \boldsymbol{n}}{\left(\boldsymbol{\alpha}^d - \boldsymbol{\alpha} \right) : \boldsymbol{n} + C_D} \tag{51}$$

$$A_{dc} = \frac{A_{do}}{h_p} \tag{52}$$

The various forms in the above relationships were developed to improve different aspects of the calibrated model's performance. The value of D was set proportional to the square of $((\alpha - \alpha^{in}):\mathbf{n} + C_{in})$ to improve the slope of the relationship between CRR and number of uniform loading cycles. The C_{in} term depends on fabric and is described in a later section along with other modifications to the above expression for the effects of fabric and fabric history. The inclusion of the term C_{in} improves the stress paths for undrained cyclic loading and the volumetric strain response during drained cyclic loading. Inclusion of this constant enables some volumetric strain to develop early in the unloading from a point outside the dilatancy surface (as described later). The remaining terms on the right-hand side of the equation were chosen to be close to unity over most of the loading range, while ensuring that D smoothly goes to zero as α approaches α^d; reasonable results were obtained using a C_D value of 0.10.

The parameter A_{dc} for contraction was related to the value of A_{do} for dilation by dividing it by a parameter h_p that can be varied during the calibration process to obtain desired cyclic resistance ratios. The effect of confining stress on cyclic loading behavior was then conveniently incorporated by making h_p depend on ξ_R, with the following form chosen so that the model produces results consistent with the design K_σ relationships presented earlier in Figure 1.4.,

$$h_p = h_{po} \exp\left(-0.7 + 7.0\left(0.5 - \xi_R\right)^2\right) \quad for \quad \xi_R \leq 0.5 \tag{53}$$

$$h_p = h_{po} \exp\left(-0.7\right) \quad for \quad \xi_R > 0.5 \tag{54}$$

Thus, the scalar constant h_{po} provides a linear scaling of contraction rates while the functional form of the remaining portion in Equations (53) and (54) is what controls the effect of overburden stress on CRR. The variation of h_p with ξ_R for different values of h_{po} is plotted in Figure 2.7. Once the other input parameters have been selected, the constant h_{po} can be calibrated to arrive at a desired cyclic resistance ratio.

An upper limit was imposed on the contraction rate, with the limiting value computed as,

$$D \leq 1.5 \cdot A_{do} \frac{\left(\boldsymbol{\alpha}^d - \boldsymbol{\alpha}\right):\mathbf{n}}{\left(\boldsymbol{\alpha}^d - \boldsymbol{\alpha}\right):\mathbf{n} + C_D} \tag{55}$$

This limit prevented numerical issues that were encountered with excessively large contraction rates. It does not appear to have limited the ability of the model to recreate realistic contraction rates as illustrated in the calibration examples shown later.

2.8 Fabric effects

Dafalias and Manzari (2004) introduced a fabric-dilatancy tensor ($\mathbf{z}$) that could be used to account for the effects of prior straining. Their fabric tensor ($\mathbf{z}$) evolved in response to plastic volumetric dilation strains, according to,

$$dz = -c_z \left\langle -d\varepsilon_v^{pl} \right\rangle \left(z_{max}\mathbf{n} + \mathbf{z} \right) \tag{56}$$

where the parameter c_z controls the rate of evolution and z_{max} is the maximum value that $\mathbf{z}$ can attain.

The fabric-dilatancy tensor was modified for the present model as,

$$dz = -\frac{c_z}{1 + \left\langle \dfrac{z_{cum}}{2z_{max}} - 1 \right\rangle} \frac{\left\langle -d\varepsilon_v^{pl} \right\rangle}{D} \left(z_{max}\mathbf{n} + \mathbf{z} \right) \tag{57}$$

In this expression, the tensor $\mathbf{z}$ evolves in response to plastic deviatoric strains that occur during dilation only (i.e., dividing the plastic volumetric strain by the dilatancy gives plastic shear strain). In addition, the evolution of fabric is restricted to only occur when $(\boldsymbol{\alpha}^\mathbf{d} - \boldsymbol{\alpha})$:$\mathbf{n} < 0$; this additional constraint precludes fabric evolution during dilation above the rotated dilatancy surface (introduced later) but below the non-rotated dilatancy surface. The parameter z_{cum} is the cumulative value of absolute changes in $\mathbf{z}$ computed according to,

$$dz_{cum} = |dz| \tag{58}$$

The rate of evolution for $\mathbf{z}$ therefore decreases with increasing values of z_{cum}, which enables the undrained cyclic stress-strain response to progressively accumulate shear strains rather than lock-up into a repeating stress-strain loop. In addition, the greatest past peak value (scalar amplitude) for $\mathbf{z}$ during its loading history is also tracked,

$$z_{peak} = \max \left(\sqrt{\frac{\mathbf{z}:\mathbf{z}}{2}}, z_{peak} \right) \tag{59}$$

The values of $\mathbf{z}$, z_{peak}, and z_{cum} are later used to facilitate the accumulation of shear strains under symmetric loading through their effects on the plastic modulus and dilatancy relationships.

The evolution of the fabric tensor terms is illustrated in Figure 2.8 and Figure 2.9 showing the response of a loose sand to undrained cyclic DSS loading without any sustained horizontal shear stress (Figure 2.8) and with a sustained horizontal shear stress (Figure 2.9). These figures show the stress path and stress-strain response of the sand, along with time histories for the back-stress ratios and fabric tensor terms. Note how the fabric terms do not grow until the soil reaches the dilatancy surface, and

30

how the stress-ratios are limited by the bounding stress ratio. There is no horizontal shear stress reversal for the case shown in Figure 2.9 and thus the back-stress ratio and fabric terms do not reverse either.

Additional memory of fabric formation history

Memory of the fabric formation history was included in the model presented herein to improve the ability of the model to account for the effects of sustained static shear stresses and account for differences in fabric effects for various drained versus undrained loading conditions.

The initial fabric tensor ($\mathbf{z}_{in}$) at the start of the current loading path is determined whenever a stress ratio reversal occurs. The $\mathbf{z}_{in}$ tracks the immediate history terms without any consideration of whether an earlier loading cycle had produced greater degrees of fabric (i.e., the logic is different from that adopted for the updating of back-stress ratio history terms). This history term is used for describing the degree of stress rotation and its effects on plastic modulus, as described later.

Another aspect of the fabric history that is tracked is the mean stress at which the fabric is formed. This aspect of fabric history is tracked by tracking the product of $\mathbf{z}$ and p, and defining p_{zp} as the mean stress at the time that this product achieves its greatest peak value. The p_{zp} is used in addressing a couple of issues, including the issue of how fabric that is formed during liquefaction may be erased during reconsolidation. For example, a saturated sand that develops cyclic mobility behavior during undrained cyclic loading clearly remembers its history of plastic deviatoric strains and then subsequently forgets (to a large extent) this prior strain history when it reconsolidates back to its pre-earthquake confining stress. As another example, the memory of prior strains during undrained cyclic loading is very different than the memory of prior strains during drained cyclic loading. This memory conceptually could be related to the history of plastic and total volumetric strains, but a simpler method to account for this effect is to consider how the mean stress p relates to the value of p_{zp}. Conceptually, it appears that prior strain history (or fabric) is most strongly remembered when the soil is operating under mean stresses that are smaller than those that existed when the fabric was formed (i.e., $p \ll p_{zp}$) and then largely forgotten when they are of the same order (i.e., $p \approx p_{zp}$). This attribute will be used in the relationships described later for describing the effects of fabric on dilatancy.

Effect of fabric on plastic modulus

An effect of fabric on the plastic modulus was added to the model presented herein by reducing the plastic modulus as the fabric tensor increased in peak amplitude, as follows:

$$K_p = G \cdot h_o \cdot \frac{\left[\left(\boldsymbol{\alpha}^b - \boldsymbol{\alpha}\right):\boldsymbol{n}\right]^{0.5}}{\left[\exp\left(\left(\boldsymbol{\alpha} - \boldsymbol{\alpha}_{in}^{app}\right):\boldsymbol{n}\right)-1\right]+C_{\gamma 1}} C_{rev}$$
$$\cdot \frac{C_{K\alpha}}{1+C_{K_p}\left(\dfrac{z_{peak}}{z_{max}}\right)\left\langle\left(\boldsymbol{\alpha}^b - \boldsymbol{\alpha}\right):\boldsymbol{n}\right\rangle\sqrt{1-C_{zpk2}}} \tag{60}$$

where,

31

$$C_{K\alpha} = 1 + \frac{C_{K\alpha f}}{1 + \left(2.5\left\langle\left(\boldsymbol{\alpha} - \boldsymbol{a}_{in}^{true}\right):\boldsymbol{n}\right\rangle\right)^2} \, C_{pzp2} \, C_{zpk1} \tag{61}$$

$$C_{zpk1} = \frac{z_{peak}}{z_{cum} + \dfrac{z_{max}}{5}} \tag{62}$$

$$C_{zpk2} = \frac{z_{peak}}{z_{cum} + \dfrac{z_{max}}{100}} \tag{63}$$

$$C_{pzp2} = \frac{-\left\langle-\left(p_{zp} - p\right)\right\rangle}{-\left\langle-\left(p_{zp} - p\right)\right\rangle + p_{\min}} \tag{64}$$

The above expressions produce a reduction in plastic modulus when fabric is favorable ($\boldsymbol{z}:\boldsymbol{n} \geq 0$) and with increasing plastic shear strains (which conceptually would break down any cementation). This reduces both the plastic modulus and the hysteretic damping at larger shear strains (note that $z_{peak} = 0$ unless the soil has been loaded strongly enough to pass outside the dilatancy surface), improves the volumetric strains that develop in drained cyclic loading, and improves the path in undrained cyclic loading.

The $C_{K\alpha}$ and square root of ($1-C_{zpk2}$) terms both serve to increase K_p during non-reversal loading by amounts that depend on the fabric and stress history. During reversal loading, the ($1-C_{zpk2}$) term approaches unity and K_p evolves as it previously had. The roles of each of the other terms are discussed below.

C_{zpk1} and C_{zpk2} are terms that start from zero and grow to be unity for uni-directional growth of fabric which is the case during non-reversing loading conditions. These two terms differ by the rate under which they approach unity by the use of the constant $z_{max}/5$ or $z_{max}/100$ with these respective values chosen for their ability to better approximate the engineering behaviors of interest and correlations. For full reversal loading where the fabric alternates between positive and negative values, these terms will both go to zero.

C_{pzp2} starts initially at zero and stays equal to zero until fabric is formed. After fabric is formed, this term quickly transitions to unity for values of mean effective stress p that are less than the value that p had when the maximum fabric was formed (p_{zp}). If p increases beyond the value of p_{zp} the term will return to zero according to the Macaulay brackets.

The values for the calibration parameters C_{Kp} and $C_{K\alpha f}$ were chosen for their ability to reasonably approximate the targeted behaviors, as discussed later. Setting C_{Kp} to a default value of 2.0 was found to produce reasonable responses with particular emphasis on improving (reducing) the equivalent damping ratios at shear strains of 1 to 3% in drained cyclic loading. The parameter $C_{K\alpha f}$ is particularly useful for adjusting the undrained cyclic loading response with sustained static shear stresses; a default calibration which depends on D_R is presented later.

The cumulative effect of the above parameters can be understood as follows. If a soil is strongly loaded in uni-directional loading and forms significant amount of fabric and is then unloaded, then upon subsequent reloading the terms C_{pzp2} and C_{zpk1} will be unity and $C_{K\alpha}$ will become large. If the loads are increased to where the soil is being sheared and forming fabric at even higher stresses (higher values of p than fabric was previously formed at) then $C_{K\alpha}$ will be unity ($C_{pzp2} = 0$). In this way, an element that has developed strong fabric under monotonic or cyclic loading without reversal of the total shear stress direction (e.g., an element within a steep slope where the static shear stresses are greater than the cyclic shear stresses) will, when unloaded and reloaded, be initially much stiffer (increased K_p) followed by a softening (smaller K_p) if the soil is loaded into virgin territory.

Effect of fabric on plastic volumetric dilation

A rotated dilatancy surface with slope M^{dR} which evolves with the history of the fabric tensor $\mathbf{z}$ was added to the framework of the model to facilitate earlier dilation at low stress ratios under certain loading paths (Ziotopoulou 2014, Ziotopoulou and Boulanger 2016). The rotated surface, schematically illustrated in Figure 2.10 as a line in q-p space and Figure 2.11 as a circular surface on a stress-ratio graph of r_{yy} versus r_{xy}, is equal to the original dilatancy surface scaled-down by a factor C_{rot1},

$$M^{dR} = \frac{M^d}{C_{rot1}}$$

(65)

$$C_{rot1} = 1 + \frac{2 \cdot \langle -\mathbf{z} : \mathbf{n} \rangle}{\sqrt{2} z_{max}} \left(1 - C_{zin1}\right) \geq 1$$

(66)

where M^d is the slope of the unrotated dilatancy surface. Experimental results (Ziotopoulou 2014, Ziotopoulou and Boulanger 2016) indicate that the loading history, the loading direction and the loading pattern play important roles in the response of the soil to irregular cyclic loading. Thus the scaling factor that defines the rotated dilatancy surface was made dependent on whether fabric is favorable ($\mathbf{z} : \mathbf{n} > 0$) or unfavorable ($\mathbf{z} : \mathbf{n} < 0$) and on the factor C_{zin1} which is an indirect measure of whether there are reversals or not,

$$C_{zin1} = \left\langle 1 - \exp\left(-2.0 \left| \frac{\mathbf{z}_{in} : \mathbf{n} - \mathbf{z} : \mathbf{n}}{z_{max}} \right| \right) \right\rangle$$

(67)

where $\mathbf{z_{in}}$ is the fabric tensor at the beginning of the current loading branch. C_{zin1} can take values ranging from 0, when there are no reversals, to 1, when there are reversals. The rotated dilatancy surface is operating only for loading with an unfavorable fabric since the factor C_{rot1} becomes 1 when the fabric is favorable (i.e., $\langle -\mathbf{z} : \mathbf{n} \rangle = 0$).

A back-stress ratio tensor for the rotated dilatancy surface (α^{dR}) was introduced as,

$$\alpha^{dR} = \frac{1}{\sqrt{2}} \left(M^{dR} - m\right) \mathbf{n}$$

(68)

Dilation occurs whenever the term $(\boldsymbol{\alpha}^{dR} - \boldsymbol{\alpha}) : \mathbf{n}$ is negative whereas contraction occurs when it is positive. The calculation of D is still treated separately during dilation and contraction.

D during dilation is now computed according to the following expressions. First, a value for D is computed from the rotated dilatancy surface,

$$D_{rot} = A_d \frac{\langle -\mathbf{z} : \mathbf{n} \rangle}{\sqrt{2} z_{max}} \frac{(\alpha^{dR} - \alpha) : \mathbf{n}}{C_{DR}} \tag{69}$$

where the C_{DR} factor is applied to reduce the rate under which dilatancy is increasing and is discussed further below. Second, another value for D is computed that would be obtained from the non-rotated dilatancy surface,

$$D_{non-rot} = A_d \cdot \left(-\langle -(\boldsymbol{\alpha}^d - \boldsymbol{\alpha}) : \mathbf{n} \rangle \right) \tag{70}$$

The Macaulay brackets in the above expression ensure that $D_{non\text{-}rot}$ is equal to zero whenever $(\boldsymbol{\alpha}^d - \boldsymbol{\alpha}) : \mathbf{n} > 0$ while $(\boldsymbol{\alpha}^{dR} - \boldsymbol{\alpha}) : \mathbf{n} < 0$. Lastly, the operating value of D is selected from the above two values based on,

$$if \quad D_{non-rot} < D_{rot} \quad \Rightarrow \quad D = D_{non-rot}$$

$$else \quad D = D_{non-rot} + \left(D_{rot} - D_{non-rot} \right) \cdot \frac{\langle M^b - M^{cur} \rangle}{\langle M^b - M^{cur} + 0.01 \rangle} \tag{71}$$

The above logic is illustrated in Figure 2.12 where D is plotted for a half-cycle of loading that goes from contraction to dilation. This figure shows that $D_{non\text{-}rot}$ is used whenever it is smaller (more negative) than D_{rot}. For cases where D_{rot} is smaller than $D_{non\text{-}rot}$, the value of D is interpolated based on the additional term on the right that multiplies the difference between D_{rot} and $D_{non\text{-}rot}$. This interpolation term is close to unity for stress ratios away from the bounding surface ($M^{cur} < M^b$), such that D will be equal to D_{rot} as illustrated in the figure. However, this term will also go smoothly to zero as the stress ratio gets close to the bounding surface, so that dilatancy smoothly goes to zero as a soil approaches the critical state where $M = M^d = M^b$. The constant of 0.01 in the denominator controls the rate under which D goes to zero as the stress ratio nears the bounding surface and was found to provide reasonable results in trial simulations.

The factor C_{DR} in the denominator of the expression for D_{rot} is applied so that the D computed based on the rotated dilatancy surface is consistent with experimental observations. Its value, for the default calibration described later, has been made dependent on the initial D_R of the soil.

Lastly, the parameter A_d in the expressions for both D_{rot} and $D_{non\text{-}rot}$ is expressed as,

$$A_d = \frac{A_{do}\left(C_{zin2}\right)}{\left(\dfrac{z_{cum}^2}{z_{max}}\right)\left(1 - \dfrac{\langle -\mathbf{z} : \mathbf{n} \rangle}{\sqrt{2} \cdot z_{peak}}\right)^3 \left(C_\varepsilon\right)^2 \left(C_{pzp}\right)\left(C_{pmin}\right)\left(C_{zin1}\right) + 1} \tag{72}$$

$$C_{pzp} = \frac{1}{1 + \left(\frac{2.5p}{p_{zp}} \right)^5} \tag{73}$$

$$C_{pmin} = \frac{1}{1 + \left(\frac{p_{min2}}{p} \right)^2} \tag{74}$$

$$C_{zin1} = \left\langle 1 - \exp\left(-2.0 \left| \frac{z_{in} : \boldsymbol{n} - \boldsymbol{z} : \boldsymbol{n}}{z_{max}} \right| \right) \right\rangle \tag{75}$$

$$C_{zin2} = \frac{1 + C_{zin1} \dfrac{z_{cum} - z_{peak}}{3z_{max}}}{1 + 3C_{zin1} \dfrac{z_{cum} - z_{peak}}{3z_{max}}} \tag{76}$$

Consider the six terms added to the denominator of the expression for A_d. The first term $[z_{cum}^2/z_{max}]$ facilitates the progressive growth of strains under symmetric loading by reducing the dilatancy that occurs when a liquefied soil has been sheared through many cycles of loading; note that this term progressively increases with subsequent cycles of loading. The second term facilitates strain-hardening when the plastic shear strain reaches the prior peak value, wherein the term approaches zero (i.e., when $\boldsymbol{z}:\boldsymbol{n}$ approaches $z_{peak}\sqrt{2}$) and the dilation rate consequently rapidly approaches the virgin loading value of A_{do}. The third term C_ε is a calibration constant that can be used to modify the rate of plastic shear strain accumulation. The fourth term C_{pzp} causes the effects of fabric on dilation to be diminished (erased) whenever the current value of p is near the value of p_{zp}; this term enables the model to provide reasonable predictions of responses to large numbers of either drained or undrained loading cycles. The fifth term C_{pmin} provides a minimum amount of shear resistance for a soil after it has temporarily reached an excess pore pressure ratio of 100%; This term is almost zero when p'=0, such that the soil will initially dilate until some minimum p' has developed, after which the term quickly approaches 1.0. The parameter p_{min2} is currently set to become equal to 5% of the value of p' at consolidation (which is the value that exists when the flag FirstCall –see Section 3– was last set equal to 0), with the minimum value of p_{min2} being 10 times the minimum value of p' (i.e., p_{min} = 1/200 times the larger of p_A or the value of p' at consolidation). The sixth term C_{zin1} facilitates strain-hardening when stress reversals are not causing fabric changes; i.e., when the initial and current fabric terms are close to equal, the term C_{zin1} goes to zero. Lastly, the second term in the numerator, C_{zin2}, causes the dilatancy to be decreased by up to a factor of 3 under conditions of large strains and full stress (and fabric) reversals, which improves the prediction of cyclic strain accumulation during undrained cyclic loading.

An additional constraint is placed on D during dilation at very low effective stresses. For $p < 2p_{min}$, the value of D cannot be smaller in magnitude than computed by the following expression,

35

$$D = -3.5 A_{do} \left\langle M^b - M^d \right\rangle \frac{2 p_{\min} - p}{p_{\min}} \quad for \quad p_{\min} \le p \le 2 p_{\min} \tag{77}$$

This expression ensures that the model will, for dense-of-critical soils (i.e., $M^b > M^d$), be dilative when p falls below $2p_{\min}$.

Effect of fabric on plastic volumetric contraction

Dafalias and Manzari (2004) used the fabric tensor to modify the dilatancy during contraction ($D > 0$) as follows,

$$D = A_d \left[\left(\boldsymbol{\alpha}^d - \boldsymbol{\alpha} \right) : \boldsymbol{n} \right] \left(1 + \langle \boldsymbol{z} : \boldsymbol{n} \rangle \right) \tag{78}$$

This relationship enhances the volumetric contraction whenever the fabric is favorable ($\boldsymbol{z:n} \ge 0$), based on the term $1+\langle\boldsymbol{z:n}\rangle$ as recommended by Dafalias and Manzari (2004).

The effect of fabric on dilatancy during contraction was modified for the present model as,

$$D = A_{dc} \cdot \left[\left(\boldsymbol{\alpha} - \boldsymbol{\alpha}_{in}^{app} \right) : \boldsymbol{n} + C_{in} \right]^2 \frac{\left(\boldsymbol{\alpha}^d - \boldsymbol{\alpha} \right) : \boldsymbol{n}}{\left(\boldsymbol{\alpha}^d - \boldsymbol{\alpha} \right) : \boldsymbol{n} + C_D} C_{p\min 2} \tag{79}$$

$$A_{dc} = \frac{A_{do} \left(1 + \langle \boldsymbol{z} : \boldsymbol{n} \rangle \right)}{h_p C_{dz}} \tag{80}$$

$$C_D = 0.1 \tag{81}$$

$$C_{in} = \frac{2 \cdot \langle \boldsymbol{z} : \boldsymbol{n} \rangle}{\sqrt{2} z_{\max}} \tag{82}$$

$$C_{dz} = \left(1 - C_{rot2} \cdot \frac{\sqrt{2} z_{peak}}{z_{\max}} \right) \cdot \left(\frac{z_{\max}}{z_{\max} + C_{rot2} \cdot z_{cum}} \right) \ge \frac{1}{1 + \frac{z_{\max}}{2}} \tag{83}$$

$$C_{rot2} = 1 - \frac{z_{peak}}{z_{cum} + \frac{z_{max}}{100}} \left(= 1 - C_{zpk2} \right) \tag{84}$$

$$C_{p\min 2} = 0 \quad for \quad p \le 2 p_{\min}$$
$$C_{p\min 2} = 1 \quad for \quad p \ge 18 p_{\min}$$
$$C_{p\min 2} = \frac{p - 2 p_{\min}}{16 p_{\min}} \quad otherwise \tag{85}$$

The factor C_{in} in the expression for D has been modified so it now depends on fabric; C_{in} is zero for unfavorable fabric, and increases with increasing **z:n** for favorable fabric to enhance the contraction rate at the start of an unloading cycle (note that D would be zero at the start of an unloading cycle if C_{in} was zero).

The term C_{dz} in the denominator of the expression for A_{dc} serves to increase the rate of contraction as z_{peak} nears z_{max} or as a large amount of cumulative fabric formation/destruction has taken place. This term was developed for improved modeling of the cyclic strength of denser sands, for which the value of h_p can be on the order of 100 (Figure 2.7). The degrading of the denominator as z_{peak} or z_{cum} increases enables the generation of high excess pore pressures at higher loading levels, and controls the slope of the CRR versus number of uniform loading cycles relationship obtained for undrained element loading. Note that the denominator degrades whether fabric is favorable or not, but that the overall rate of contraction is more enhanced if the fabric is favorable (**z:n** ≥ 0). The factor C_{rot2} was introduced into the factor C_{dz} to provide better control over the rate of contraction as z_{peak} nears z_{max} or as a large amount of cumulative fabric formation/destruction has taken place. The factor C_{rot2} takes values that range from 1 for loading with zero fabric or cyclic loading that causes reversals of fabric (since z_{cum} will become much larger than z_{peak}), to 0 for loading that causes fabric to grow monotonically in one direction such as in non-reversal cyclic loading (since z_{cum} will equal z_{peak}). Lastly, the limit on the minimum value of C_{dz} is required for avoiding division by zero and to avoid over-estimating contraction rates (i.e., small values of h_p and large values of z_{peak} or z_{cum}).

The term C_{pmin2} slows the rate of contraction when p is approaching its minimum allowable value, and stops further contraction when p is less than twice the minimum allowable p.

Effect of fabric on the elastic modulus

The elastic shear modulus and elastic bulk modulus may degrade with increasing values of cumulative plastic deviator strain term, z_{cum}. This component of the model was added to account for the progressive destruction, with increasing plastic shear strains, of any minor cementation bonds or other ageing- or strain history-related phenomena that produced an increase in small-strain shear modulus. The destruction of minor cementation by plastic shear strains is evidenced in the field by measurements of shear wave velocities in sand that are lower after earthquake shaking than before earthquake shaking (e.g., Arai 2006). The degradation of the elastic shear modulus is computed as,

$$G = G_o p_A \left(\frac{p}{p_A} \right)^{1/2} C_{SR} \left(\frac{1 + \dfrac{z_{cum}}{z_{max}}}{1 + \dfrac{z_{cum}}{z_{max}} C_{GD}} \right) \tag{86}$$

where C_{GD} is the factor by which the shear modulus is degraded (divided) at very large values of z_{cum}. This change in the elastic shear modulus G causes the bulk modulus K to progressively decrease with increasing z_{cum}. The change in K improves the model's ability to track the stress-strain response of liquefying sand. In particular, decreasing K with increasing z_{cum} reduces the rate of strain-hardening after phase transformation at larger shear strain levels, and improves the ability to approximate the hysteretic stress-strain response of a soil as it liquefies.

Effect of fabric on peak mobilized friction angles in drained and undrained loading

Kutter and Chen (1997) showed that plastic dilation rates are different in drained and undrained loading of the same clean sand, with the consequence being that the peak mobilized friction angles are also different for drained and undrained loading. This aspect of behavior would appear to be contradictory to having a bounding surface that is only dependent on the relative state of the sand (i.e., through the parameter n^b) if the mobilized friction angles for drained and undrained loading paths are both controlled by the bounding surface. The model presented herein produces the same peak mobilized friction angles for drained and undrained loading because both conditions become limited by the same bounding surface. This aspect of behavior deserves closer examination in future efforts.

2.9 Post-shaking reconsolidation

Volumetric strains that develop during post-liquefaction reconsolidation of sand are difficult to numerically model using the conventional constitutive separation of strains into elastic and plastic components since a large portion of the post-liquefaction reconsolidation strains are due to sedimentation effects which are not easily incorporated into either the elastic or plastic components of behavior. Single element simulations using various constitutive models show that they generally predict post-liquefaction reconsolidation strains that are an order of magnitude smaller than observed in various experimental studies (e.g., Ziotopoulou and Boulanger 2013b, Howell et al. 2014).

The present model was modified to provide more realistic estimates of reconsolidation strains during the post-shaking portion of a numerical simulation. The modification involved the pragmatic approach of reducing the post-shaking elastic shear modulus G (and hence elastic bulk modulus K) which increases reconsolidation strains, thereby compensating for the sedimentation strains which are not explicitly modeled. The user may activate this feature after the end of strong shaking, such that post-liquefaction reconsolidation strains are better approximated in the remainder of the simulation. This feature should not be activated for the strong shaking portion of a simulation.

The post-shaking elastic moduli are determined by multiplying the conventional elastic moduli (computed using the expressions described earlier) by a reduction factor F_{sed} as,

$$G_{post-shaking} = F_{sed}G \tag{87}$$

$$K_{post-shaking} = F_{sed}K \tag{88}$$

The F_{sed} value is computed as,

$$F_{sed} = F_{sed,min} + \left(1 - F_{sed,min}\right)\left(\frac{p'}{20p'_{sed}}\right)^2 \leq 1 \tag{89}$$

$$p'_{sed} = p'_{sed_o} \left(\frac{z_{cum}}{z_{cum} + z_{max}} \right) \left\langle 1 - \frac{M^{cur}}{M^d} \right\rangle^{0.25} \tag{90}$$

$$F_{sed,min} = 0.04 \tag{91}$$

$$p'_{sed_o} = -\frac{P_{atm}}{5} \tag{92}$$

where the constant value $F_{sed,min}$ represents the smallest value that F_{sed} can attain, and the parameter $p'_{sed,o}$ is the mean effective stress up to which reconsolidation strains are enhanced. The value of F_{sed} progressively reduces from unity toward the value of $F_{sed,min}$ as z_{cum} progressively increases and provided that M^{cur} is less than M^d. Setting $F_{sed,min}$ to 0.04 was found to produce reasonable responses as shown later. The user can select other values for $p'_{sed,o}$ and $F_{sed,min}$.

2.10 Summary of constitutive equations

The constitutive equations for the model presented herein are summarized in Table 2.1 along with the equations for the Dafalias and Manzari (2004) model.

Table 2.1. Comparison of constitutive equations

Dafalias-Manzari (2004) model	Present model
Critical state line $$e_c = e_o - \lambda \left(\frac{p_{cs}}{p_A} \right)^{\xi}$$	*Critical state line* $$\xi_R = \frac{R}{Q - \ln\left(100 \frac{p}{p_A} \right)} - D_R$$
Elastic deviatoric strain increment $$de^{el} = \frac{ds}{2G}$$ $$G = G_o p_A \frac{(2.97 - e)^2}{1 + e} \left(\frac{p}{p_A} \right)^{1/2}$$	*Elastic deviatoric strain increment* $$de^{el} = \frac{ds}{2G}$$ $$G = G_o p_A \left(\frac{p}{p_A} \right)^{1/2} C_{SR} \left(\frac{1 + \frac{z_{cum}}{z_{max}}}{1 + \frac{z_{cum}}{z_{max}} C_{GD}} \right)$$ $$C_{SR} = \frac{1 - C_{SR,o} \cdot \left(\frac{M}{M^b} \right)^{m_{SR}}}{\left[1 - C_{SR,o} \cdot \left(\frac{M}{M^b} \right)^{m_{SR}} \right]_{initial}} \leq 1$$ $$C_{SR,o} = 0.5$$ $$m_{SR} = 4$$
Elastic volumetric strain increment $$d\varepsilon_v^{el} = \frac{dp}{K}$$ $$K = \frac{2(1+v)}{3(1-2v)} G$$	*Elastic volumetric strain increment* $$d\varepsilon_v^{el} = \frac{dp}{K}$$ $$K = \frac{2(1+v)}{3(1-2v)} G$$
Yield surface $$f = \left[(s - p\boldsymbol{\alpha}):(s - p\boldsymbol{\alpha}) \right]^{1/2} - \sqrt{2/3}\, pm = 0$$	*Yield surface* $$f = \left[(s - p\boldsymbol{\alpha}):(s - p\boldsymbol{\alpha}) \right]^{1/2} - \sqrt{1/2}\, pm = 0$$

Plastic deviatoric strain increment	*Plastic deviatoric strain increment*

Plastic deviatoric strain increment

$$de^{pl} = \langle L \rangle R'$$

$$R = Bn - C\left(n^2 - \frac{1}{3}I\right) + \frac{1}{3}DI$$

$$B = 1 + \frac{3}{2}\frac{1-c}{c}g(\theta,c)\cos(3\theta)$$

$$C = 3\sqrt{\frac{3}{2}\frac{1-c}{c}}\,g(\theta,c)$$

$$c = \frac{Q_{ext}}{Q_{compr}}$$

$$g(\theta,c) = \frac{2c}{(1+c)-(1-c)\cos(3\theta)}$$

$$M^b = M\cdot\exp(-n^b\xi_R)$$

$$\alpha_\theta^b = \sqrt{\frac{2}{3}}\left[g(\theta,c)M^b - m\right]n$$

$$K_p = \frac{2}{3}G\cdot h_o\cdot\frac{(\alpha_\theta^b - \alpha):n}{(\alpha - \alpha_{in}):n}$$

Plastic deviatoric strain increment

$$de^{pl} = \langle L \rangle R'$$

$$R = R' + \frac{1}{3}DI = n + \frac{1}{3}DI$$

$$M^b = M\cdot\exp(-n^b\xi_R)$$

$$M = 2\cdot\sin(\phi_{cv})$$

$$\alpha^b = \sqrt{\frac{1}{2}}\left[M^b - m\right]n$$

$$K_p = G\cdot h_o\,\frac{\left[(\alpha^b - \alpha):n\right]^{0.5}}{\left[\exp((\alpha-\alpha_{in}):n)-1\right]+C_{\gamma 1}}C_{rev}$$

$$\cdot\frac{C_{K\alpha}}{1+C_{K_p}\left(\frac{z_{peak}}{z_{max}}\right)\langle(\alpha^b-\alpha):n\rangle\sqrt{1-C_{zpk2}}}$$

$$C_{rev} = \frac{(\alpha-\alpha_{in}^{app}):n}{(\alpha-\alpha_{in}^{true}):n} \quad for \quad (\alpha-\alpha_{in}^p):n\leq 0$$

$$=1 \quad otherwise$$

$$C_{K\alpha} = 1 + \frac{C_{K\alpha f}}{1+\left(2.5\cdot\langle(\alpha-\alpha_{in}^{true}):n\rangle\right)^2}\cdot C_{pzp2}\cdot C_{zpk1}$$

$$C_{zpk1} = \frac{z_{peak}}{z_{cum}+\frac{z_{max}}{5}}$$

$$C_{zpk2} = \frac{z_{peak}}{z_{cum}+\frac{z_{max}}{100}}$$

	$C_{pzp2} = \dfrac{-\langle -(p_{zp} - p) \rangle}{-\langle -(p_{zp} - p) \rangle + p_{\min}}$ $C_{\gamma 1} = \dfrac{h_o}{200}$ $C_{Kp} = 2$
Plastic volumetric strain increment $d\varepsilon_v^{pl} = \langle L \rangle D$ $M^d = M \cdot \exp(n^d \xi_R)$ $\boldsymbol{\alpha}_\theta^d = \sqrt{2/3} \left[g(\theta, c) M^d - m \right] \boldsymbol{n}$ $D = A_d \cdot \left[(\boldsymbol{\alpha}_\theta^d - \boldsymbol{\alpha}) : \boldsymbol{n} \right]$ $A_d = A_o \left(1 + \langle \boldsymbol{z} : \boldsymbol{n} \rangle \right)$	**Plastic volumetric strain increment** $d\varepsilon_v^{pl} = \langle L \rangle D$ $M^d = M \cdot \exp(n^d \xi_R)$ $M^{dR} = \dfrac{M^d}{C_{rot1}}$ $C_{rot1} = 1 + \dfrac{2 \cdot \langle -\boldsymbol{z} : \boldsymbol{n} \rangle}{\sqrt{2} z_{\max}} \cdot (1 - C_{zin1}) \geq 1$ $C_{zin1} = \left\langle 1 - \exp\left(-2.0 \left| \dfrac{\boldsymbol{z}_{in} : \boldsymbol{n} - \boldsymbol{z} : \boldsymbol{n}}{z_{\max}} \right| \right) \right\rangle$ $\alpha^d = \dfrac{1}{\sqrt{2}} \cdot (M^d - m) \boldsymbol{n}$ $\alpha^{dR} = \dfrac{1}{\sqrt{2}} \cdot (M^{dR} - m) \boldsymbol{n}$ *If dilating (D<0):* $D_{non-rot} = A_d \cdot \left[(\alpha^d - \alpha) : \boldsymbol{n} \right]$ $D_{rot} = A_d \cdot \dfrac{\langle -\boldsymbol{z} : \boldsymbol{n} \rangle}{\sqrt{2} z_{\max}} \cdot \dfrac{(\alpha^{dR} - \alpha) : \boldsymbol{n}}{C_{DR}}$

$$if \ \ D_{non-rot} < D_{rot} \ \ \Rightarrow \ \ D = D_{non-rot}$$

$$else \ \ D = D_{non-rot} + \left(D_{rot} - D_{non-rot} \right) \cdot \frac{\left\langle M^b - M^{cur} \right\rangle}{\left\langle M^b - M^{cur} + 0.01 \right\rangle}$$

$$A_d = \frac{A_{do}\left(C_{zin2} \right)}{\left(\dfrac{z_{cum}^2}{z_{max}} \right) \left(1 - \dfrac{\left\langle -z : \boldsymbol{n} \right\rangle}{\sqrt{2} \cdot z_{peak}} \right)^3 \left(C_\varepsilon \right)^2 \left(C_{pzp} \right) \left(C_{p\min} \right) \left(C_{zin1} \right) + 1}$$

$$A_{do} = \frac{1}{0.4} \cdot \frac{\left[\sin^{-1}\left(\dfrac{M^b}{2} \right) - \sin^{-1}\left(\dfrac{M}{2} \right) \right]}{M^b - M^d}$$

$$C_{pzp} = \frac{1}{1 + \left(2.5 p \middle/ p_{zp} \right)^5}$$

$$C_{p\min} = \frac{1}{1 + \left(p_{\min} \middle/ p \right)^2}$$

$$C_{zin1} = \left\langle 1 - \exp\left(-2.0 \left| \frac{\boldsymbol{z}_{in} : \boldsymbol{n} - \boldsymbol{z} : \boldsymbol{n}}{z_{max}} \right| \right) \right\rangle$$

$$C_{zin2} = \frac{1 + C_{zin1} \dfrac{z_{cum} - z_{peak}}{3 z_{max}}}{1 + 3 C_{zin1} \dfrac{z_{cum} - z_{peak}}{3 z_{max}}}$$

43

If contracting (D≥ 0)

$$D = A_{dc} \cdot \left[\left(\boldsymbol{\alpha} - \boldsymbol{\alpha}_{in}^{app} \right) : \boldsymbol{n} + C_{in} \right]^2 \frac{\left(\boldsymbol{\alpha}^d - \boldsymbol{\alpha} \right) : \boldsymbol{n}}{\left(\boldsymbol{\alpha}^d - \boldsymbol{\alpha} \right) : \boldsymbol{n} + C_D} C_{p\min 2} \quad \leq 1.5 \cdot A_{do} \frac{\left(\boldsymbol{\alpha}^d - \boldsymbol{\alpha} \right) : \boldsymbol{n}}{\left(\boldsymbol{\alpha}^d - \boldsymbol{\alpha} \right) : \boldsymbol{n} + C_D}$$

$$A_{dc} = \frac{A_{do} \left(1 + \langle z : \boldsymbol{n} \rangle \right)}{h_p C_{dz}}$$

$$C_{in} = \frac{2 \langle z : \boldsymbol{n} \rangle}{\sqrt{2} z_{max}}$$

$$C_{dz} = \left(1 - C_{rot2} \cdot \frac{\sqrt{2} z_{peak}}{z_{max}} \right) \cdot \left(\frac{z_{max}}{z_{max} + C_{rot2} z_{cum}} \right) \geq \frac{1}{1 + \frac{z_{max}}{2}}$$

$$C_{rot2} = 1 - \frac{z_{peak}}{z_{cum} + \frac{z_{max}}{100}} \left(= 1 - C_{zpk2} \right)$$

$$C_D = 0.1$$

$$C_{p\min 2} = 0 \quad for \quad p \leq 2 p_{min}$$

$$C_{p\min 2} = 1 \quad for \quad p \geq 18 p_{min}$$

$$C_{p\min 2} = \frac{p - 2 p_{min}}{16 p_{min}} \quad otherwise$$

$$h_p = h_{po} \, exp\left(-0.7 + 7.0 \left(0.5 - \xi_R \right)^2 \right) \quad for \quad \xi_R \leq 0.5$$

$$h_p = h_{po} \, exp\left(-0.7 \right) \quad for \quad \xi_R > 0.5$$

Fabric-dilatancy tensor update $$d\mathbf{z} = -c_z \left\langle -d\varepsilon_v^{pl} \right\rangle (z_{max}\mathbf{n} + \mathbf{z})$$	**Fabric-dilatancy tensor update if** $\left(\boldsymbol{\alpha}^d - \boldsymbol{\alpha}\right):\mathbf{n} < 0$ $$d\mathbf{z} = -\frac{c_z}{1 + \left\langle \dfrac{z_{cum}}{2z_{max}} - 1 \right\rangle} \frac{\left\langle -d\varepsilon_v^{pl} \right\rangle}{D} (z_{max}\mathbf{n} + \mathbf{z})$$ $$d\mathbf{z}_{cum} = \left| d\mathbf{z} \right|$$
Stress increment $$L = \frac{2G\mathbf{n}:d\mathbf{e} - \mathbf{n}:\mathbf{r}Kd\varepsilon_v}{K_p + 2G\left(B - C\cdot tr\mathbf{n}^3\right) - KD\mathbf{n}:\mathbf{r}}$$ $$d\boldsymbol{\sigma} = 2Gd\mathbf{e} + Kd\varepsilon_v\mathbf{I}$$ $$- \langle L \rangle \left(2G\left[B\mathbf{n} - C\left(\mathbf{n}^2 - \frac{1}{3}\right)\mathbf{I} \right] + KD\mathbf{I} \right)$$	**Stress increment** $$L = \frac{2G\mathbf{n}:d\mathbf{e} - \mathbf{n}:\mathbf{r}Kd\varepsilon_v}{K_p + 2G - KD\mathbf{n}:\mathbf{r}}$$ $$d\boldsymbol{\sigma} = 2Gd\mathbf{e} + Kd\varepsilon_v\mathbf{I} - \langle L \rangle \left(2G\mathbf{n} + KD\mathbf{I} \right)$$
	Post-shaking reconsolidation $$G_{post-shaking} = F_{sed}G$$ $$K_{post-shaking} = F_{sed}K$$ $$F_{sed} = F_{sed,min} + \left(1 - F_{sed,min}\right)\left(\frac{p'}{20p'_{sed}}\right) \quad \leq \quad 1$$ $$p'_{sed} = p'_{sed_o}\left(\frac{z_{cum}}{z_{cum} + z_{max}}\right)\left\langle 1 - \frac{M^{cur}}{M^d} \right\rangle^{0.25}$$ $$F_{sed,min} = 0.04$$ $$p'_{sed_o} = -\frac{P_{atm}}{5}$$
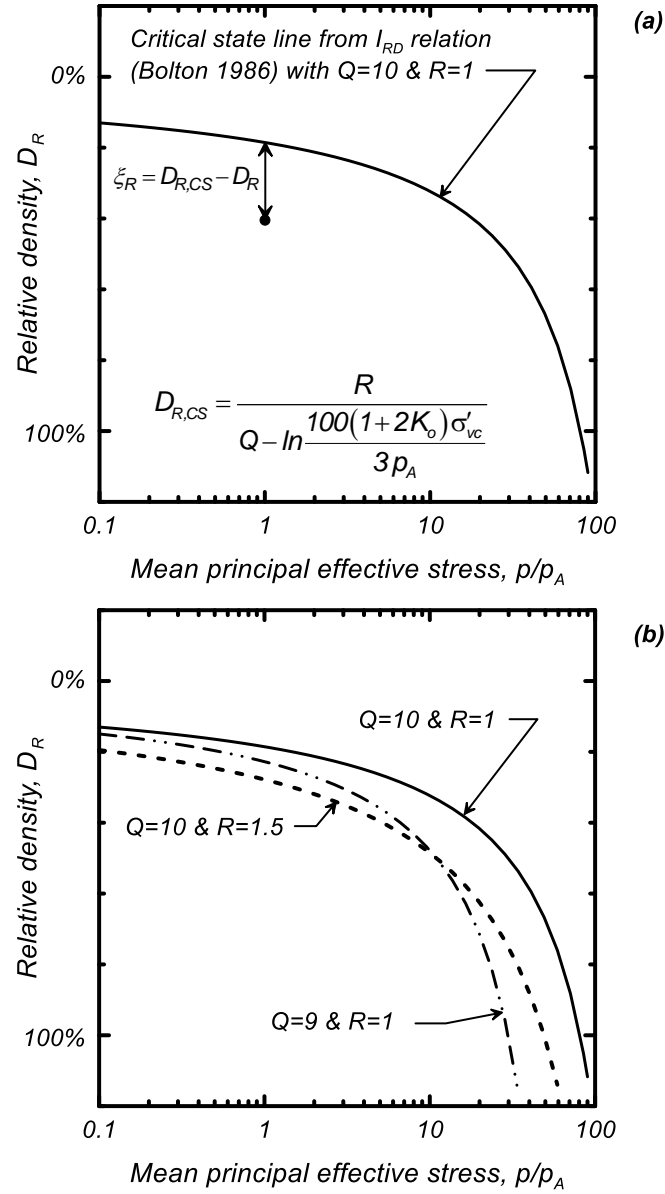
Figure 2.1. Definition of the relative state parameter index, ξ_R (Boulanger 2003a) and the effects of varying Q and R.
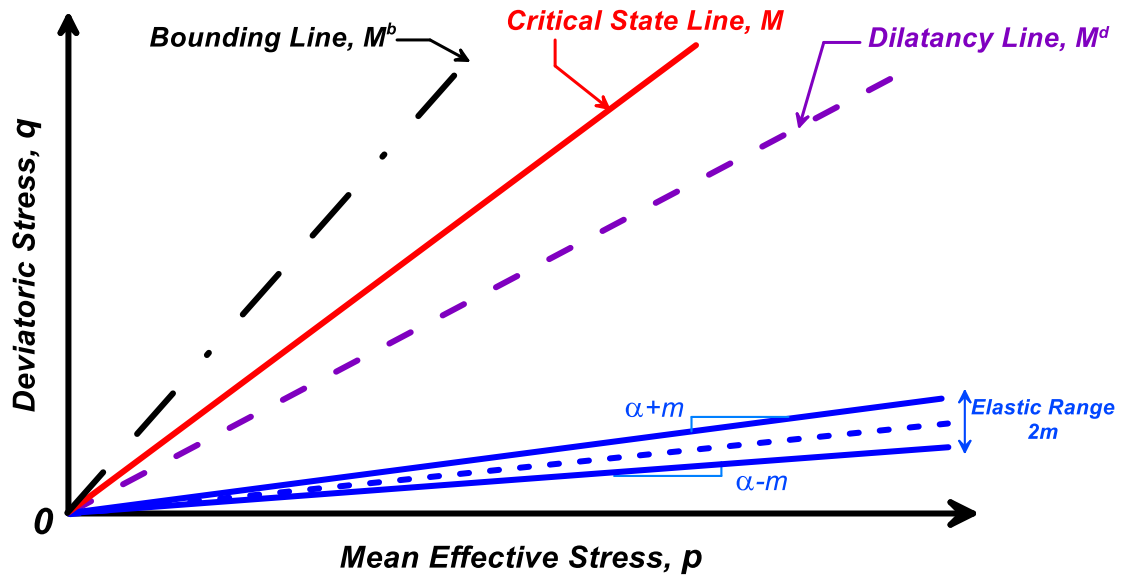
Figure 2.2. Schematic of yield, critical, dilatancy, and bounding lines in q-p space
(after Dafalias & Manzari 2004). Relative location of dilatancy and bounding lines corresponds to
dense-of-critical states of stress.
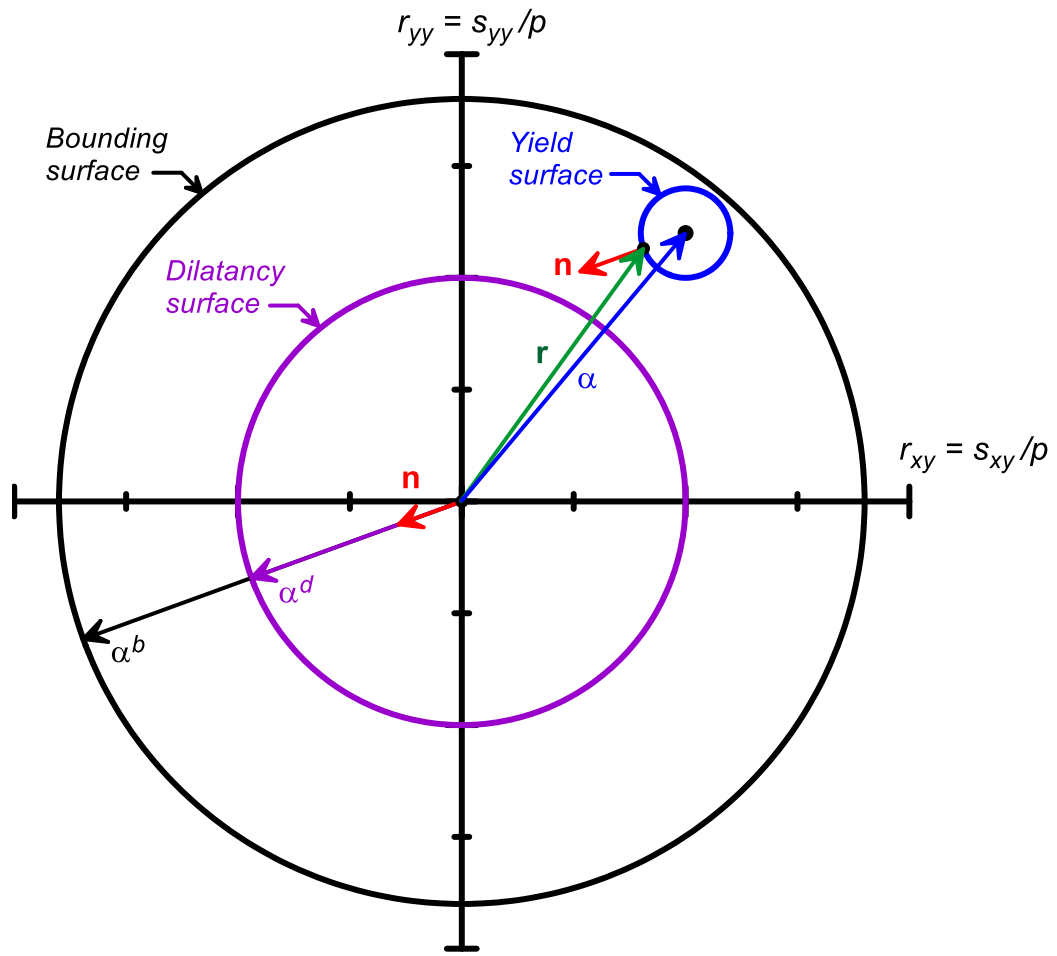
Figure 2.3. Schematic of the bounding, dilatancy, and yield surfaces on the r_{yy}-r_{xy} stress-ratio plane with the yield surface, normal tensor, dilatancy back-stress ratio, and bounding back-stress ratio. Relative locations of the surfaces differ from those of Figure 2.2.
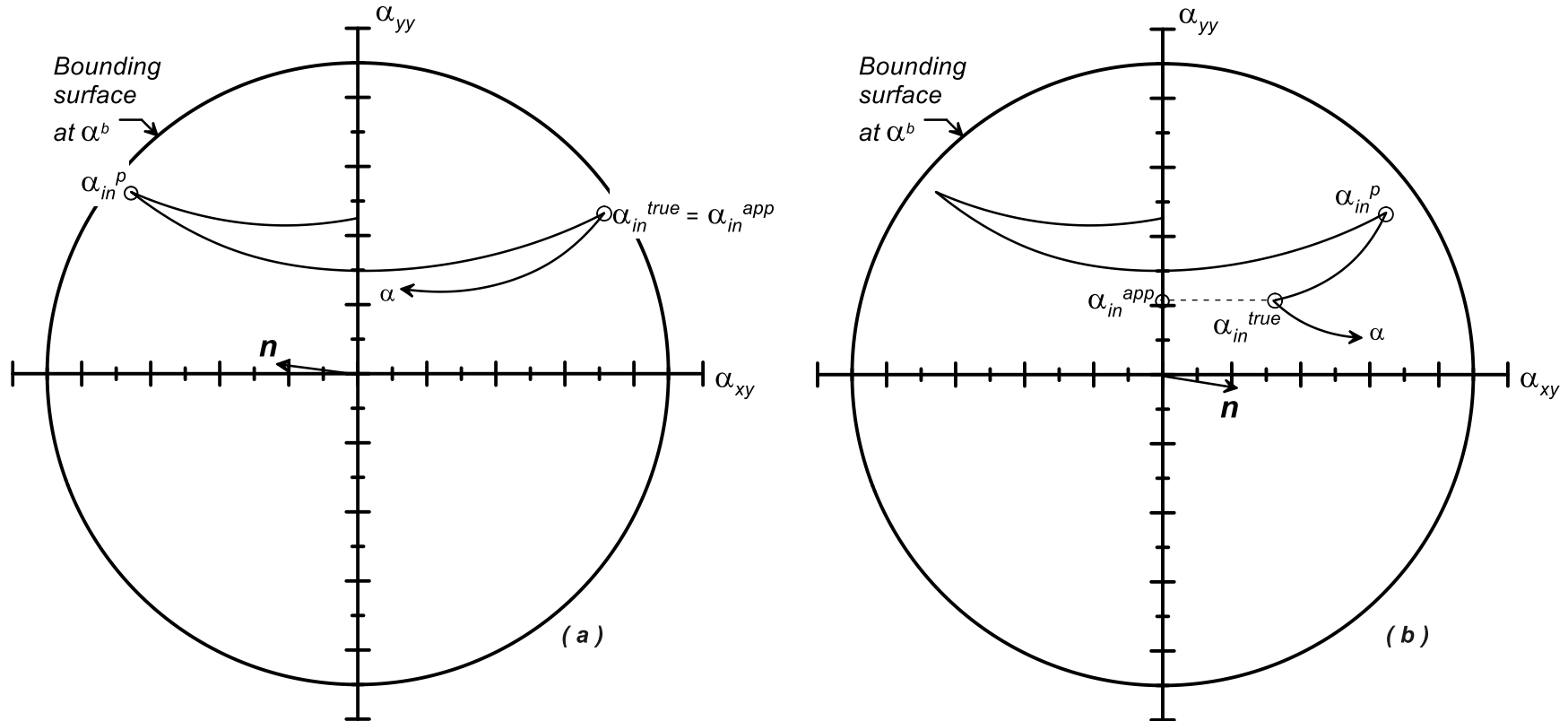
Figure 2.4. Schematic showing definitions of back-stress ratio tensors on the α_{yy}-α_{xy} plane for: (a) a loading history with reversals in the sign of the shear stress ratios, and (b) a loading history with a recent loading reversal that does not involve reversal of the sign of the shear stress ratios.
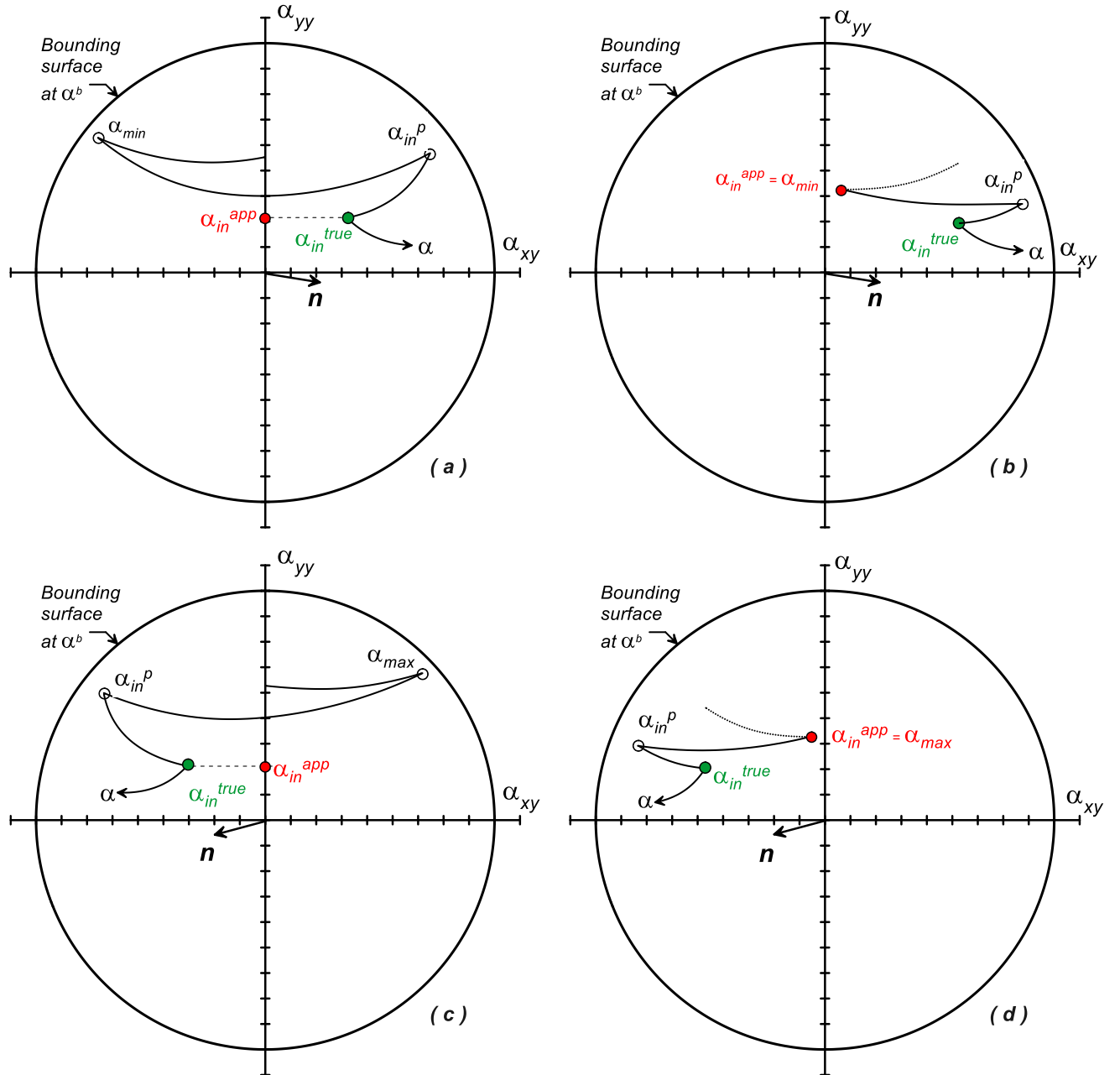
Figure 2.5. Example scenarios of back-stress ratio tracking: (a) positive loading direction with minimum value of back-stress ratio ($\boldsymbol{\alpha}_{min}$) being less than zero such that $\boldsymbol{\alpha}_{in}^{app} = \boldsymbol{\alpha}_{in}^{true}$, (b) positive loading direction with minimum value of back-stress ratio ($\boldsymbol{\alpha}_{min}$) being greater than zero such that $\boldsymbol{\alpha}_{in}^{app} = \boldsymbol{\alpha}_{min}$, (c) negative loading direction with maximum value of back-stress ratio ($\boldsymbol{\alpha}_{max}$) being greater than zero such that $\boldsymbol{\alpha}_{in}^{app} = \boldsymbol{\alpha}_{in}^{true}$, (d) negative loading direction with minimum value of back-stress ratio ($\boldsymbol{\alpha}_{max}$) being less than zero such that $\boldsymbol{\alpha}_{in}^{app} = \boldsymbol{\alpha}_{max}$.
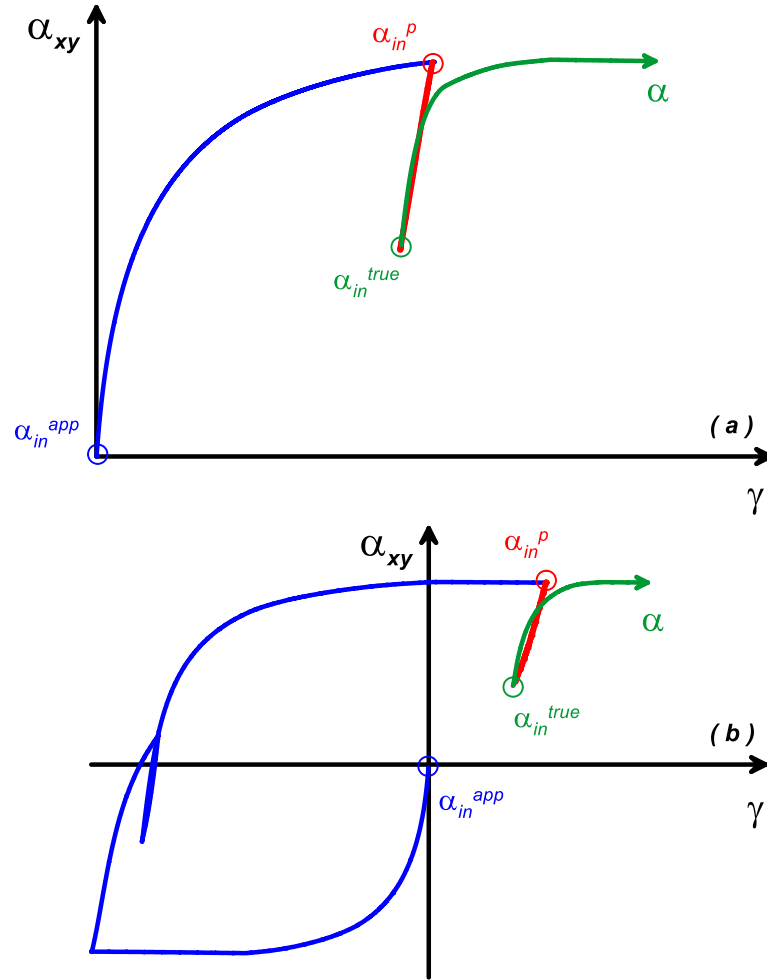
Figure 2.6. Drained DSS simulations showing α_{xy} versus γ with the points corresponding to the current back-stress ratio $\boldsymbol{\alpha}$, the apparent initial back-stress ratio $\boldsymbol{\alpha}_{in}^{app}$, the true initial back-stress ratio $\boldsymbol{\alpha}_{in}^{true}$, and the previous initial back-stress ratio $\boldsymbol{\alpha}_{in}^{p}$ for: (a) monotonic shearing with one intermediate unload-reload cycle, and (b) a more general sequence of cyclic loading.
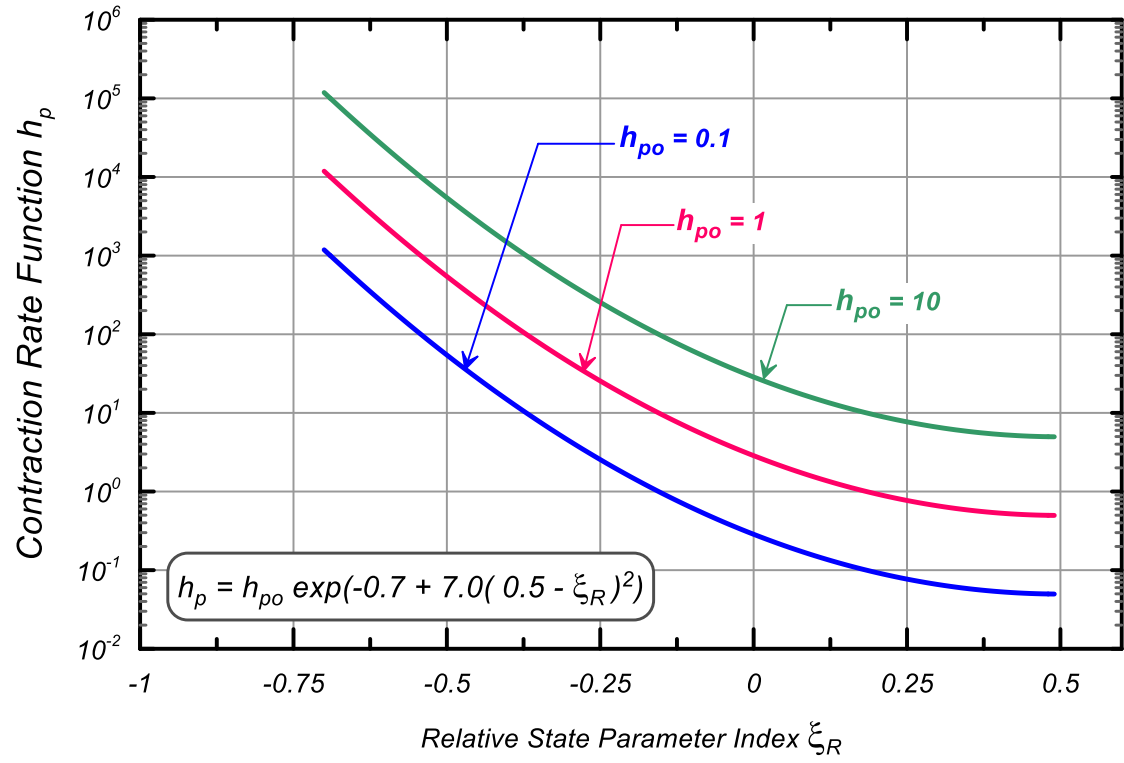
Figure 2.7. Variation of contraction rate function h_p with relative state parameter index ξ_R and the contraction rate parameter h_{po}.
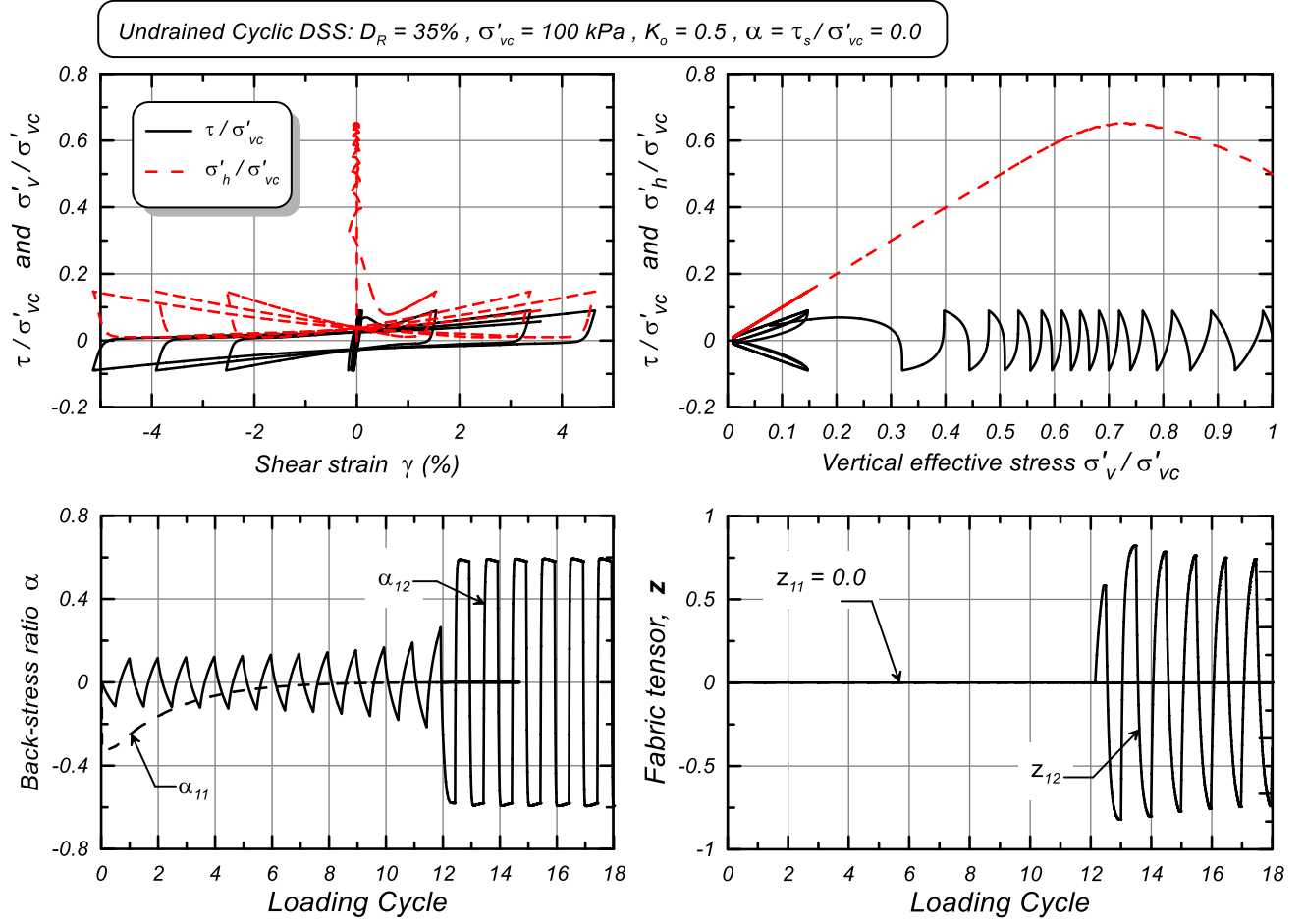
Figure 2.8. Undrained cyclic DSS loading response for $D_R = 35\%$ with an initial static shear stress ratio of $\alpha=0.0$, showing the variation in stresses, stress ratios, and fabric tensor terms.
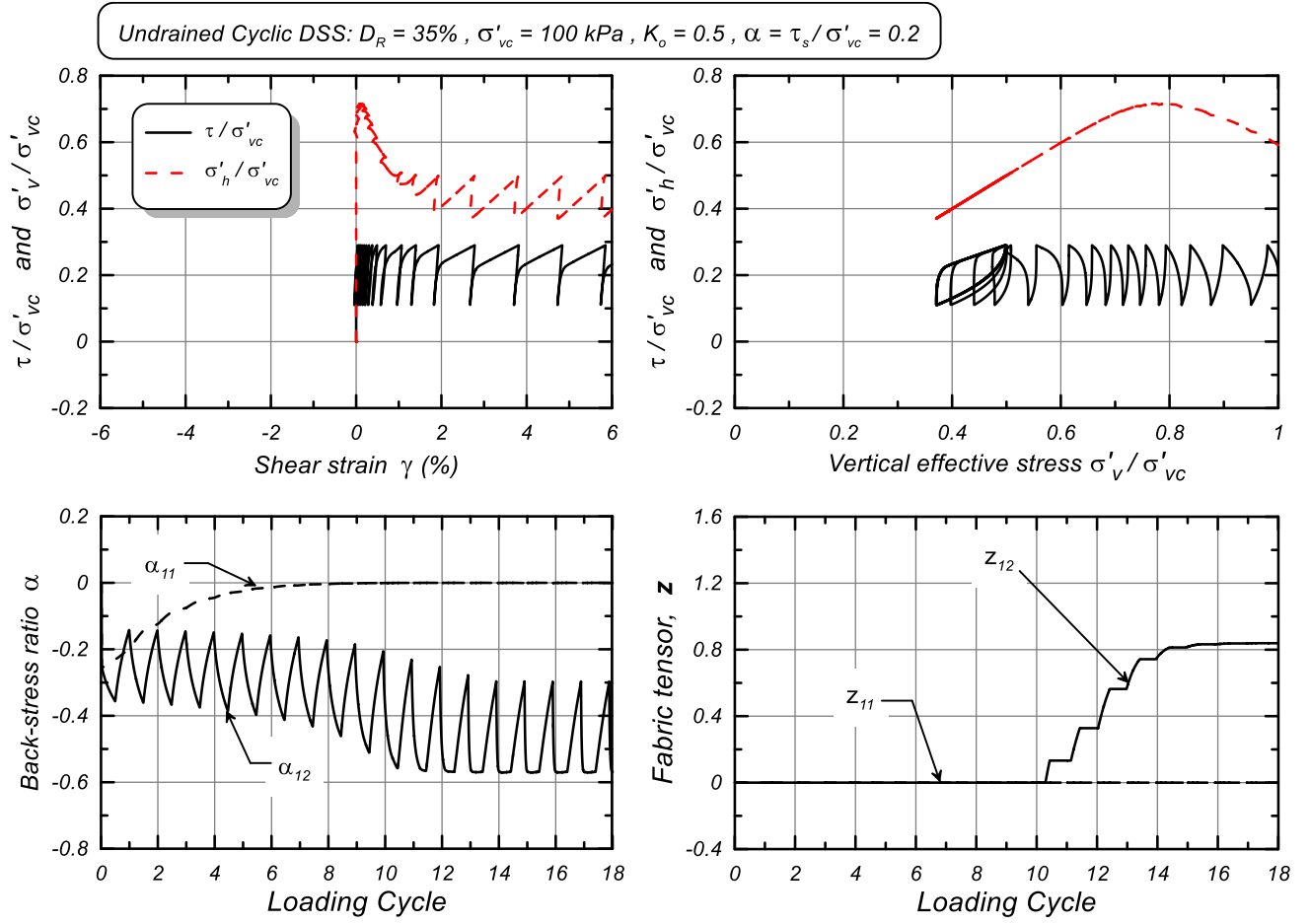
Figure 2.9. Undrained cyclic DSS loading response for D$_R$ = 35% with an initial static shear stress ratio of α=0.20, showing the variation in stresses, stress ratios, and fabric tensor terms.
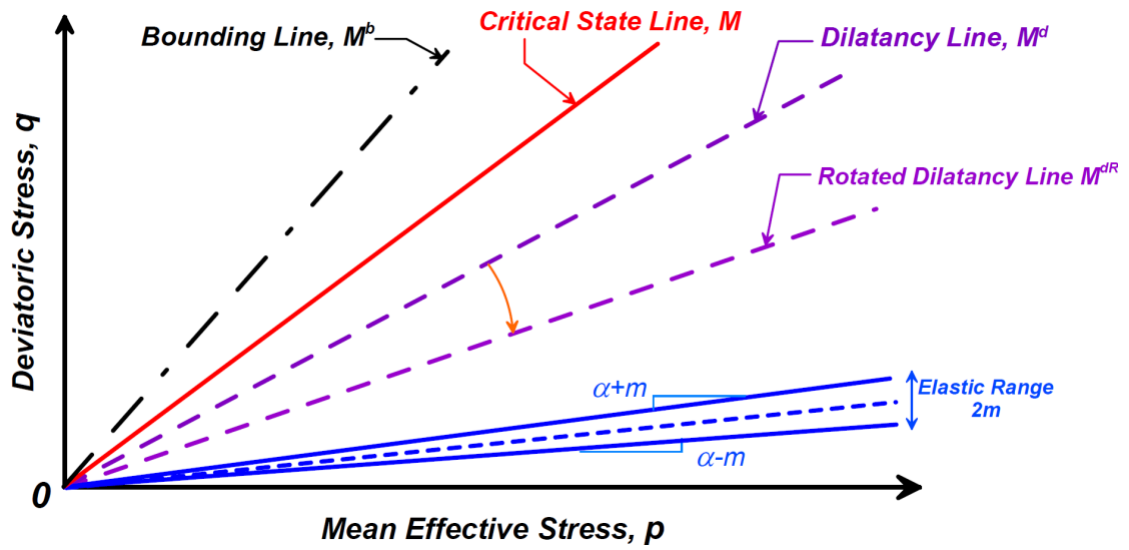
Figure 2.10. Schematic of the rotated dilatancy line added to PM4Sand Version 3, along with the yield, critical, dilatancy, and bounding lines in q-p space. Relative location of dilatancy and bounding lines corresponds to dense-of-critical states of stress.
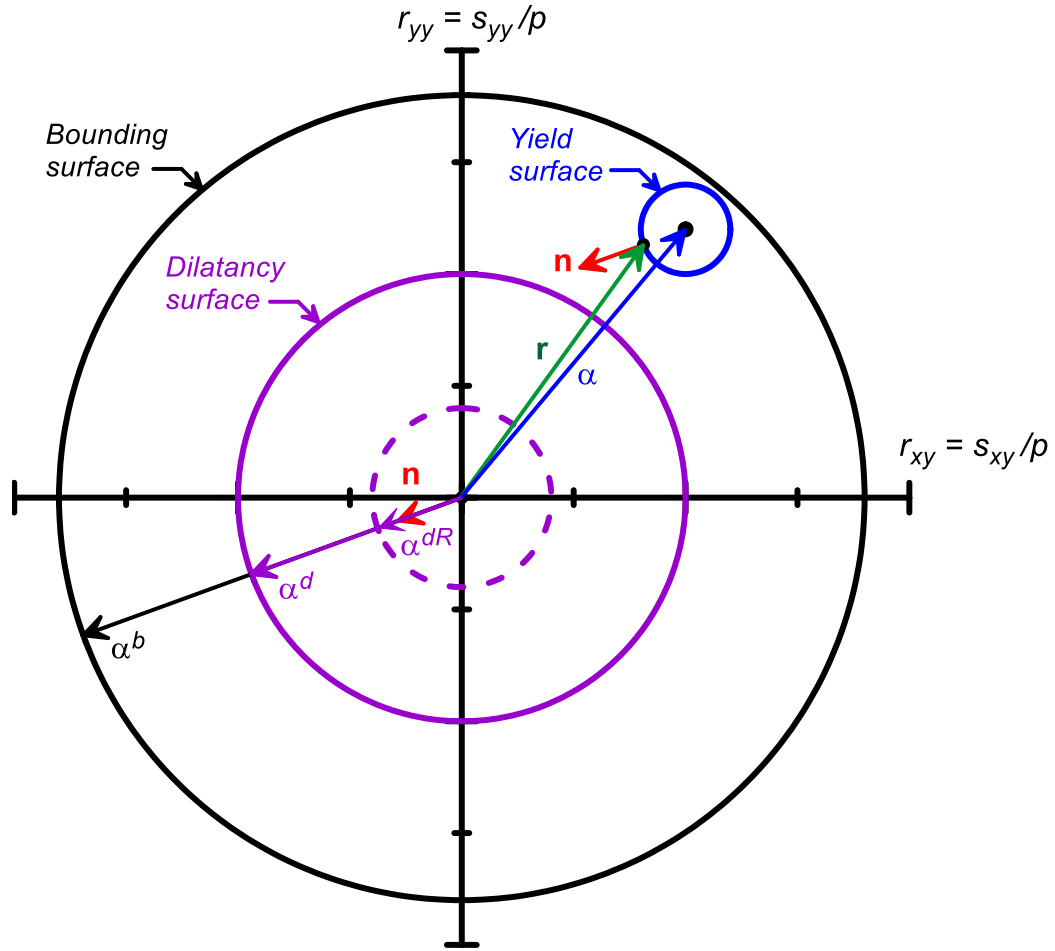
Figure 2.11. Schematic of the rotated dilatancy line, along with the bounding, dilatancy, and yield surfaces on the r_{yy}-r_{xy} stress-ratio plane with the yield surface, normal tensor, dilatancy back-stress ratio, and bounding back-stress ratio. Relative locations of the surfaces differ from those of Figure 2.10.
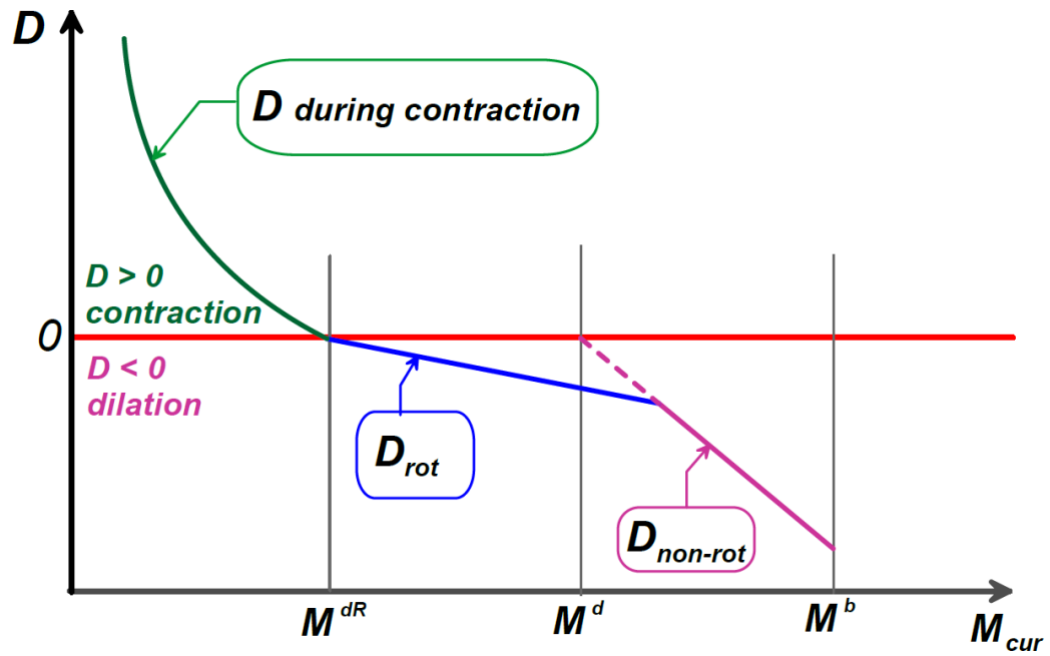
Figure 2.12. Schematic of the dilatancy D calculation based on the stress state with regards to the rotated dilatancy (M^{dR}), dilatancy (M^d) and bounding (M^b) surfaces during a half-cycle of loading that goes from contraction to dilation.

3. MODEL IMPLEMENTATION

The model has been implemented as a user defined material (udm) for use with the commercial finite difference program, FLAC 8.1 (Itasca 2019). This section includes a brief description of the mixed discretization scheme used in FLAC, the numerical implementation scheme used for PM4Sand, some additional comments on alternative implementation schemes, and information regarding the dynamic link library (DLL) for PM4Sand.

3.1 Aspects of FLAC's numerical approach

Explicit integration

FLAC is an explicit finite difference program which uses time steps equal to or smaller than the minimum time required for waves to travel between any pair of nodes. This approach ensures that physical information does not propagate faster than numerical information. FLAC computes a default time step based on the properties of the model (e.g., element size, material stiffness, permeability, damping). Users may specify a time step that is smaller than the default value.

Obtaining numerically convergent solutions to nonlinear problems using FLAC requires that:

1) integration of the constitutive models be convergent, and
2) the explicit global solution is convergent.

The default time step computed by FLAC does not necessarily ensure a numerically convergent solution, especially for FLAC models that are subjected to very high loading rates. Convergence of the constitutive model's integration depends more strongly on the strain increment size, which is dependent on both the loading rate and time step size. Convergence of the explicit global solution depends more strongly on the sizes of the stress increments generated in the materials, which again are only indirectly controlled by the default time step size. For this reason, the user needs to evaluate the sensitivity of the solution to the time step size and not automatically assume that the default time step size ensures a convergent solution.

Mixed discretization scheme

FLAC uses a mixed discretization technique in which each quadrilateral zone (analogous to an element) is subdivided internally by its diagonals into two overlaid sets of constant-strain triangles. The term "mixed" stems from the fact that different discretizations are used for the isotropic and deviatoric parts of the strain and stress tensor (Marti and Cundall 1982). Isotropic stress and strain components are taken to be constant over the whole quadrilateral zone, while the deviatoric components are treated separately for each triangular sub-zone. Essentially, the shear strains are computed and maintained for each individual triangle, while the volumetric strains are computed for each quadrilateral as a weighted average of the volumetric strains within the juxtaposed pairs of triangles. Hour-glass modes are resisted by shear stresses generated in the triangles and the scheme accurately predicts plastic collapse loads because constant volume deformations are possible within the quadrilaterals. Note that discretization using triangles or four-node quadrilaterals alone would result in meshes that are over-constrained (too stiff) and which would tend to over-predict plastic collapse loads. Since each quadrilateral can be

divided by two possible diagonals, a symmetric response of this discretization can only be obtained by running two complete meshes in parallel, each representing one half of the overall stiffness. At the end, the procedure reduces the number of constraints on plastic flow and, at the same time, reduces unwanted hour-glassing by ensuring that hourglass modes produce non-zero stresses.

The implementation of a complex constitutive model in FLAC requires special attention to the way stresses and strains are handled under FLAC's mixed discretization scheme. During each time step, FLAC calls the constitutive model once per triangular subzone (four times per zone). The isotropic components of the stress outputs from the four subzones are then averaged internally by FLAC according to the Mixed Discretization scheme. A consequence of this averaging of stresses is that the final stress state for any subzone is unlikely to satisfy the consistency condition of elasto-plastic models, meaning that the newly calculated stress states will not necessarily lie on the yield surface. Andrianopoulos (2006) addressed this problem by adopting a vanished elastic region in their elasto-plastic model.

3.2. Implementation of PM4Sand in FLAC

The implementation scheme for PM4Sand and how it relates to the challenges posed by FLAC's mixed discretization scheme (Section 3.1) are described here. Recall that each zone (consisting of four subzones) will start off at the beginning of each time step with a stress state and will be loaded by a strain increment whose volumetric components are the same in all four subzones while their deviatoric components are different (due to the mixed discretization scheme). The constitutive model will be called once per subzone (four times per zone) to obtain stresses from strains according to the following equation where C_{ijkl} denotes the constitutive law:

$$\sigma_{ij}^{(i+1)} = \sigma_{ij}^{(i)} + d\sigma_{ij}^{(dt)} = \sigma_{ij}^{(i)} + C_{ijkl}d\varepsilon_{ij}^{(dt)} \tag{93}$$

At the end of the step, each subzone will have its own stress state, which will be handled by FLAC independent of the constitutive model, and its own internal parameters, which FLAC will be unaware of. The subzones can therefore all have different stress states at the beginning of the next loading increment, and as such would need to maintain their own sets of internal parameters.

The current implementation scheme for PM4Sand is illustrated in Figure 3.1 and described by the pseudo-code listed in Table 3.1. At the end of each time step, the stress and internal variables are averaged over the four subzones. A drift correction is applied to ensure that the averaged stresses and internal variables satisfy the consistency condition; the correction involves projecting the back-stress ratio in the direction of the zone-averaged stress ratio. Another correction is applied if the zone-averaged stress ratio lies outside the bounding surface; the correction involves projecting the zone averaged stress ratio back along a normal to the bounding surface. The zone-averaged stresses are then used to compute a new dilatancy D and plastic modulus K_p that are consistent with the average response of the zone over this step. These values for D and K_p are then used by all four subzones in the next time step (i.e., the values of D and K_p lag one step behind the time step for which they were determined); note that this approach is used by other elasto-plastic models available in FLAC. Consequently, the four subzones will use a common D and K_p during each time step. Most other internal parameters are also computed and retained at the zone level, as described by the pseudo-code in Table 3.1.

Two other implementation schemes for PM4Sand were explored for comparison purposes and found to have problems. The first of these alternative implementations was that used in Version 1 of PM4Sand. In this implementation, each subzone had its own D and K_p and developed its own internal variables (e.g., fabric, back-stress ratios, history terms) for each loading increment or step. At the end of the step, the stress and internal variables were averaged at the zone level and the drift and bounding surface corrections were applied. The four subzones therefore started each loading step with a common set of stresses and internal variables, but each could have greatly differing values for D and K_p depending on the loading direction imposed on each subzone. In highly nonlinear loading steps, it was possible for one or two of the overlapping subzones to be strongly contractive (e.g., perhaps because of a reversal in loading direction) while the other subzones were strongly dilative, such that the incremental changes in stresses between the four subzones had competing effects on the zone's average behavior. This implementation was found to sometimes lead to unusual deformation modes in zones that were connected to piles by FLAC's interface springs. The unusual deformation modes are believed to be due to strong differences in loading directions and conditions between the subzones of zones being loaded by interface springs. This problem was effectively eliminated by the current implementation described in Table 3.1. The second of these alternative implementations increased the independence of the subzones, just to explore how it would affect behavior. In this implementation, each subzone (triangle) retained its own memory and history of stresses and internal parameters. This approach led to nonsensical results between the overlapping triangular subzones, especially when the loading conditions were highly nonlinear. For example, the external stresses sometimes could be carried by only two of the overlapping triangles (each having twice the correct stresses) while the stresses in the other two overlapping triangles went to zero. The experiences with these two alternative implementation schemes illustrate how FLAC's mixed discretization scheme requires special considerations when implementing highly nonlinear constitutive models.

The current implementation also includes a scheme to reduce hour-glassing modes which developed in liquefied zones in some cases because the four subzones no longer have independent states of stress. The four subzones have, in parallel to the PM4Sand constitutive model, an elastic-plastic resistance to shear stresses which acts independently in each of the subzones. The properties of this parallel elastic-plastic model are set at the instance when PM4Sand is initialized; the elastic moduli of the parallel elastic-plastic model are set equal to 0.01 times those for PM4Sand, and its plastic shear strength (c_{hg}) is set as the product of a strength ratio (cr_{hg}) times the mean effective stress in the zone. If the user specifies values for both c_{hg} and cr_{hg}, then c_{hg} is taken as the greater of the specified c_{hg} value and the value computed using the specified cr_{hg}. The default value for cr_{hg} is 0.005. The parallel elastic-plastic model only responds to deviatoric strains (producing shear stresses) and not to volumetric strains (producing no mean stress). This nominal amount of independent shearing resistance in the subzones was found to adequately control hour-glassing modes for the range of problems examined to date.

Implementation of PM4Sand uses explicit integration and thus the user should routinely check that the solutions are not sensitive to time step size. The addition of substepping could improve the constitutive model's integration but would not eliminate the need to evaluate the effect of time step size on the global solution. In the developers' experiences, the default time steps of FLAC in dynamic analyses of liquefaction problems have been small enough to ensure that numerical solutions are not significantly affected by time step size, and thus the additional computational cost of including substepping at the constitutive level was not considered necessary. Examples of the effects of time step size are presented in Section 3.3.

Numerical stability of the implemented model has been evaluated for a wide range of simulations of both element responses and system responses using the default range of parameters which are also summarized in the next section. Numerical stability problems may, however, develop when using input parameters which fall outside the ranges explored during model development, calibration, and implementation. Some initial bounds have therefore been placed on certain parameters whenever parametric analyses identified the potential for such problems; e.g., the minimum value of mean stress is limited to 0.5 kPa or 0.005 times the initial consolidation stress; the relative density was limited to values less than 1.2. The user must be aware that other limits may be identified as additional analyses explore a broader range of the possible input parameters.

3.3 Effect of time step size on element responses

Numerical convergence of the current implementation of PM4Sand was evaluated by running numerous problems using a range of dynamic time steps (dydt), beginning with the default (maximum) time step computed by FLAC and then trying smaller and smaller values. These comparisons have shown that the solutions are not sensitive to the time step size for the range of problems and loading rates examined. The user must always check the sensitivity of boundary value problems to the time step size, however, as the accuracy of the explicit integration is strongly dependent on the size of the strain increments which are only partly controlled by the time step size.

For example, the effect of time step size (or strain increment size) on integration of the PM4Sand model is shown in Figure 3.3a for a single element simulation of a cyclic drained DSS test for sand at $D_R = 55\%$ at $\sigma'_{vo} = 100$kPa. The element was subjected to two cycles of strain-controlled loading with a single-amplitude shear strain of 1%. The strain rate was constant, with each cycle having a total duration of 1 sec (i.e., average loading frequency was 1 Hz). The default time step was 1.038e-4 s and the strain rate was 4 %/s which gives a step size of $\Delta\gamma = 4.15$e-6 %/step. To evaluate different $\Delta\gamma$'s, the time step was reduced by factors of ½, ¼, and 1/8. The simulated stress-strain responses showed minimal differences, indicating that the integration was sufficiently accurate for practical purposes.

A second example of the effect of time step size is shown in Figure 3.3b for a stress-controlled cyclic undrained DSS test for sand at $D_R = 55\%$ at $\sigma'_{vo} = 100$kPa. The default time step was 3.604e-5 s and the strain rate was again 4 %/s which gives a step size of $\Delta\gamma = 1.44$e-6 %/step. The default time step is smaller for the undrained element test because of the higher wave speed in the pore water. To evaluate different $\Delta\gamma$, the time step was again reduced by factors of ½, ¼, and 1/8. The simulated stress-strain responses again showed minimal differences, indicating that the integration was sufficiently accurate for practical purposes.

Figure 3.3a and b presents the same examples as Figure 3.2a and b but for a very high strain rate of 12%/s. The corresponding step sizes for the drained (a) and undrained (b) cases are 12.45e-6%/step and 4.32e-6 %/step, respectively. To evaluate different $\Delta\gamma$'s, the time step was again reduced by factors of 1/2, 1/4 and 1/8. The simulated stress-strain responses for the drained case showed minimal differences, whereas the undrained case showed some slight differences. The differences for the undrained case are attributed to the very high strain rate of 12%/sec, which was only used to examine the limits of behaviors.

Note that comparisons of solutions at different step sizes $\Delta\gamma$ generally cannot be made by just varying the strain rate or cyclic loading frequency. FLAC is always solving the dynamic equation of equilibrium so changing the strain rate by changing any loading rate parameter also changes the dynamic excitation for the system, which can cause a change in the dynamic response of the element. In that case, any changes in the stress-strain response caused by changes in loading rate parameters may be a realistic simulation result that reflects the change in the dynamic excitation of the element.

3.4 Effect of time step size on system responses

The effect of time step size on the solution of full boundary value problems can similarly be examined by repeating simulations with successively smaller dynamic time step sizes. As an example, the effect of time step size on the seismic response of an embankment dam with PM4Sand used for the shells [$(N_1)_{60cs} = 25$] and foundation alluvium [$(N_1)_{60cs} = 15$] is illustrated in Figure 3.4. Time histories of crest settlement and horizontal displacements at points on the upstream and downstream faces are shown for the default time step size and for time step sizes that are ½ and ¼ the default size. The differences in the displacements at these three points are small enough to be virtually indistinguishable in the figure. The effect of time step size has been observed to be more significant in some other boundary value problem simulations (e.g., 5% differences), but they are generally small enough for practical applications.

The sensitivity of simulation results to the dynamic time step size should always be evaluated as part of the sensitivity studies. As previously discussed in Section 3.1, the effects of changing time step size may result from a combination of the effects on the constitutive model integration and the explicit global solution. Implementation of substepping in the constitutive model may reduce its effect, but will not remove the need to check the global solution's sensitivity to the step size. Since the sensitivity to step size should always be checked, the additional computational costs of including substepping at the constitutive level was not considered warranted at this time.

3.5 DLL module

The PM4Sand model was coded in C++ and compiled as a User Defined Model (UDM) dynamic link library (DLL) in Microsoft Visual Studio 2015 for FLAC 8.1 and in Microsoft Visual Studio 2022 for FLAC2D 9.00. The steps required for using a DLL are described in the respective FLAC/FLAC2D manuals.

Automatic loading of the DLL file in FLAC8.1

(1) Load the DLL file in the /Exe64/plugins/models subdirectory of the folder where FLAC has been installed.

(2) Open the FLAC 8.1 executable file or the FLAC graphical user interface. If the DLL is properly located, then the model should be automatically loaded. In order to verify that it has been loaded, the user can type "`print model`" in the console. If the model has been loaded then it should appear as "`pm4sand`" under the list of "Currently loaded CPP models".

(3) Before constitutive model plug-ins can be assigned to zones, the model must be configured for their use by giving the **config cppudm** command. Otherwise, the user will get a "model will not cycle" error message.

Automatic loading of the DLL file in FLAC2D 9.00

(1) Load the DLL file in the /Exe64/plugins/cmodels subdirectory of the folder where FLAC2D has been installed.

(2) Open the FLAC2D 9.00 executable file or the FLAC2D graphical user interface. If the DLL is properly located, then the model should be automatically loaded and the console will indicate "`flac2d>program load cmodel "plugins/cmodel/cmodelPM4Sand2D009.dll --- cmodel plugin pm4sand2d loaded.`". In order to also verify that it has been loaded, the user can type "`zone cmodel list`" in the console. If the model has been loaded then it should appear as "`pm4sand2d`" under the list of "Currently loaded CPP models".

(3) Before constitutive model plug-ins can be assigned to zones, the model must be configured for their use by giving the **model configure plugins** command. Otherwise, the user will get a "model will not cycle" error message.

In order to assign the model to the preferred zones the following command should be given in FLAC8.1:

```
model pm4sand <...>
```

or in FLAC2D 9.00:

```
zone cmodel assign pm4sand2d range <...>
```

3.6 Additional notes on use in boundary value problem simulations

FLAC includes both "static" and "dynamic" solution procedures. PM4Sand has been extensively validated for use with the dynamic procedure. The use of PM4Sand with FLAC's static solution procedure requires special attention to the loading and solution procedures. The static solution procedure uses extremely high damping values which can carry significant shear and normal stresses, which can cause problems with the response of a highly nonlinear, stress-dependent material. For example, if the user imposes a large strain rate (e.g., high rate of loading on a foundation) in a problem involving drained loading of a contractive soil with the static solution procedure, the drained volumetric contraction of the soil can result in normal stresses being transferred to the damping component which causes an artificial reduction in normal effective stress in the soil. For this reason, the use of PM4Sand with FLAC's static solution procedure requires a higher degree of scrutiny and evaluation to ensure that such problems do not develop.

A nominal amount of Rayleigh damping should be included with PM4Sand zones to control numerical noise during dynamic solutions. A damping ratio of 0.005 has been found sufficient for most applications.

63

Zones at the ground surface, particularly within slopes and above the water table, are susceptible to developing large deformations at strong shaking levels (i.e., when the frictional shear resistance is exceeded). Excessive distortion of surface zones can lead to premature stoppage of a simulation, particularly for soils that liquefy or cyclically soften. Some analysts will use Mohr Coulomb materials in lieu of complex sand models for surface zones, for which they can then include a nominal amount of cohesion to reduce the potential for surficial shear failures. In the current version of PM4Sand, a similar effect can be achieved by increasing the nominal shear resistance c_{hg} above the default value used to control hour-glassing in liquefied zones.

Loading conditions that cause a progressive increase in the mean effective stresses in PM4Sand, or any other pressure-dependent material, require special consideration during the solution process. The elastic moduli will increase with increasing mean effective stress, such that the time step required for a stable solution will decrease as the loading progresses. FLAC only determines the required time step at certain instances, like when the step or solve commands are executed. For this reason, the loading should be applied in small increments with the solve command periodically repeated so that the required time step is updated as appropriate during the applied loading.

Initial stresses in a boundary value problem are sometimes established using simpler constitutive models, like a Mohr Coulomb or elastic model, prior to switching the materials to a more complex model like PM4Sand. Problems can develop if the initial states of stress fall outside the greater of the bounding and dilatancy surface lines for the PM4Sand model. This can happen in zones where the initial state of stress was computed for a Mohr Coulomb material with a nonzero cohesion or for an elastic material. For this reason, it is helpful to first ensure that the initial states of stress in all zones correspond to a stress ratio that is less than some reasonable limit prior to switching the material model to PM4Sand.

The ability to use the DLL with FLAC's "free-field" lateral boundary conditions option or compliant base option has not been configured at this time. Thus, the user should not have PM4Sand in the outer column of elements against which the free-field lateral boundary condition will be applied. Instead, the outer columns can be replaced with elastic materials having a secant modulus compatible with the adjacent PM4Sand zones.

Table 3.1: Simplified pseudo-code of PM4Sand (Version 3.3)

Operations within one subzone:

1. Initialize the model parameters; this only happens when the model is first assigned or when FirstCall is set to zero at some point during the analysis. For detailed information on what parameters are initialized (or reset) see Table 3.2.
2. Obtain the strain increment from FLAC $d\boldsymbol{\varepsilon}$.
3. Decompose the strain increment into volumetric and deviatoric components, $d\varepsilon_p$ and $d\boldsymbol{e}_s$.
4. Calculate the trial elastic stress increment and trial elastic stress:

$$\boldsymbol{\sigma}_{tr} = \boldsymbol{\sigma}_0 + d\boldsymbol{\sigma}_{tr} = \boldsymbol{\sigma}_0 + 2Gd\boldsymbol{e} + Kd\varepsilon_v\boldsymbol{I}$$

5. Calculate the trial stress ratio $\boldsymbol{r}_{tr}$ the distance from the yield surface $dist$, the unit normal to the yield surface $\boldsymbol{n}$ and the inner product of the change in back-stress ratio tensor with unit normal vector $daxn$.

$$\boldsymbol{r}_{tr} = \frac{\boldsymbol{\sigma}_{tr} - p_{tr}\boldsymbol{I}}{p_{tr}}$$

$$dist = \sqrt{(\boldsymbol{r}_{tr} - \boldsymbol{\alpha}_0):(\boldsymbol{r}_{tr} - \boldsymbol{\alpha}_0)}$$

$$\boldsymbol{n} = \frac{(\boldsymbol{r}_{tr} - \boldsymbol{\alpha}_0)}{dist}$$

$$daxn = (\boldsymbol{\alpha}_0 - \boldsymbol{\alpha}_{in}):\boldsymbol{n}$$

6. Check for yield:
   a. If elastic then commit the trial stresses. Go to step 8.

   $$dist < \frac{1}{\sqrt{2}}m$$

   $$\boldsymbol{\sigma}_0 = \boldsymbol{\sigma}_{tr}$$

   b. If inelastic:
      i. Calculate loading index L:

      $$L = \frac{2G\boldsymbol{n}:d\boldsymbol{e} - \boldsymbol{n}:\boldsymbol{r}Kd\varepsilon_v}{K_p + 2G - KD\boldsymbol{n}:\boldsymbol{r}}$$

      ii. Calculate trial stress increment and trial stress:

      $$\boldsymbol{\sigma}_{tr} = \boldsymbol{\sigma}_0 + d\boldsymbol{\sigma}_{tr} = \boldsymbol{\sigma}_0 + 2Gd\boldsymbol{\varepsilon}_s + Kd\varepsilon_p\boldsymbol{I} - L\{2G\boldsymbol{n} + KD\boldsymbol{I}\}$$

      iii. Apply penalties to stress ratios and back-stress ratios to meet the consistency condition and to remain within the greater of the bounding and dilatancy surfaces.
      iv. Calculate image back-stress ratios and inner products:

      $$\boldsymbol{\alpha}^b = \sqrt{\tfrac{1}{2}}\left[M^b - m\right]\boldsymbol{n}$$

      $$\boldsymbol{\alpha}^d = \sqrt{\tfrac{1}{2}}\left[M^d - m\right]\boldsymbol{n}$$

      $$\boldsymbol{\alpha}^{dR} = \sqrt{\tfrac{1}{2}}\left[M^{dR} - m\right]\boldsymbol{n}$$

      v. Commit the trial stresses (back-stress ratios, stress ratio, mean stress, stress)
7. Return all stress tensor components to FLAC (at this point FLAC takes over and will average them according to the mixed discretization scheme)

Operations referring to the whole zone:

8. After the calculation has completed the 4th subzone, the following additional calculations are performed for the overall zone. Recall the following parameters for all 4 subzones and compute area-weighted average values for:
   - Volumetric strain $d\bar{\varepsilon}_p$
   - Strain increment $d\bar{\varepsilon}$

- Mean stress $\bar{p}$
- Stress tensor (committed one) $\bar{\sigma}_0$
- Back-stress ratio tensor $\bar{\alpha}_0$
- Unit normal to yield surface vector $\bar{n}$

9. Apply penalties to the averaged zone parameters to meet the consistency condition and maintain the yield surface inside the greater of the bounding and dilatancy surfaces.
10. Calculate image back-stress ratios and inner products for the averaged zone parameters.
11. Calculate daxn for the averaged zone parameters and determine whether a loading reversal has occurred.
12. Compute Dilatancy D and Plastic Modulus K_p for the past average step in the zone.
13. Compute plastic volumetric strain for use in fabric terms.
14. If $\left(\boldsymbol{\alpha}^d - \boldsymbol{\alpha}\right) : \boldsymbol{n} < 0$, update the fabric tensor for the zone and if exceeding its former value, update the cumulative fabric term.

$$z = z - \frac{c_z}{max\left(1, \dfrac{z_{cum}}{2 z_{max}}\right)} \frac{d\bar{\varepsilon}_v^{pl}}{D}\left(z_{max}\bar{n} + z\right)$$

15. Update the relative state parameter, the bounding and dilatancy stress ratios, the elastic shear modulus (depends on fabric) and the elastic bulk modulus for the next step.
16. Update the initial and previous initial back-stress values and the strain increment accumulators.
17. Update initial back-stress ratios upon reversal.
18. Commit zone stress tensor, zone mean stress, zone back-stress ratio tensor, zone stress ratio tensor to memory.

Table 3.2: Initialization function of PM4Sand (called during the first application of the model and whenever `First_Call=0`)

---

1. Obtain stresses from FLAC and create stress tensor (these will be the committed stresses from which the calculation will start):

$$\sigma_o^{ij}$$

2. Check stresses and calculate mean effective stress:

    a. If stresses compressive (following FLAC's sign convention that tensile stresses and strains are positive):

$$\sigma_o^{11} < 0 \rightarrow p_o = min\left(p_{min}, \frac{1}{2}\sigma_o^{ii}\right)$$

$$p_{min} = min\left(p_{min}, \frac{p}{200}\right)$$

$$p_{min2} = min\left(p_{min2}, \frac{p}{20}\right)$$

    b. If stresses tensile:

$$\sigma_o^{11} > 0 \rightarrow p_o = -\frac{P_{atm}}{20}$$

$$\sigma_o^{ij} = p_o \cdot [I]$$

3. Calculate relative state parameter and subsequently calculate the bounding and dilatancy stress ratios and A_{do} (from input property D_R and secondary parameters R, Q, n^b and n^d – see Chapter 4):

$$\xi_R = \frac{R}{Q - ln\left(-100\frac{p}{P_{atm}}\right)} - D_R$$

    a. If dense-of-critical ($\xi_R < 0$):

$$M^b = Mexp(-n^b\xi_R), \quad M^d = Mexp(n^d\xi_R)$$

$$A_{do} = 2.5\left[\frac{sin^{-1}\left(\frac{M^b}{2}\right) - \varphi_{cv}}{M^b - M^d}\right]$$

    b. If loose-of-critical ($\xi_R > 0$):

$$M^b = M \cdot exp\left(-\frac{n^b}{4}\xi_R\right), \quad M^d = M \cdot exp(4n^d\xi_R), \qquad A_{do} = 1.24$$

4. Check that initial stresses are inside the greater of the bounding and dilatancy surfaces and compute the committed back-stress and stress ratio tensors from the stress tensor:

$$M^{cut} = max(M^b, M^d), \quad M^{fin} = -\frac{2}{p_o} \cdot \sqrt{\frac{1}{2}(\sigma_o^{ij} - p_o[I]):(\sigma_o^{ij} - p_o[I])}$$

    a. If $M^{fin} > M^{cut}$ where M^{cut} is the greater of M^b and M^d:

$$r_o^{ij} = \left(\frac{\sigma_o^{ij} - p_o[I]}{p_o}\right)\left(\frac{M^{cut}}{M^{fin}}\right)$$

$$\sigma_o^{ij} = p_o[I] + r_o^{ij}p_o$$

$$\alpha_o^{ij} = r_o^{ij} \cdot \frac{M^{cut} - m}{M^{cut}}$$

    b. If $M^{cut} > M^{fin}$:

$$r_o^{ij} = \left(\frac{\sigma_o^{ij} - p_o[I]}{p_o}\right)$$

$$\alpha_o^{ij} = r_o^{ij}$$

5. Create/Initialize the initial back-stress ratio, initial previous back-stress ratio, minimum initial back-stress ratio and maximum initial back-stress ratio tensors (see also Section 2.5 on Stress Reversal):

   a. If $M^{fin} < 0.9M^b$:

   $$\alpha_{in}^{ij} = \alpha_o^{ij}$$

   b. If $M^{fin} > 0.9M^b$:

   $$\alpha_{in}^{ij} = \alpha_o^{ij} \left(\frac{0.9M^b}{M^{fin}} \right)$$

   Note that M^{fin} in the above expression would have been updated if step 4 had required adjusting the stresses. The other back-stress ratio history terms are then set as:

   $$\alpha_{inP}^{ij} = \alpha_{inMax}^{ij} = \alpha_{inMin}^{ij} = \alpha_{in}^{ij}$$

6. Calculate initial values of elastic shear modulus, elastic bulk modulus, plastic modulus, dilatancy:

   $$G = G_o P_{atm} \sqrt{\frac{-p_o}{P_{atm}}}$$

   $$K = G \frac{2(1 + v)}{3(1 - 2v)}$$

   $$K_p = 100G$$

   $$D = 0$$

7. Initialize fabric related terms (see Section 2.8) – note that these terms will be referring to the whole zone:

   $$p_{zp} = \frac{p_o}{100}$$

   $$z_{peak} = \frac{z_{max}}{100000}$$

   $$zxp = \mathbf{z}{:}p = 0$$

   $$zxpPk = -z_{max} \frac{p_o}{50}$$

   $$\mathbf{z}^{ij} = \mathbf{z}_{in}^{ij} = \mathbf{z}_\alpha^{ij} = z_{cum} = 0$$
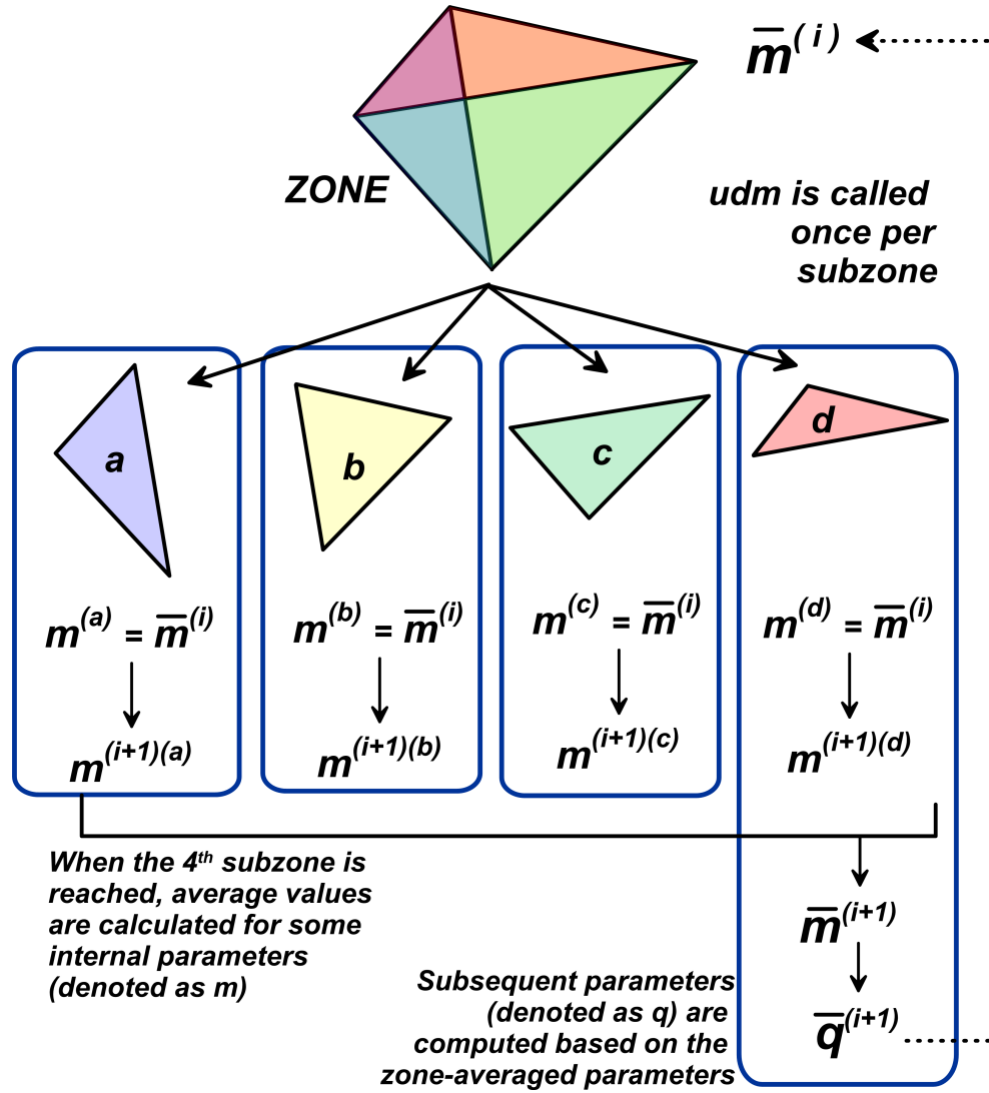
Figure 3.1. Schematic illustration of the averaging procedure followed in the implementation of PM4Sand: zone-averaged values are computed for some internal variables of the model, denoted as "m", at the end of each step, after which other internal parameters, denoted as "q", are computed based on the zone-averaged parameters.
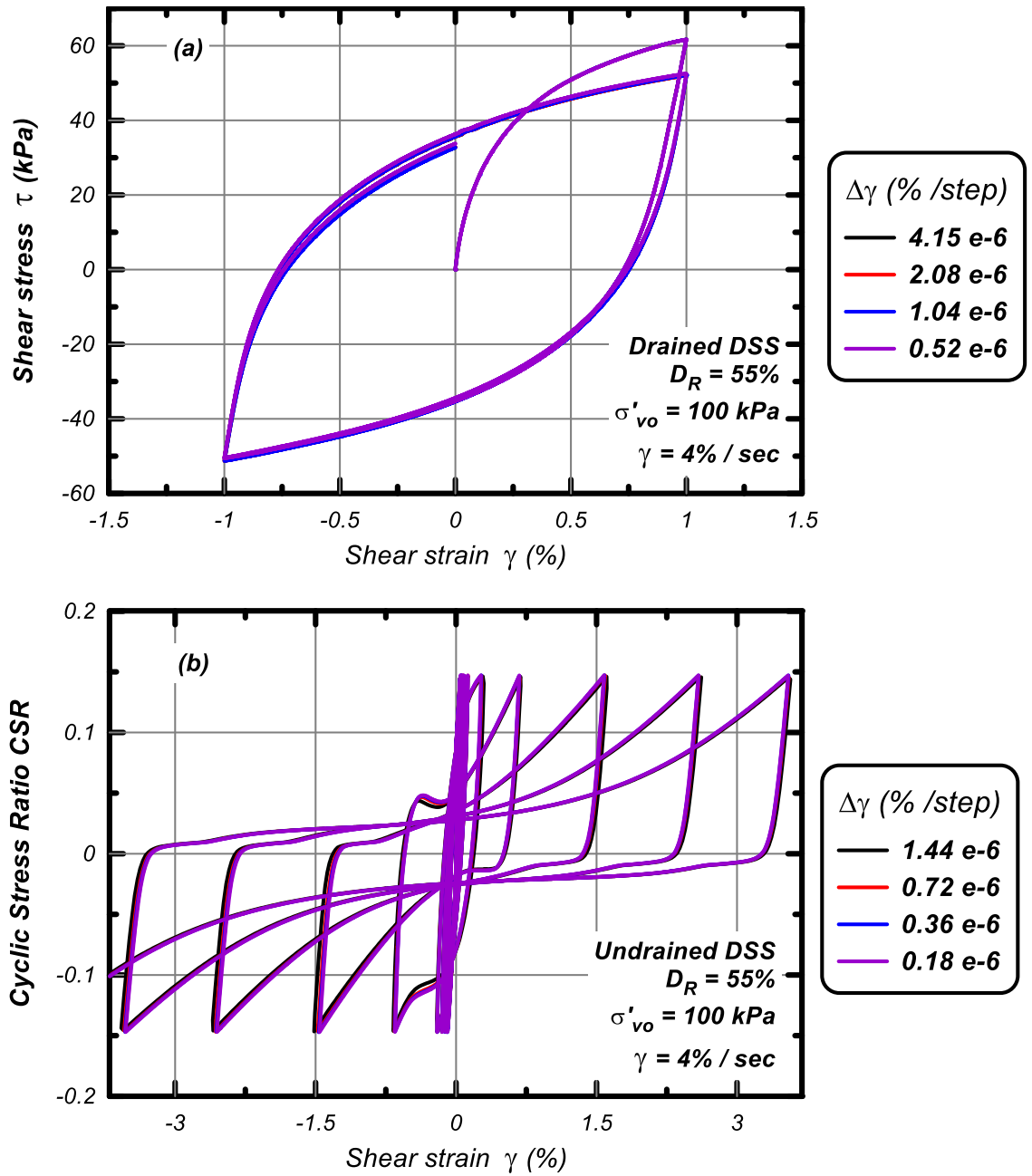
Figure 3.2. Effect of dynamic time step on the results obtained from (a) drained and (b) undrained cyclic DSS element test simulations (D_R=55%, σ'_{vo}=1atm) loaded at a shear strain rate of 12%/s. The black line in each case denotes the response obtained with FLAC's default dynamic time step.
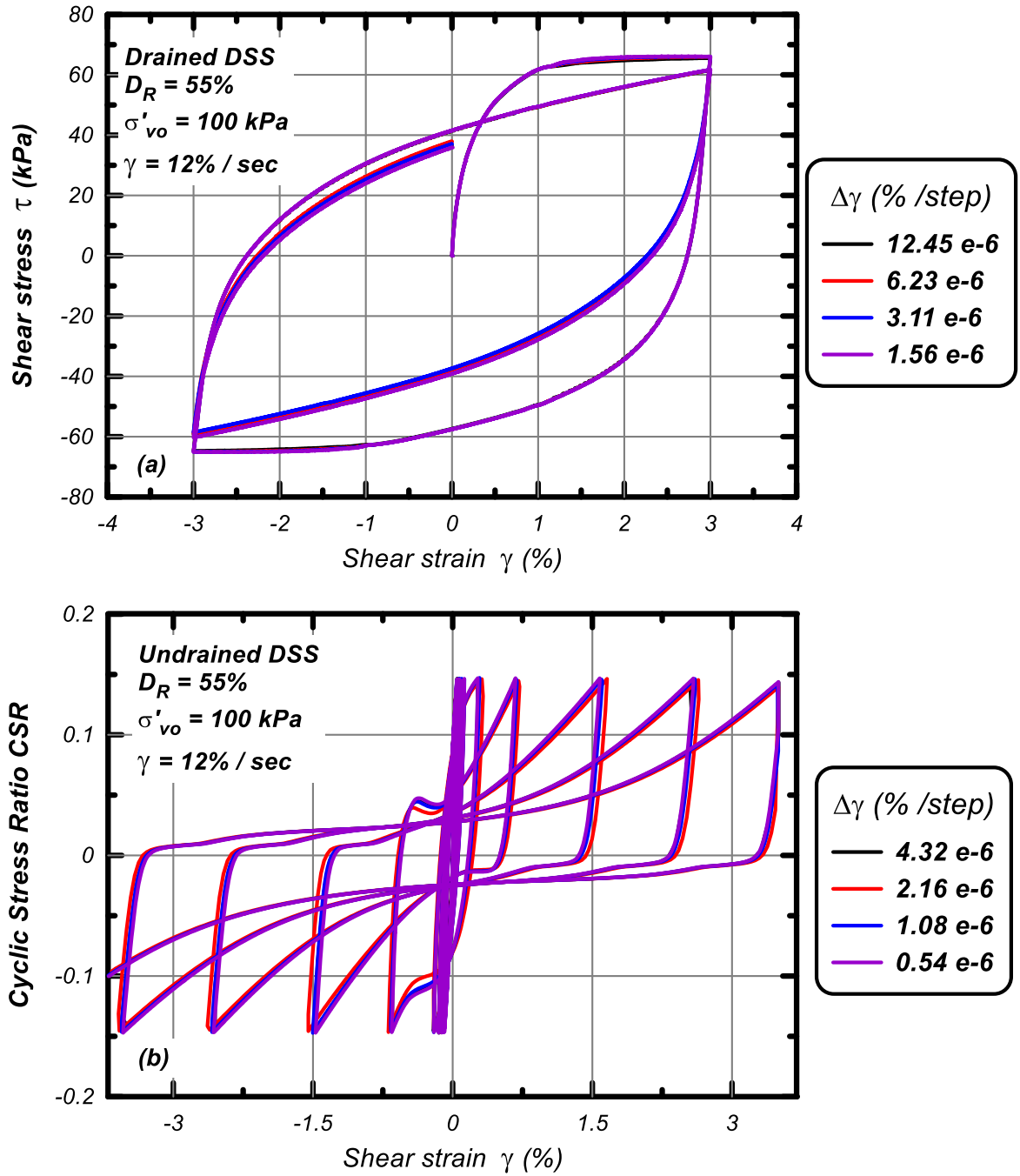
Figure 3.3. Effect of dynamic time step on the results obtained from (a) drained and (b) undrained cyclic DSS element test simulations (D_R=55%, σ'_vo=1atm) loaded at a shear strain rate of 4%/s. The black line in each case denotes the response obtained with FLAC's default dynamic time step.
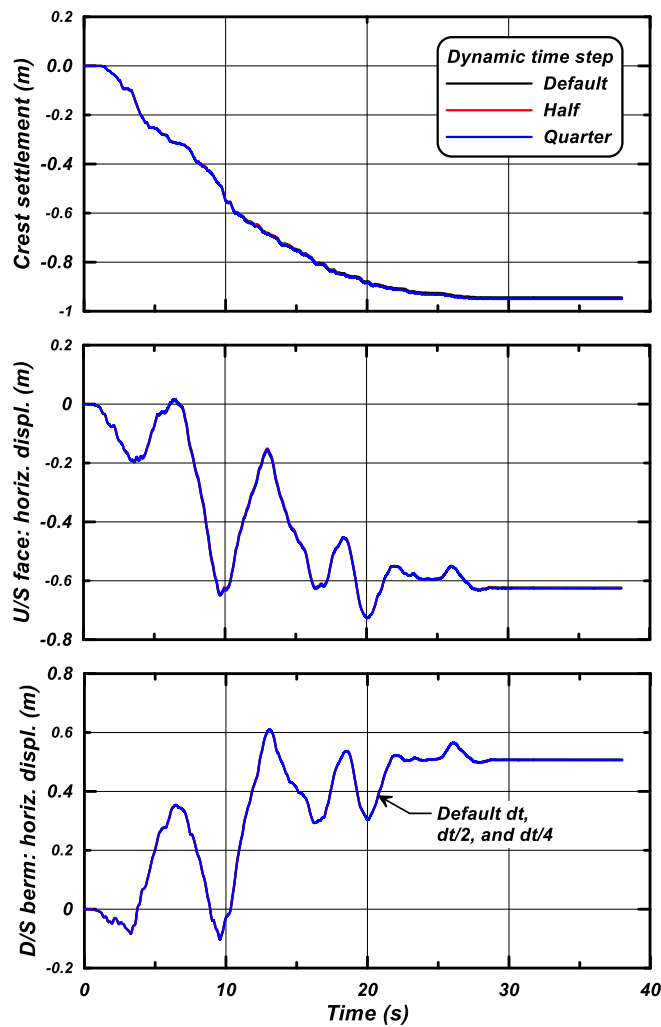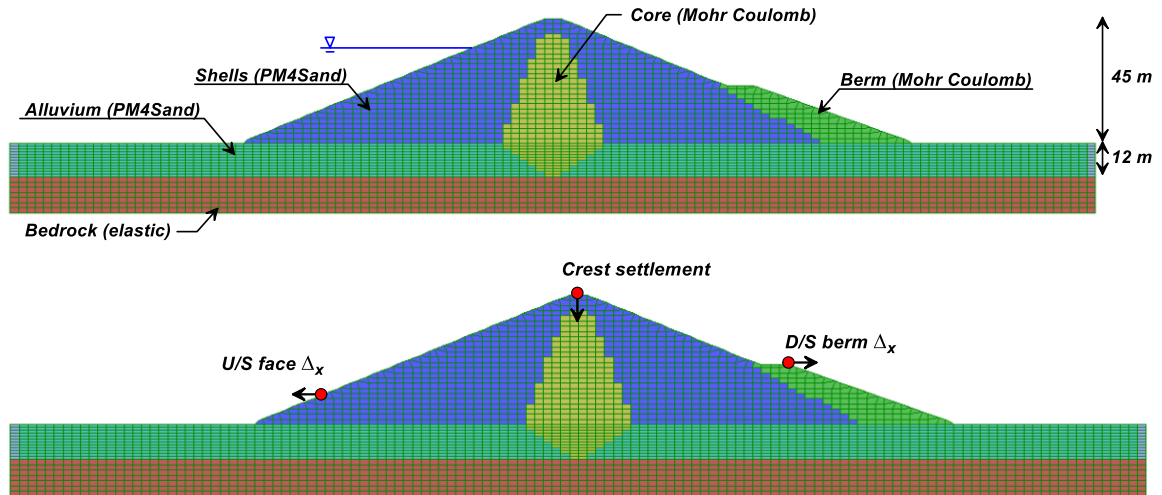
Figure 3.4. Effect of dynamic time step on seismic analysis of an embankment dam: cross-section, materials, and displacement monitoring points (top figures) and time histories of crest settlement and horizontal displacements for points on the upstream and downstream faces (lower figures).

4. MODEL INPUT PARAMETERS AND RESPONSES

4.1 Model input parameters

The model parameters are grouped into two categories; a primary set of six parameters (three properties, two flags, and atmospheric pressure) that are most important for model calibration, and a secondary set of parameters that may be modified from their default values in special circumstances.

Primary input parameters

The three primary input properties are the sand's apparent relative density D_R, the shear modulus coefficient G_o, and the contraction rate parameter h_{po}. These three parameters are discussed below and summarized in Table 4.1.

Relative density (D_R) can be estimated in practice by correlation to penetration resistances. For example, a common form for SPT correlations is,

$$D_R = \sqrt{\frac{(N_1)_{60}}{C_d}}$$

(94)

where D_R is expressed as a ratio rather than a percentage. Idriss and Boulanger (2008) reviewed published data and past relationships, and then adopted a value of $C_d = 46$ in the development of their liquefaction triggering correlations. For the CPT, they similarly reviewed available relationships and arrived at the following expression,

$$D_R = 0.465 \left(\frac{q_{c1N}}{C_{dq}} \right)^{0.264} - 1.063$$

(95)

for which they adopted $C_{dq} = 0.9$. For the example loading responses shown later, D_R values of 35%, 55%, and 75% were used, which would be correlated to SPT $(N_1)_{60}$ values of 6, 14, and 26 by the above correlations.

The input value of D_R is best considered an "apparent relative density," rather than a strict measure of relative density following conventional laboratory tests. The input value of D_R influences the response of the model and thus it is just another input parameter that the user can adjust as part of the calibration process. The above correlations are provided for the purpose of obtaining a reasonable estimate for the apparent D_R so that the resulting model behaviors are also reasonable. There are situations, however, where the user may choose to adjust the input D_R, up or down relative to the above relationships, to improve its calibration to some other relationship or data.

73

The second primary input parameter is the constant G_o which controls the elastic (or small-strain) shear modulus. The equation for the elastic shear modulus (Equation 23) at the time of model initialization can be simplified to,

$$G = G_o p_A \left(\frac{p}{p_A} \right)^{1/2}$$ (96)

The full equation for the elastic shear modulus includes adjustments for the effects of stress-ratio (Equation 24) and fabric (Equation 86), but these are both unity at the time of model initialization. The elastic shear modulus can be calibrated to fit in-situ V_s measurements, according to,

$$G = \rho \cdot (V_s)^2$$ (97)

or alternatively fit to values of V_s that may be estimated by correlation to penetration resistances. For the examples shown herein, the correlation by Andrus and Stokoe (2000) in Figure 4.1 was used, with a slight modification that constrains the extrapolation to very small $(N_1)_{60}$ values, as shown in the figure,

$$V_{s1} = 85 \left[(N_1)_{60} + 2.5 \right]^{0.25}$$ (98)

The above relationships in combination with the default values for the maximum and minimum void ratios (described later) produce V_{s1} values of 145, 171, and 196 m/s and corresponding G_o values of 477, 677, and 906 for the D_R values of 35%, 55%, and 75%, respectively.

Calibration of G to fit in-situ V_s measurements requires an estimate for the in-situ coefficient of earth pressure at rest (K_o) for computing p (i.e., the mean of the vertical and horizontal stresses for the present 2D implementation; Equation 2). Maintaining consistency between the calibration procedure and the boundary value problem solution requires that the initial K_o conditions in the boundary value problem reasonably match the value assumed during calibration.

Alternatively, the above expressions were combined together with a range of typical densities to arrive at the following simpler expression for estimating G_o,

$$G_o = 167 \sqrt{(N_1)_{60} + 2.5}$$ (99)

This expression produces G_o values of 487, 678, and 892 for the D_R values of 35%, 55%, and 75%, respectively.

The third primary input parameter is the constant h_{po} which is used to modify the contractiveness and hence enable calibration of the model to specific values of cyclic resistance ratio (CRR). For the examples presented herein, the target CRR values were based on the liquefaction triggering correlation by Idriss and Boulanger (2008) in Figure 1.2. This relationship produces target CRR values for an effective overburden stress of 1 atm and an earthquake magnitude of M=7.5 of 0.090, 0.147, and 0.312

for the corresponding SPT $(N_1)_{60}$ values of 6, 14, and 26, respectively. The corresponding values of h_{po} to achieve these CRR values, given the already set values for D_R and G_o, are 0.52, 0.40 and 0.62, respectively.

The value of atmospheric pressure, p_A, should also be specified in the unit set being used for the analysis. If not specified, it will default to 101,300 Pascal.

The flag FirstCall is used to re-set the back-stress ratio history terms equal to the current stress ratio, and to erase all fabric terms. The first time the model is called, the flag should be unspecified or have a value of 0. The model will then initiate the back-stress ratios and all pertinent history terms using the current state of stress. The flag is then set equal to 1.0 internally. If FirstCall is later set equal to 0.0 using the property command in FLAC, this will cause the material to re-initiate all internal terms, thereby re-setting the back-stress and stress ratio history terms and erasing all fabric terms. FirstCall should usually be set to 0.0 just before initiating dynamic earthquake loading. Otherwise, the model will retain memory of the loading during the static initiation of the model, which may or may not be desired.

The flag PostShake is used during the post-shaking portion of a simulation to improve the modeling of post-liquefaction reconsolidation strains. The flag is set to 0 internally and remains 0 unless the user specifies otherwise. If the flag is set to 1.0, the elastic moduli will be reduced according to the expressions presented previously. PostShake should only be set to 1.0 at the end of strong shaking, as the reductions in elastic moduli were not calibrated for cyclic loading behavior.

Table 4.1 – Primary input parameters (parameter names in square brackets correspond to the input name to be used within FLAC)

Parameter [FLAC property name]	Comments
D_R [D_r]	**Apparent relative density:** Primary variable controlling dilatancy and stress-strain response characteristics. Input as a fraction, not as a percentage. Commonly estimated based on CPT or SPT penetration resistances, such as the following relationships used by Idriss and Boulanger (2008): $$D_R = \sqrt{\frac{(N_1)_{60}}{C_d}}$$ with $C_d = 46$, and $$D_R = 0.465\left(\frac{q_{c1N}}{C_{dq}}\right)^{0.264} - 1.063$$ with $C_{dq} = 0.9$.
G_o [G_o]	**Shear modulus coefficient:** Primary variable controlling the small strain shear modulus, G_{max}. Should be chosen to match estimated or measured shear wave velocities according to $G_{max} = \rho\, V_s^2$. A value for G_o can be estimated based on the modified correlation between SPT $(N_1)_{60}$ and V_{s1} values shown in Figure 4.1. The value of G_o can thus be computed as, $$G_o = 167\sqrt{(N_1)_{60} + 2.5}$$
h_{po} [h_po]	**Contraction rate parameter:** Primary variable that adjusts contraction rates and hence can be adjusted to obtain a target cyclic resistance ratio, as commonly estimated based on CPT or SPT penetration resistances and liquefaction correlations. Calibration of this parameter should be performed last because its value can depend on the values assigned to other parameters.
p_A [P_atm]	**Atmospheric pressure** in the unit set being used. Defaults to 101,300 Pascals if not specified.
FirstCall [First_Call]	**Flag** used to re-set the back-stress ratio history terms equal to the current stress ratio, and to erase all fabric terms. FirstCall should usually be set to 0.0 at model initiation and/or just before initiating dynamic earthquake loading. Otherwise, the model will retain memory of the loading during the static initiation of the model, which may or may not be desired.

PostShake [Post_Shake]	**Flag** used during post-shaking portion of a simulation to improve modeling of post-liquefaction reconsolidation strains. PostShake should only be set to 1.0 after the end of strong shaking.

Secondary input parameters

Secondary input parameters are those parameters for which default values have been developed that will generally produce reasonable agreement with the trends in typical design correlations. The user must, however, still confirm through element loading calibrations that the default parameters are appropriate for their particular conditions. The secondary input parameters (21 in total) are listed in Table 4.2, along with commentary on the recommended default values.

The recommended default values for all secondary parameters have been embedded within the initialization section of the code and thus these parameters will take their default values unless the user specifies otherwise. In addition, the input logic is structured such that secondary parameters will take their default value if the user inputs a value of zero for that parameter.

Table 4.2 – Secondary input parameters

Parameter [FLAC name]	Comments
h_o [h_o]	Variable that adjusts the ratio of plastic modulus to elastic modulus. The default value of $h_o=(0.25+D_R)/2$, with a minimum value of 0.30, was chosen to provide reasonable G/G_{max} and damping relationships for the default value of G_o. This variable may require adjustment in combination with any adjustments to G_o.
e_{max} and e_{min} [e_max] [e_min]	The maximum and minimum void ratios affect the computation of density, and affect how volumetric strains translate into changes in relative state. Default values of 0.8 and 0.5, respectively, were adopted. Refinements in these parameters for a practical problem may not be necessary, as the calibration of other parameters will have a stronger effect on monotonic or cyclic strengths.
n^b [n_b]	Default value is 0.50. Controls dilatancy and thus also the peak effective friction angles. Note that M^b for loose-of-critical states is computed using $n^b/4$.
n^d [n_d]	Default value is 0.10. Controls the stress-ratio at which contraction transitions to dilation, which is often referred to as phase transformation. A value of 0.10 produces a phase transformation angle slightly smaller than ϕ_{cv}, which is consistent with experimental data. Note that M^d for loose-of-critical states is computed using $4n^d$.
A_{do} [A_do]	Default value is computed based on Bolton's dilatancy relationship at the time of initialization; typical values will be between 1.2 and 1.5.

z_{max} [z_max]	Default value is computed at the time of initialization as, $$z_{max} = 0.70 \cdot \exp(-6.1 \cdot \xi_{Ro}) \le 20$$ This returns 0.7 if ξ_R is initially 0.0, and increases to its maximum value of 20 with increasing dense-of-critical states. May require varying if the relationship between D_R and cyclic strength is significantly different from that implied by the liquefaction correlations of Idriss and Boulanger (2008).
C_z [c_z]	Default value is 250. Controls strain levels at which fabric affects become important.
C_ε [c_e]	Default value varies with D_R. The value is 0.5 for D_R less than 55%, and linearly decreases to its minimum value of 0.2 at $D_R = 75\%$. Can be used to adjust the rate of strain accumulation in undrained cyclic loading.
ϕ'_{cv} [phi_cv]	Default value is 33 degrees.
ν_o [pois]	Default value is 0.30. For 1-D consolidation of an elastic material, the value of K_o would correspond to, $$K_o = \frac{\nu}{1-\nu}$$ The default value for ν results in a K_o value of 0.43 in 1-D consolidation.
C_{GD} [G_degr]	Default value is 2.0. The small-strain elastic modulus degrades with increasing cumulative plastic deviator strains (z_{cum}). The maximum degradation approaches a factor of $1/C_{GD}$.
C_{DR} [C_DR]	Default value is computed at the time of initialization as, $$C_{DR} = 5 + 25 \, (D_R - 0.35) \le 10$$ Controls the rotated dilatancy surface and is applied to reduce the rate under which dilatancy is increasing.
$C_{K\alpha f}$ [C_kaf]	Default value varies with D_R. as, $$C_{K\alpha f} = 5 + 220 \cdot (D_{Ro} - 0.26)^3 \in [4.0; 35.0]$$ The value is 4.0 for D_R less than 10%, and increases to its maximum value of 35.0 at $D_R = 77\%$. This variable controls the effect that sustained static shear stresses have on plastic modulus.
Q [Q_bolt]	Default value is 10. Default value is for quartzitic sands per recommendations of Bolton (1986).
R [R_bolt]	Default value is 1.5. Default value for quartzitic sands would be 1.0 per recommendations of Bolton (1986); a slight increase in R is used to lower the critical state line to better approximate typical results for direct simple shear loading.
m [m_par]	Default value is 0.01. Default value provides reasonable modeling and numerical stability.
$F_{sed,min}$ [F_sedmin]	Default value is set at time of initialization and equal to 0.04. Controls the minimum value the reduction factor of the elastic moduli can attain during reconsolidation (used when Post_Shake=1.0).
$p'_{sed,o}$ [p_sedo]	Default value is $-P_{atm}/5$. It is the mean effective stress up to which reconsolidation strains are enhanced when Post_Shake=1.0

cr$_{hg}$ [MC_ratio]	Nominal plastic shear strength ratio used to compute c$_{hg}$ at the time of initialization or when FirstCall is set equal to 0. Default value is 0.005.
c$_{hg}$ [MC_c]	Nominal plastic shear strength assigned at initialization or when FirstCall is set equal to 0. It is computed as the greater of: (1) cr$_{hg}$ times p, and (2) the user-specified value for c$_{hg}$. Thus, the user-specified value for c$_{hg}$ is the minimum value it will be assigned.

Tracking variables

Many of the parameters internal to PM4Sand may be tracked for debugging purposes. The table below lists six internal parameters which may be of interest. Other internal parameters which can be tracked include: max_G, max_K, pmin, pmin2, MM, alfa_11, alfa_12, r_11, r_12, aIn_11, aIn_12, aInP_11, aInP_12, z_11, z_12, zcum, zpeak, zxpPk, pzp, zxp, Cka, eqsum, evsum, LoadInd, Dilat, Kp, zabs, evol, eq_11, eq_22, eq_12, epsIncr and daxn. Note that Cka tracks the product of the C$_{rev}$ and C$_{k\alpha}$ terms. Other internal parameters are visible through the FLAC interface, and can be phonetically mapped to different terms in constitutive equations in this manual.

Table 4.3 – Internal parameters available for tracking

Parameter [FLAC Name]	Comments
M^b [Mb]	Bounding surface stress ratio
M^d [Md]	Dilatancy surface stress ratio
Mcur [Mcur]	Current stress ratio
G [shearG]	Elastic shear modulus
K [bulkK]	Elastic bulk modulus
ξ_R [rsp]	Relative state parameter
D$_R$ [Dr]	Relative density, which evolves in response to volumetric strains. Note that the input parameter D_r is an initial parameter and does not evolve during an analysis.

4.2 Example calibration and model responses for a range of element loading conditions

The response of the model is illustrated in this section by presenting simulation results for a set of input parameters that were calibrated to emphasize realistic modeling of liquefaction behavior. Results are presented for sands having initial apparent relative densities of 35%, 55%, and 75% with corresponding SPT $(N_1)_{60}$ values of approximately 6, 14, and 26, respectively, based on the correlations presented previously. All secondary input parameters were assigned the default values summarized previously in Table 4.2. Values for G_o were obtained using the previously presented correlation between SPT $(N_1)_{60}$ values and overburden-corrected shear wave velocity V_{S1} (Figure 4.1). Values for h_{po} were obtained by matching the CRR values from direct simple shear (DSS) simulations with the $CRR_{M=7.5}$ values that were computed using the SPT-based liquefaction triggering correlation by Idriss and Boulanger (2006, 2008); an SPT-based estimate of CRR for an M=7.5 earthquake and effective overburden stress of 1 atm was assumed to be approximately equal to the CRR corresponding to 15 uniform loading cycles causing a peak shear strain of 3% in direct simple shear loading. The model input parameters for the examples presented in this section are summarized in Table 4.4 below.

Table 4.4. Input parameters for example element responses

Scenario field condition				Model input parameters [a]		
D_R	$(N_1)_{60}$	V_{S1} using Andrus & Stokoe (2000)	$CRR_{M=7.5}$ using Idriss & Boulanger (2008)	D_R	G_o	h_{po}
0.35	6	145	0.090	0.35	477	0.52
0.55	14	171	0.147	0.55	677	0.40
0.75	26	196	0.312	0.75	906	0.62

(a) All secondary input parameters were assigned the default values listed in Table 4.2.

Undrained cyclic loading

The undrained cyclic loading responses for the calibrated models are illustrated in Figures 4.2-4.4. These figures show the stress-strain and stress-path responses for undrained uniform cyclic loading in DSS with a vertical consolidation stress of 1 atm and initial static shear stress ratios (α) of 0.0, 0.1, and 0.2. Results for initial D_R of 35%, 55%, and 75% are presented in Figures 4.2, 4.3, and 4.4, respectively. Close up views of the stress-strain responses for D_R=35%, 55%, and 75% with an initial static shear stress ratio $\alpha = 0.0$ are presented in Figure 4.5.

The stress-strain responses for $\alpha = 0.0$ illustrate the model's ability to progressively reach larger and larger shear strains with continued cyclic loading, rather than locking up in a repeating loop as many plasticity models do. The ability to simulate the progressive accumulation of shear strains reflects the inclusion of the cumulative fabric terms, as described previously. The progressive increases in peak shear strain after the soil has reached a peak excess pore pressure ratio (r_u) greater than 98% are realistic in magnitude.

The stress-strain responses with nonzero initial static shear stresses show a progressive accumulation of shear strains in the direction of the initial static shear stress, with the rate and nature of the stress-strain response also being reasonably realistic.

CRR versus number of loading cycles – Effect of D_R and failure criterion

The CRR obtained for the calibrated models are summarized in Figure 4.6 showing the cyclic stress ratio (CSR) required to cause an excess pore pressure ratio (r_u) of 98% or single-amplitude shear strains of 1% and 3% versus number of uniform loading cycles. These results are for DSS loading with a vertical consolidation stress of 1 atm, an initial K_o of 0.5, and zero initial static shear stress ratio (α=0.0). The simulation results in this figure were fitted with a power law, for which the exponent "b" is labeled beside each curve.

The slopes of these CRR versus number of loading cycles are in good agreement with typical values obtained in laboratory testing studies. The exponent b is generally between 0.24 and 0.27 for these simulations. For the experimental data in Figure 1.3 the exponent b ranges from a low of 0.1 for one study on to a high of 0.34 for another. The ability of the model to produce reasonable slopes for these curves is attributed primarily to the changes in the plastic modulus and dilatancy relationships (Ziotopoulou and Boulanger 2012).

The slopes of the CRR versus number of loading cycle curves can be slightly adjusted by the parameters n^b and n^d. For example, repeating the same simulations for D_R=75% with n^b=0.8 (versus the value of 0.5 used herein) and with all other factors the same, increases the exponent b to values of 0.28 to 0.33. Ziotopoulou and Boulanger (2012) performed the same simulations using an earlier set of calibration parameters and got values for the exponent b ranging from 0.26 to 0.36. Note, however, that a greater value for n^b also results in greater peak friction angles and changes other responses as well, so such adjustments cannot be made independent of other features of behavior.

CRR versus number of loading cycles – Effect of confining stress

The effect of overburden stress on CRR for the calibrated models is illustrated in Figure 4.7 showing the CSR required to cause a single-amplitude shear strain of 3% versus number of uniform loading cycles for different confining stresses. These results are for DSS loading with initial K_o=0.5, initial static shear stress ratio (α) of 0.0, and vertical consolidation stresses of 1, 4, and 8 atm. The cyclic strengths for D_R=35% are the least affected by confining stress, while the cyclic strengths for D_R=75% are the most affected (reduced).

The equivalent K_σ values from these simulations, with the CRR values compared at 15 uniform loading cycles, are compared in Figure 4.8 to the relationships recommended by Boulanger and Idriss (2004) based on the framework presented in Boulanger (2003b). The simulated effects of confining stress are in good agreement, as expected since the expression for h_{po} was calibrated to this relationship.

CRR versus number of loading cycles – Effect of sustained shear stress

Summary plots of the CSR required to cause a single-amplitude shear strain of 3% versus number of uniform loading cycles are presented in Figure 4.9 for different values of initial static shear stress ratio. Results are presented for sand at D_R=35%, 55%, and 75% loaded in DSS with an initial K_o=0.5, a vertical consolidation stress of 1atm, and with initial static shear stress ratios (α) of 0.0, 0.1, 0.2, and 0.3. The model was initialized at the stress conditions corresponding to the end of 1D vertical consolidation, thereby setting the back-stress ratio terms prior to application of the initial horizontal static shear stress. The simulation results are reasonable in predicting that the presence of an initial static shear stress ratio results in lower cyclic strengths for loose sands (e.g., the D_R = 35% results) and greater cyclic strengths for denser sands (e.g., the D_R=75% results).

The effect of vertical effective stress on these behaviors is illustrated in Figures 4.10a and 4.10b showing the cyclic resistance ratio (3% peak shear strain in 15 uniform cycles of DSS loading) against initial static shear stress ratio for D_R of 35, 55, and 75% with vertical effective consolidation stresses of 100 and 400 kPa. Figures 4.10c and 4.10d show the same effects in terms of the static shear stress ratio strength correction factor K_α for the same overburden stresses. Increasing the vertical effective consolidation stress makes the material relatively more contractive, such that the effect of an initial static shear stress ratio is relatively more detrimental at 400 kPa than at 100 kPa. This general pattern is in agreement with experimental observations (Figure 1.5).

CRR versus number of loading cycles – Effect of K_o

Summary plots of the CSR required to cause a single-amplitude shear strain of 3% versus number of uniform loading cycles are presented in Figure 4.11 for different values of the lateral earth pressure coefficient at rest K_o (i.e., the ratio of horizontal to vertical effective stresses at the time of consolidation). Results are presented for sand at D_R=35%, 55%, and 75% loaded in DSS, a vertical consolidation stress of 1atm, and with zero initial static shear stress ratio.

Drained monotonic loading

The response for drained monotonic loading in direct simple shear (DSS) and plane-strain compression (PSC) for sand at D_R of 35%, 55%, and 75% under vertical confining stresses of ¼, 1, 4, and 16 atm is shown in Figures 4.12 and 4.13. The responses reasonably approximate the effects of relative density and confining stress on both the stress-strain and volumetric strain responses. The plots show the response up to shear strains of 10%, while the simulations tend to reach critical state conditions at shear strains of 40-60%. The post-peak rate of strain-softening is dictated by the dilation rate, which is constrained to approximate Bolton's (1986) stress-dilatancy relationship. The simulated post-peak softening is slower than often observed in experimental results (e.g., Figure 1.9) because drained laboratory experiments are often affected by strain localizations in dilating sands (e.g., Desrues et al. 1996, Sadrekarimi and Olson 2010); The rate of strain-softening in a dilating zone is much lower than represented by global measurements of stress and strain.

The peak effective friction angles from simulations of drained monotonic loading in DSS and plane strain compression (PSC) are shown versus vertical consolidation stress in Figure 4.14 where they are also compared to Bolton's (1986) relationship for plane strain conditions for Q=10 and R=1.5 (which

are the default values of Q and R that have been selected for the model). The peak friction angles are lower in DSS than in PSC because of the difference in how the friction angles are computed for this plot. For PSC, the peak friction angle is computed based on the peak stress ratio within the element, without any predetermined assumptions regarding the orientation of the plane on which it will occur. For DSS loading, the peak friction angle was computed as the inverse tangent of the peak stress ratio on the horizontal plane, following the same convention commonly used in practice for interpreting such tests. In the DSS simulation, however, the horizontal plane was not the plane of maximum stress obliquity, and therefore the interpreted peak friction angle is slightly lower than the value obtained in PSC. Computationally, both the DSS and PSC mobilize similar peak friction angles if the comparison is made only for the plane of maximum stress obliquity in both simulations; In the DSS, however, the stress ratio on the horizontal plane in the DSS simulations is often closer to $\sin(\phi)$ as opposed to $\tan(\phi)$, which results in the apparent differences shown in Figure 4.14. Despite these differences, the peak friction angles are reasonable and consistent with typical design correlations (e.g., Kulhawy and Mayne 1990).

Undrained monotonic loading

The undrained monotonic loading in direct simple shear (DSS) for sand at D_R of 35%, 55%, and 75% under vertical consolidation stresses of ¼, 1, 4, and 16 atm are shown in Figure 4.15, while the same responses are shown with normalization by the vertical consolidation stress in Figure 4.16. The stress-strain responses show strain hardening behavior at lower relative states than would be expected based on the experimental results for reconstituted sands, such as presented by Yoshimine et al. (1999). Experiments on loose reconstituted sands often show strain softening to some minimum shear stress ratio (e.g., quasi-steady state condition) before beginning to strain harden, and that minimum stress ratio is often in the range of 0.1 to 0.3. For the present calibration, the CRR for $D_R = 35\%$ sands under 1 atm of confining stress was targeted to be 0.090 based on a field-based liquefaction correlation, and it was not possible to calibrate the model to match both the target CRR values and the monotonic undrained strengths presented in Yoshimine et al. (1999). If the monotonic behavior was more important than the CRR values, then a different calibration would be required.

Drained, strain-controlled, cyclic loading from small to large strains

Drained strain-controlled cyclic loading in DSS for sand at D_R of 35%, 55%, and 75% under vertical consolidation stresses of 1, 4, and 16 atm with $K_o=1.0$ are shown in Figures 4.17 to 4.19, with results also shown for the equivalent modulus reduction (G/G_{max}) and equivalent damping ratio (ξ) versus cyclic shear strain amplitude (γ). Also shown on these figures are the modulus reduction and equivalent damping ratio curves recommended for sands at different depths by EPRI (1993). The simulated modulus reduction and equivalent damping ratio curves depend on the effective confining stress in a pattern and magnitude that is consistent with empirical design correlations, such as the ones by EPRI. The simulated modulus reduction curves for this calibration tend to be slightly higher than the empirical curves, whereas the simulated equivalent damping ratios are in reasonable agreement with the empirical curves over a fairly broad range of shear strain amplitudes. The model response for this calibration avoids the problem common to many plasticity models of producing excessively high equivalent damping ratios as shear strain amplitudes approach about one percent.

Drained, strain-controlled cyclic loading: Densification under large numbers of cycles

Drained strain-controlled cyclic loading in DSS for sand at D_R of 35%, 55%, and 75% subjected to 20 cycles at 1% shear strain under a vertical effective stress of 1 atm are presented in Figure 4.20 to illustrate the accumulation of volumetric strains with increasing number of constant-amplitude strain cycles. The model response with this calibration produces volumetric strains that are about twice the values expected based on the empirical data presented in Figure 1.12, although the general pattern of stress-strain behavior and its dependency on D_R and confining stress are reasonably consistent with the empirical data. Alternative model calibrations can produce better agreement with these behaviors, but they were generally found to require compromising the fit to the CRR correlations.

Post-liquefaction reconsolidation strains

The volumetric strains that develop during post-liquefaction reconsolidation of sand are difficult to model using the conventional separation of strains into elastic and plastic components because a large portion of the post-liquefaction reconsolidation strains are due to sedimentation effects (i.e., volume reductions while the effective stresses remain close to zero) which are not easily incorporated into either the elastic or plastic components of behavior. For example, it is common for many plasticity-based constitutive models to predict reconsolidation volumetric strains from a condition of r_u=100% that are only a fraction of one percent (Ziotopoulou and Boulanger 2013b), whereas experimental data show values ranging from one to four percent for most relative densities (e.g., Figure 1.12).

Volumetric strains due to post-cyclic reconsolidation, with and without the PostShake [`Post_Shake = 1.0`] option, are plotted in Figure 4.21 versus the maximum shear strain induced during undrained cyclic loading. Results are shown for sand at D_R = 35%, 55%, and 75% loaded in DSS with an initial K_o=0.5, a vertical consolidation stress of 1 atm, and zero initial static shear stress ratio. After cyclic loading to different maximum shear strains, the horizontal shear stress was reduced to zero such that the excess pore pressure was near its maximum possible value (e.g., r_u was approximately 98% or larger for cases with maximum shear strains of 3% or greater). The computed volumetric strains were less than about 0.25% with PostShake = 0 (default value) and are much smaller than expected based on common experimental data. The computed volumetric strains with `Post_Shake = 1.0` (imposed at the end of cyclic loading) are in much closer agreement with experimental data (Figure 1.14).

4.3 Example calibration with user-defined critical state undrained shear strength

Calibration of the model to a specified undrained critical state shear strength ($s_{u,cs}$) is illustrated in this section. The $s_{u,cs}$ for any set of calibration parameters can be computed from the critical state line (Figure 2.1) as,

$$s_{u,cs} = \frac{M}{2} \frac{P_A}{100} e^{\left(Q - \frac{R}{D_R}\right)} \tag{100}$$

The critical state line parameters Q and R can be adjusted to fit an experimentally determined critical state line (e.g., Kamai and Boulanger 2012) or fit an $s_{u,cs}$ estimated from a case history based correlation. Boulanger and Ziotopoulou (2018) illustrated how the model can be calibrated to a specific target $s_{u,cs}$ by setting R according to,

$$R = D_R \left[Q - \ln \left(\frac{2 s_{u,cs}}{M} \frac{100}{P_A} \right) \right]$$

(101)

The logic of this approach is illustrated in Figure 4.22 wherein the target $s_{u,cs}$ is used to compute p'_{cs} given M, which is then used to compute R given D_R and Q. Alternatively, the above expression can be rearranged to obtain the target $s_{u,cs}$ by adjusting Q instead of R.

The calibration of R or Q to obtain a target $s_{u,cs}$ is based on the $s_{u,cs}$ corresponding to the current D_R. If a numerical simulation procedure imposes undrained conditions (no fluid flow) such that the D_R does not change significantly during the simulation, then the model will produce the target $s_{u,cs}$ at large shear strains. If a numerical simulation allows fluid flow, then the D_R may increase or decrease throughout the simulation depending on the pore pressure diffusion pattern. In this latter case, the resulting changes in $s_{u,cs}$ during the simulation (per the above equations) needs to be recognized by the user.

Consider the example calibration for $D_R = 35\%$ in Section 4.2. This example calibration, referred to as Calibration 1 below, used $G_o = 477$ and $h_{po} = 0.52$ with all other parameters retaining their default values. Recall that Q and R have default values of 10 and 1.5, respectively. That calibration produces a $s_{u,cs}$ value of,

$$s_{u,cs} = \frac{1.089}{2} \frac{101.3 \, kPa}{100} e^{\left(10 - \frac{1.5}{0.35} \right)} = 167 \, kPa$$

For a zone with $\sigma'_{vc} = 100$ kPa, this corresponds to an initially dense-of-critical-state condition that produces $s_{u,cs} / \sigma'_{vc} = 1.67$.

A revised calibration, referred to as Calibration 2, is now presented for a case where the calibration includes targeting an $s_{u,cs} / \sigma'_{vc} = 0.07$ for a zone with $\sigma'_{vc} = 100$ kPa. The target $s_{u,cs}$ is therefore only 7 kPa, which is achieved by setting R to,

$$R = 0.35 \left[10 - \ln \left(\frac{2 (7 \, kPa)}{1.089} \frac{100}{101.3 \, kPa} \right) \right] = 2.611$$

The target V_{s1} and $CRR_{M=7.5}$ values remain unchanged, which means G_o remains unchanged whereas h_{po} had to be recalibrated to 2.2.

The responses of the above two calibrations to monotonic undrained DSS loading with $\sigma'_{vc} = 100$ kPa are shown in Figure 4.23. Calibration 1 results in a strongly dilative response whereas Calibration 2 produces the intended contractive response.

The responses of the above two calibrations to cyclic undrained DSS loading with $\sigma'_{vc} = 100$ kPa and an imposed CSR = 0.090 are shown in Figure 4.24. Calibration 1 produces a cyclic mobility response wherein cyclic shear strains progressively accumulate during cyclic loading. The specimen never develops flow liquefaction because it is always dense of critical state. Calibration 2 exhibits flow liquefaction, which is triggered by the generation of excess pore pressures during the cyclic loading. The specimen develops flow liquefaction because the peak shear stresses imposed during cyclic loading are greater than the $s_{u,cs}$.

The representation of post-liquefaction residual shear strengths in practice is complicated by various challenges and limitations as discussed in Boulanger et al. (2014, 2015). The $s_{u,cs}$ mobilized in the field, and the timing at which it is mobilized, will depend on pore pressure diffusion and associated void redistribution processes, which depend on the soil properties (e.g., initial relative density, cyclic strength, permeability), subsurface stratigraphy (e.g., layer thicknesses, slope angles, continuity of interfaces), and ground motion characteristics (e.g., shaking intensity, shaking duration, shaking history). Simulation of void redistribution processes and their timing are highly uncertain, such that pragmatic approximations for representing post-triggering residual shear strengths during and after strong shaking are often used in practice (see Boulanger et al. 2015 for additional discussion).
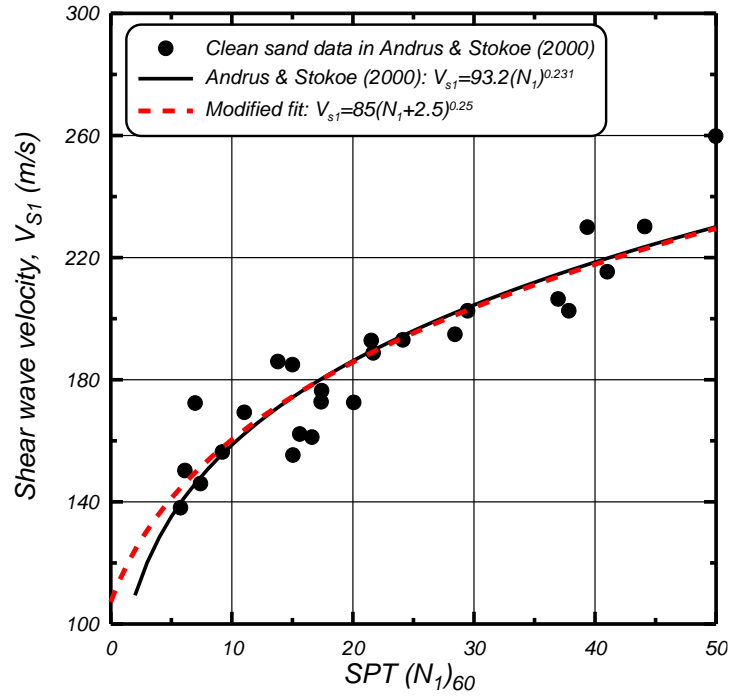
Figure 4.1. Correlation between overburden-corrected shear wave velocity and SPT penetration resistances in clean sands (after Andrus and Stokoe 2000).
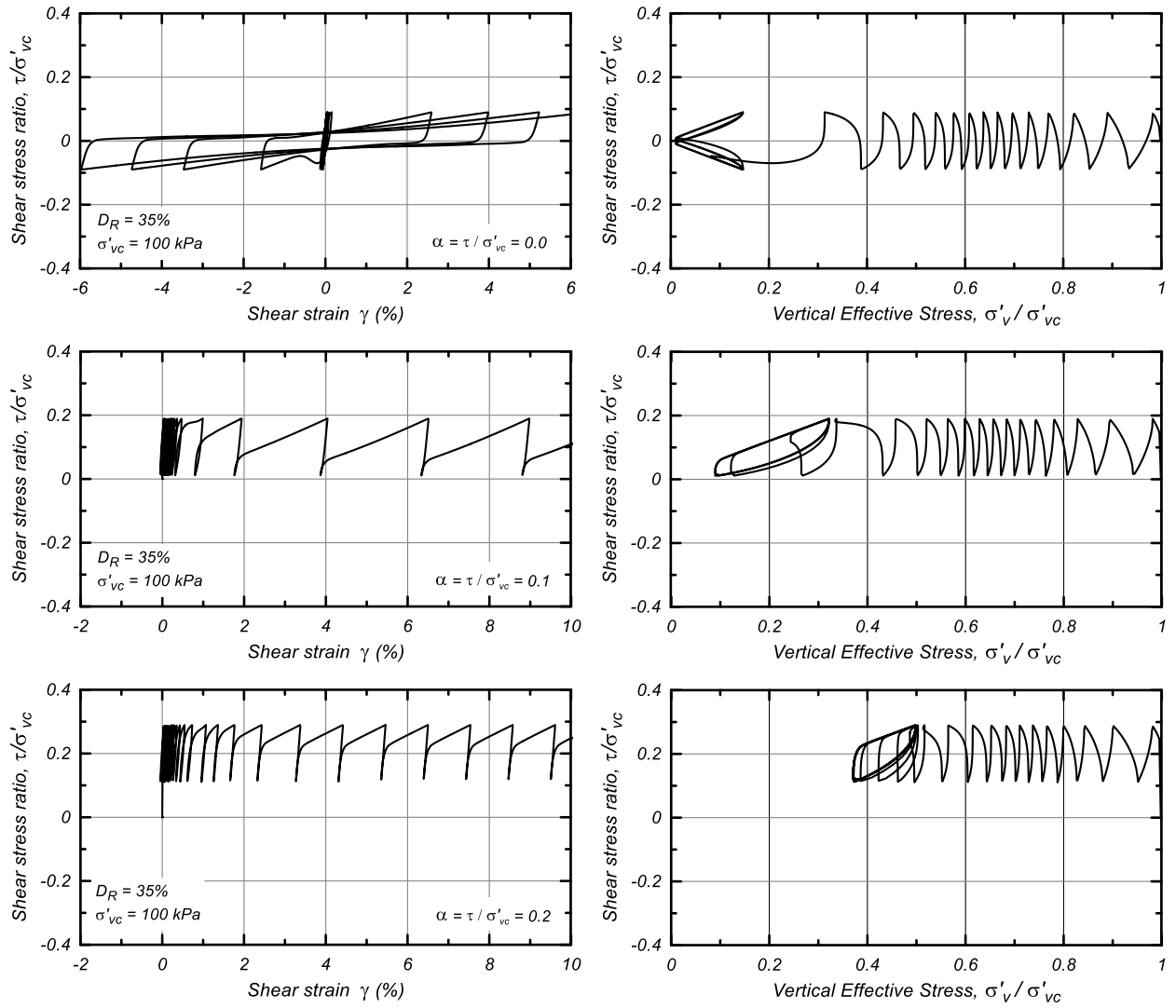
Figure 4.2. Undrained cyclic DSS loading response for $D_R = 35\%$ with vertical effective consolidation stress of 100 kPa and with initial static shear stress ratios of 0.0, 0.1, and 0.2.
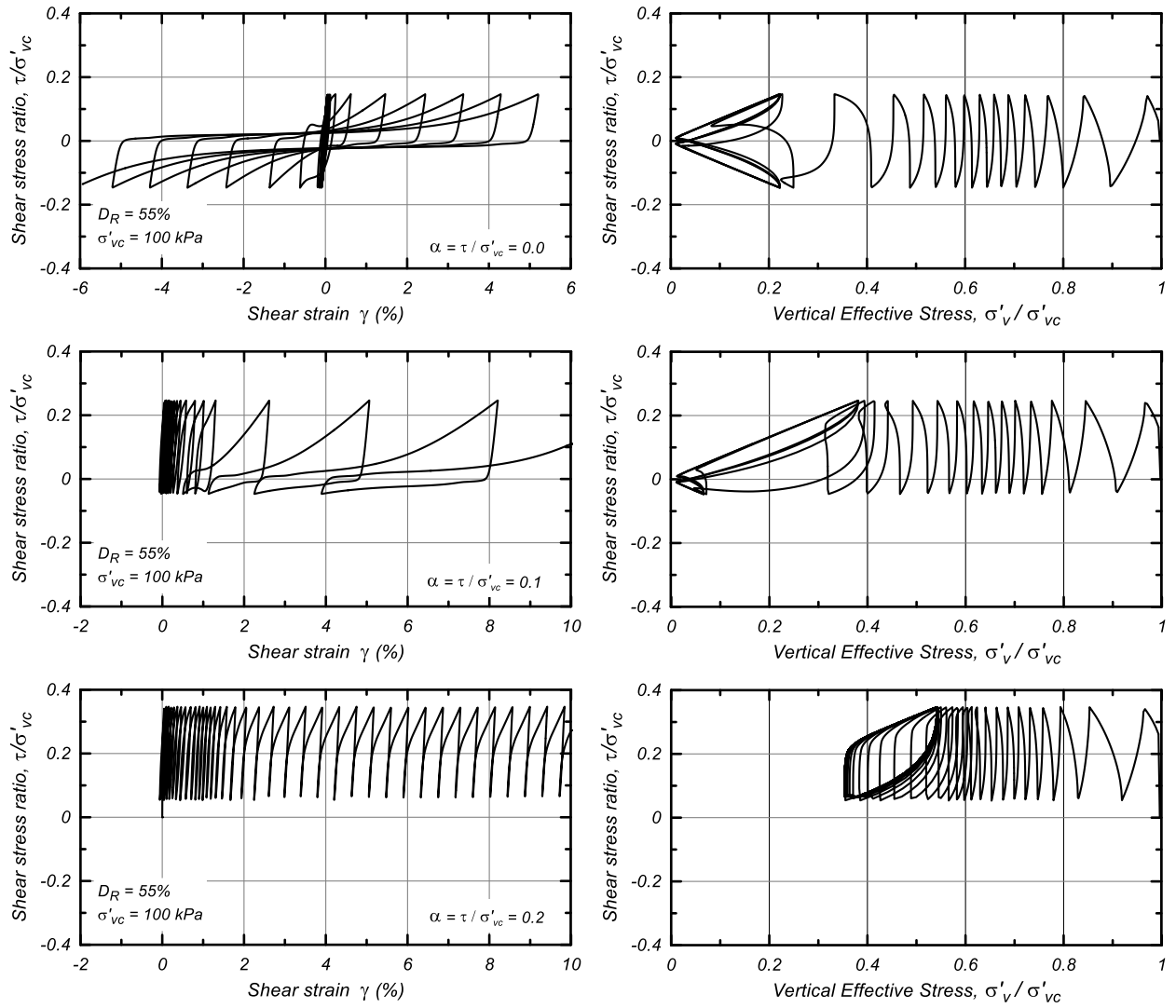
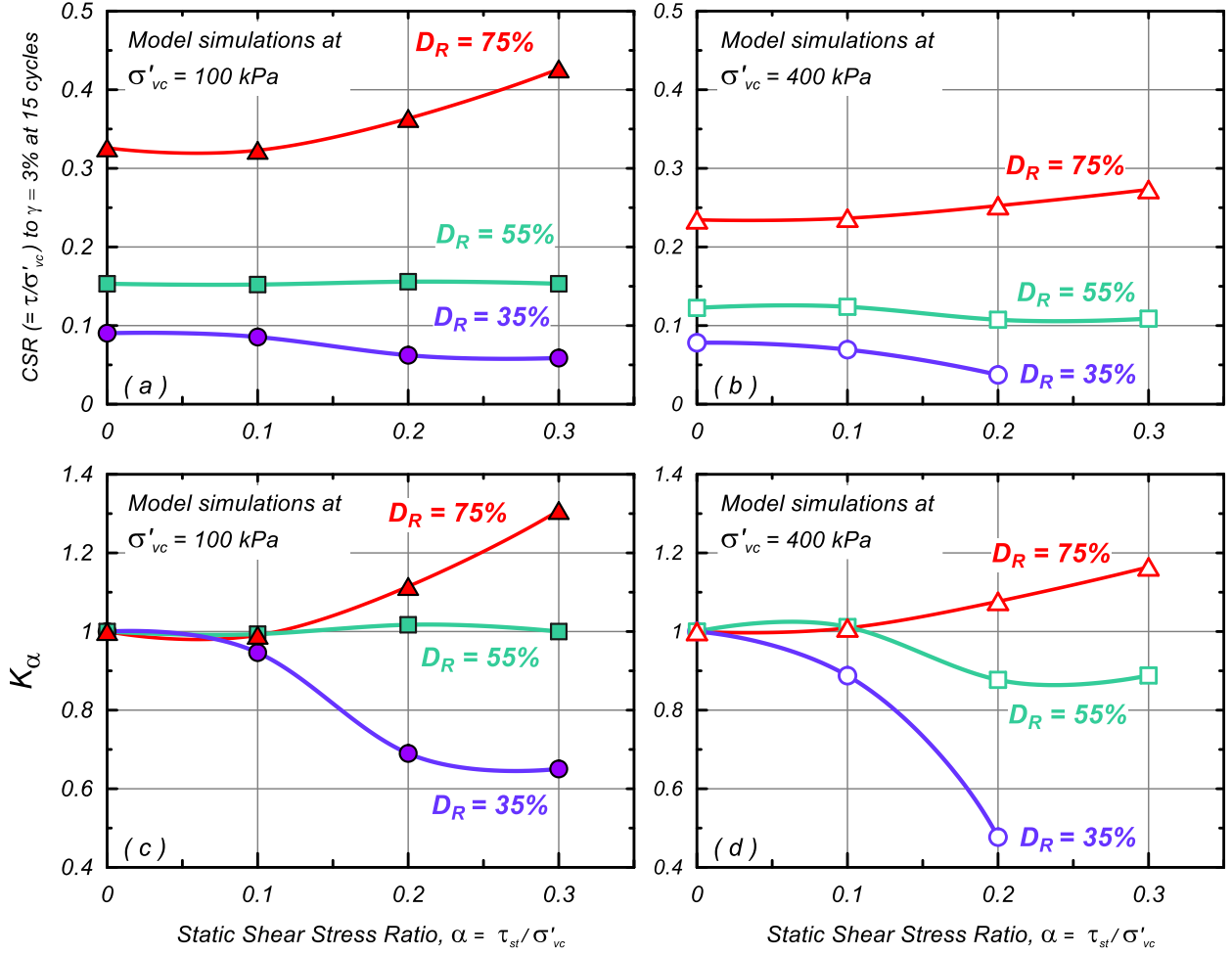Figure 4.3. Undrained cyclic DSS loading response for D_R = 55% with vertical effective consolidation stress of 100 kPa and with initial static shear stress ratios of 0.0, 0.1, and 0.2.

89
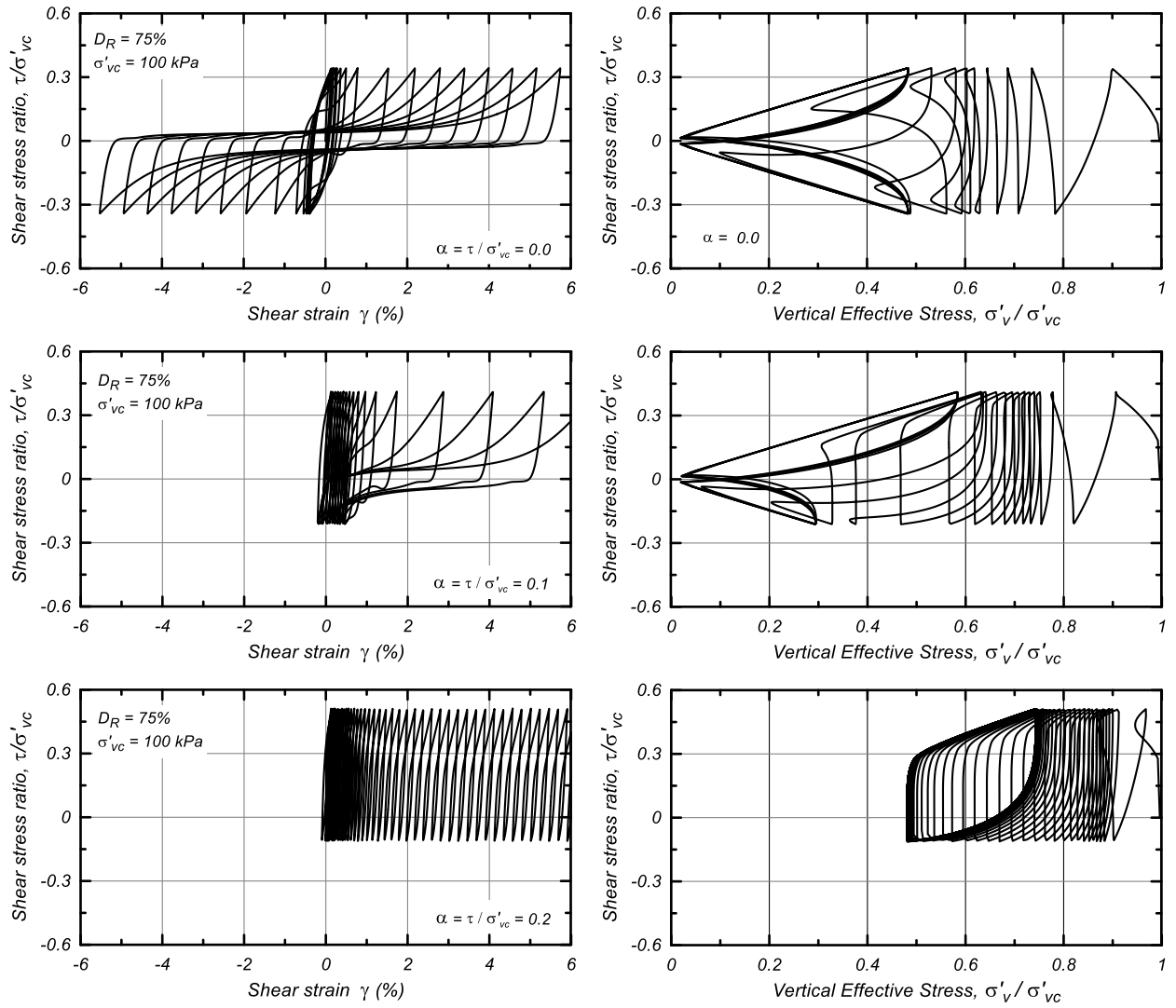
Figure 4.4. Undrained cyclic DSS loading response for D_R = 75% with vertical effective consolidation stress of 100 kPa and with initial static shear stress ratios of 0.0, 0.1, and 0.2.
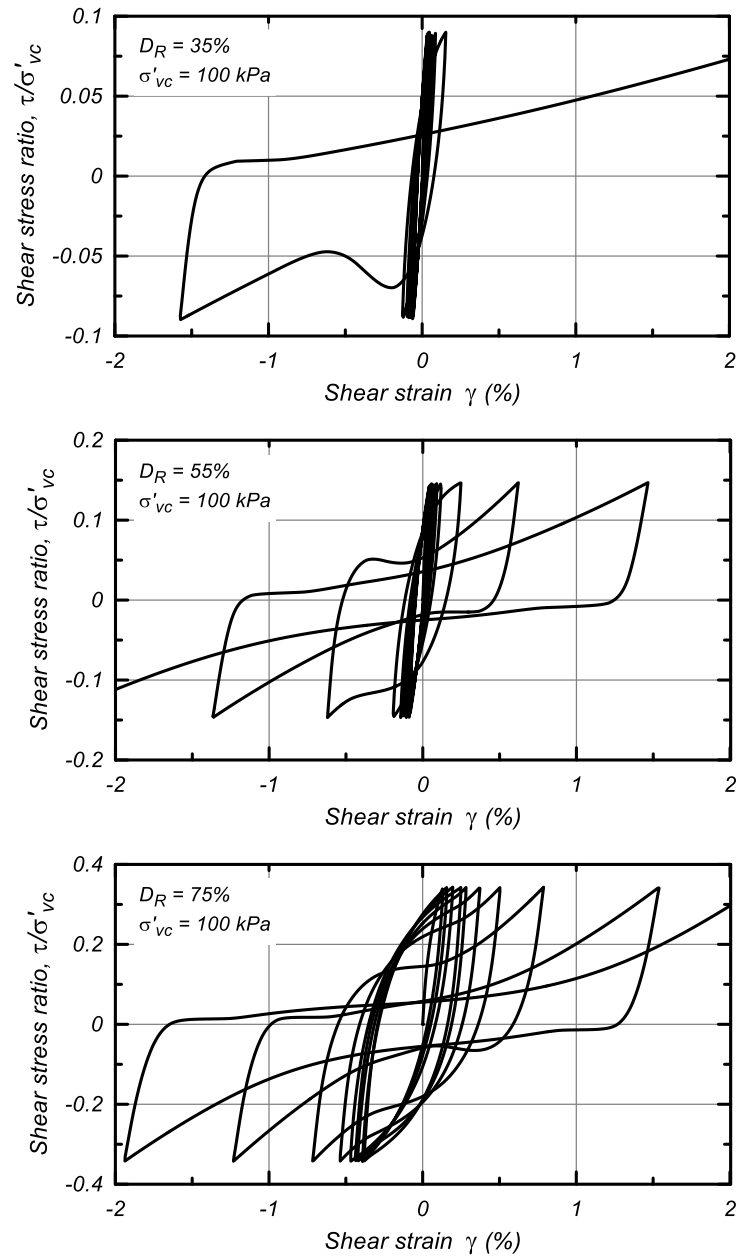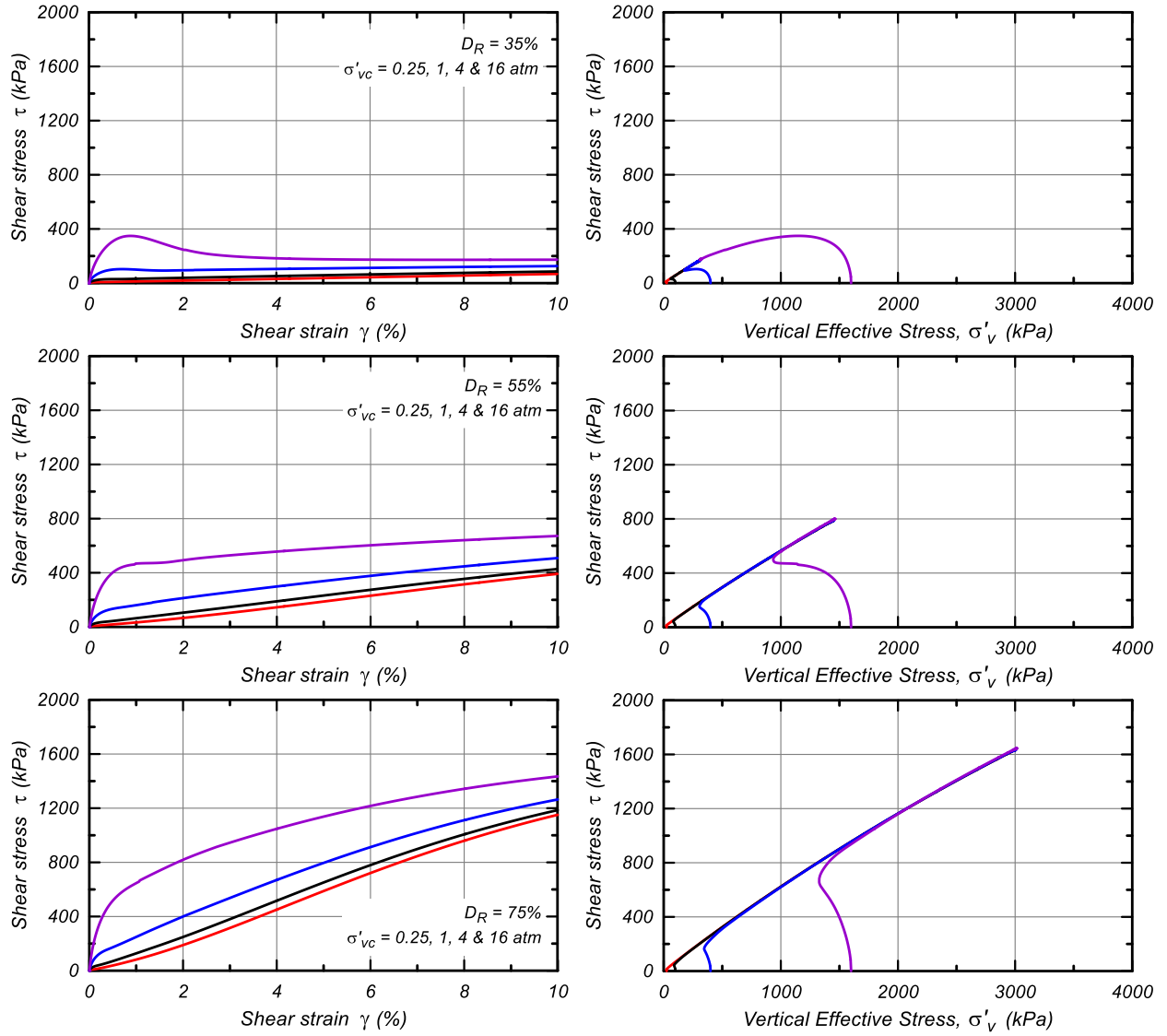
Figure 4.5. Undrained cyclic DSS loading responses for D_R = 35, 55, and 75% with a vertical effective consolidation stress of 100 kPa and without any initial static shear stress.
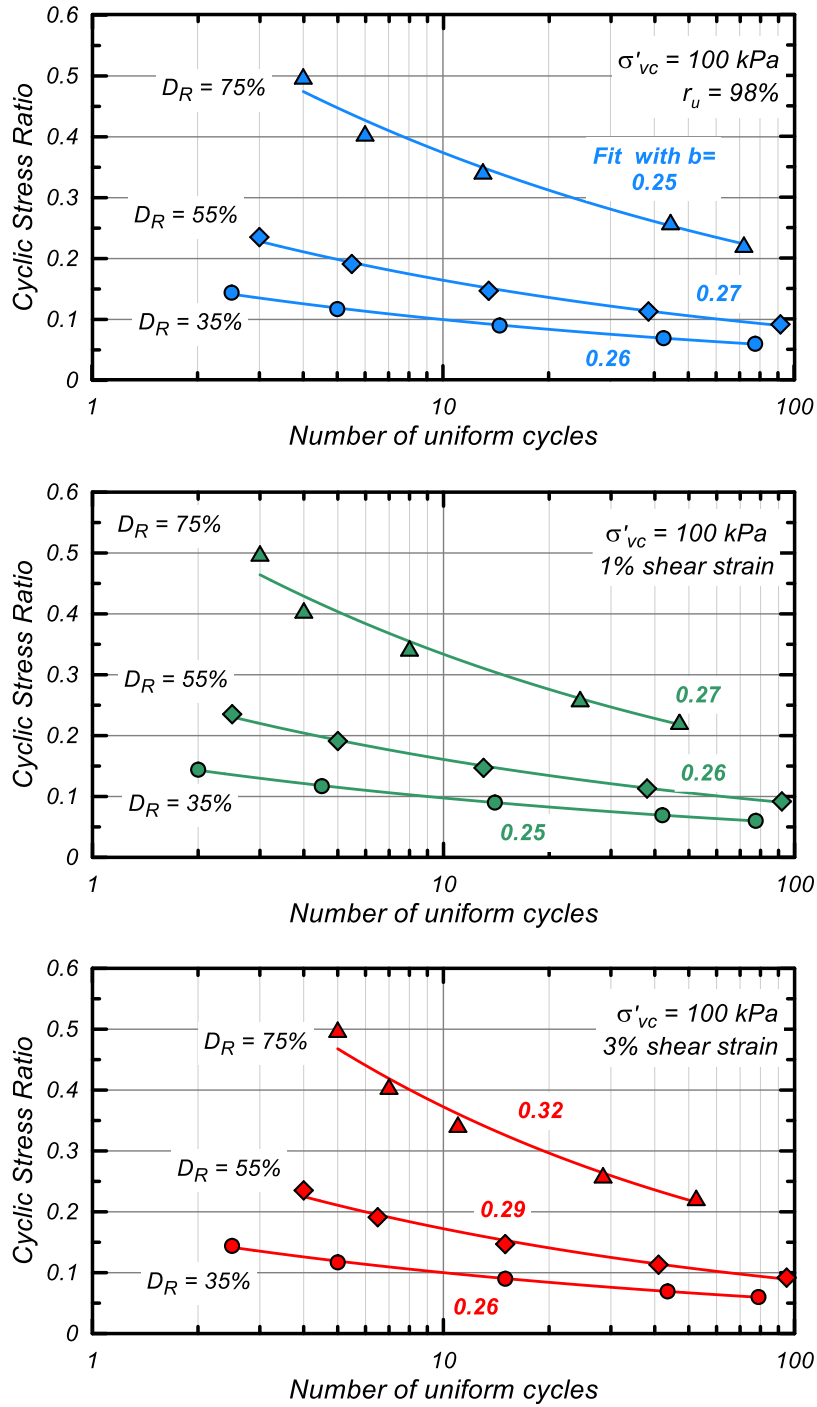
Figure 4.6. Cyclic stress ratios versus number of equivalent uniform loading cycles in undrained DSS loading to cause r_u=98% or single-amplitude shear strains of 1% or 3% for D_R = 35, 55, and 75% with a vertical effective consolidation stress of 100 kPa. Each set of CSR-N simulations was fit with a power relationship and the exponent b is labeled beside each curve.
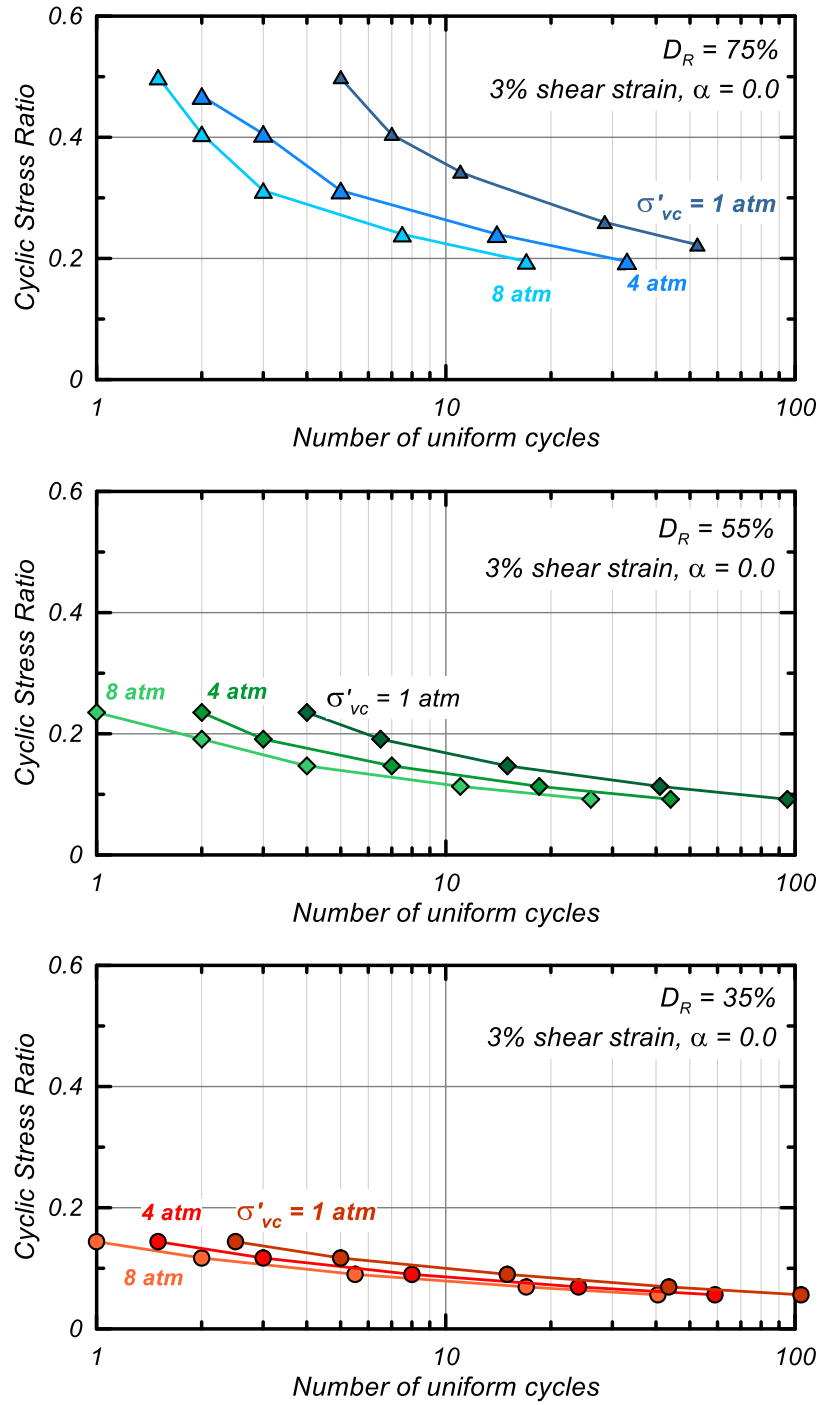
Figure 4.7. Cyclic stress ratios versus number of equivalent uniform loading cycles in undrained DSS loading to cause single-amplitude shear strain of 3% for D_R = 35, 55, and 75% with vertical effective consolidation stresses of 1, 4, and 8 atm.
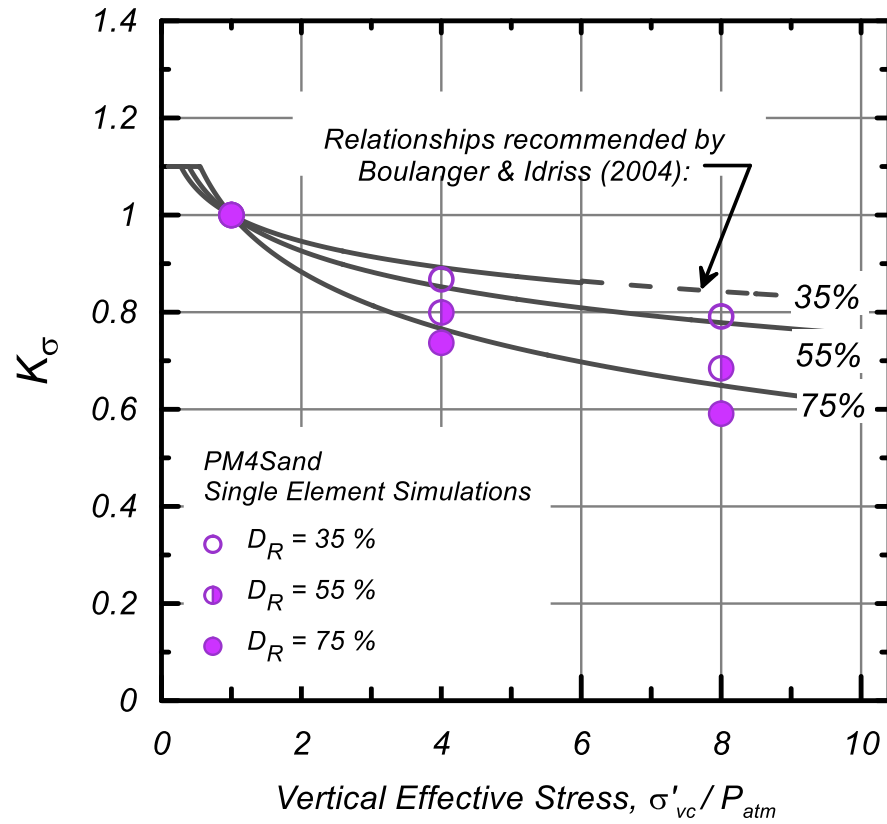
Figure 4.8. Comparison of K_σ factors, determined at 15 uniform loading cycles to cause 3% single-amplitude shear strain, from simulations versus relationships recommended by Boulanger and Idriss (2004).
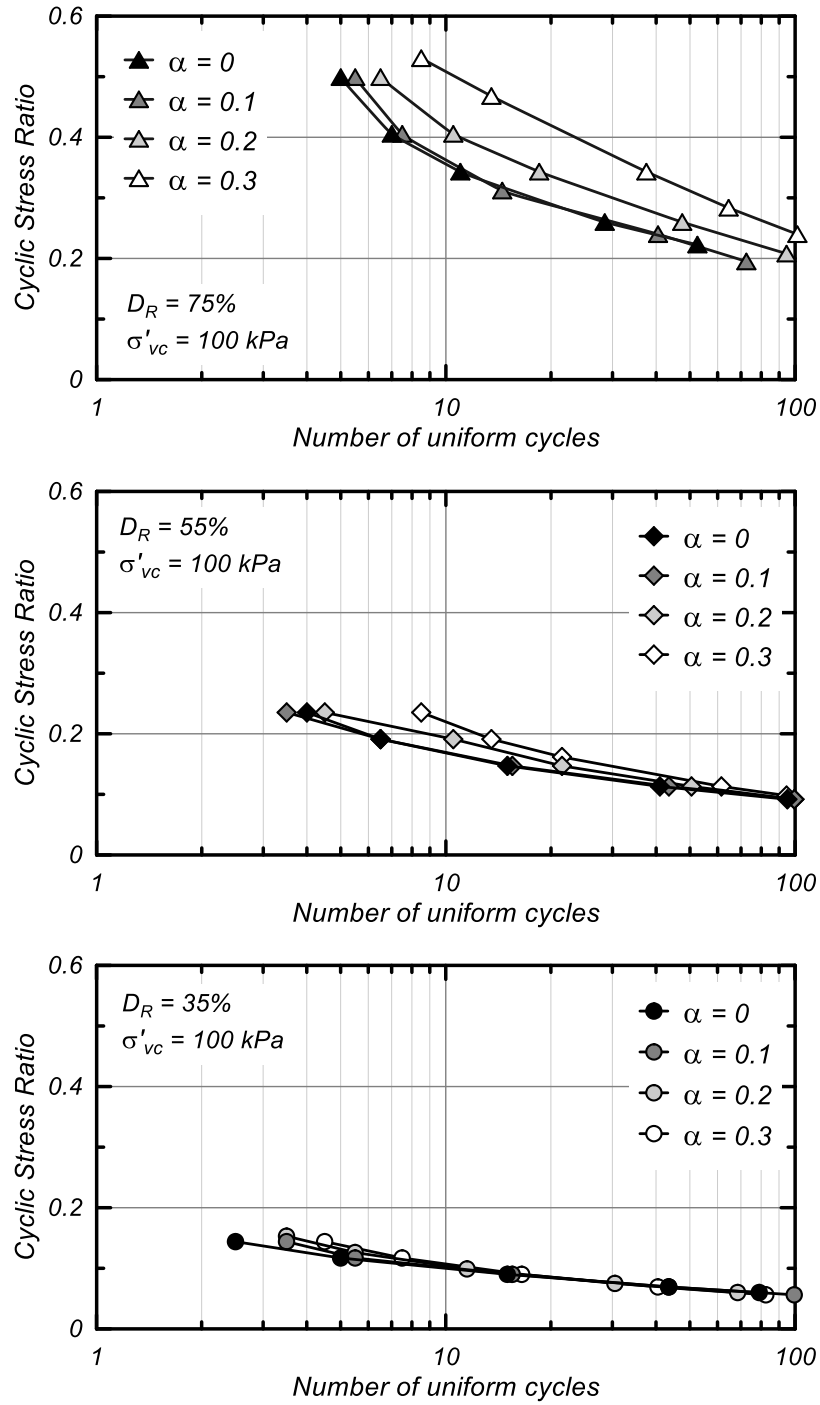
Figure 4.9. Cyclic stress ratios versus number of equivalent uniform loading cycles in undrained DSS loading to cause single-amplitude shear strain of 3% for D_R = 35, 55, and 75% with vertical effective consolidation stresses of 100 kPa and initial static shear stress ratios of 0.0, 0.1, 0.2, and 0.3.

95

Figure 4.10. Effect of vertical effective consolidation stresses of 100 and 400 kPa on the variation of cyclic resistance ratio (a and b) (peak shear strain of 3% in 15 uniform cycles in DSS loading) and on the K_α factor (c and d) for sand at D_R of 35, 55, and 75% with initial static shear stress ratios of 0.0, 0.1, 0.2, and 0.3.
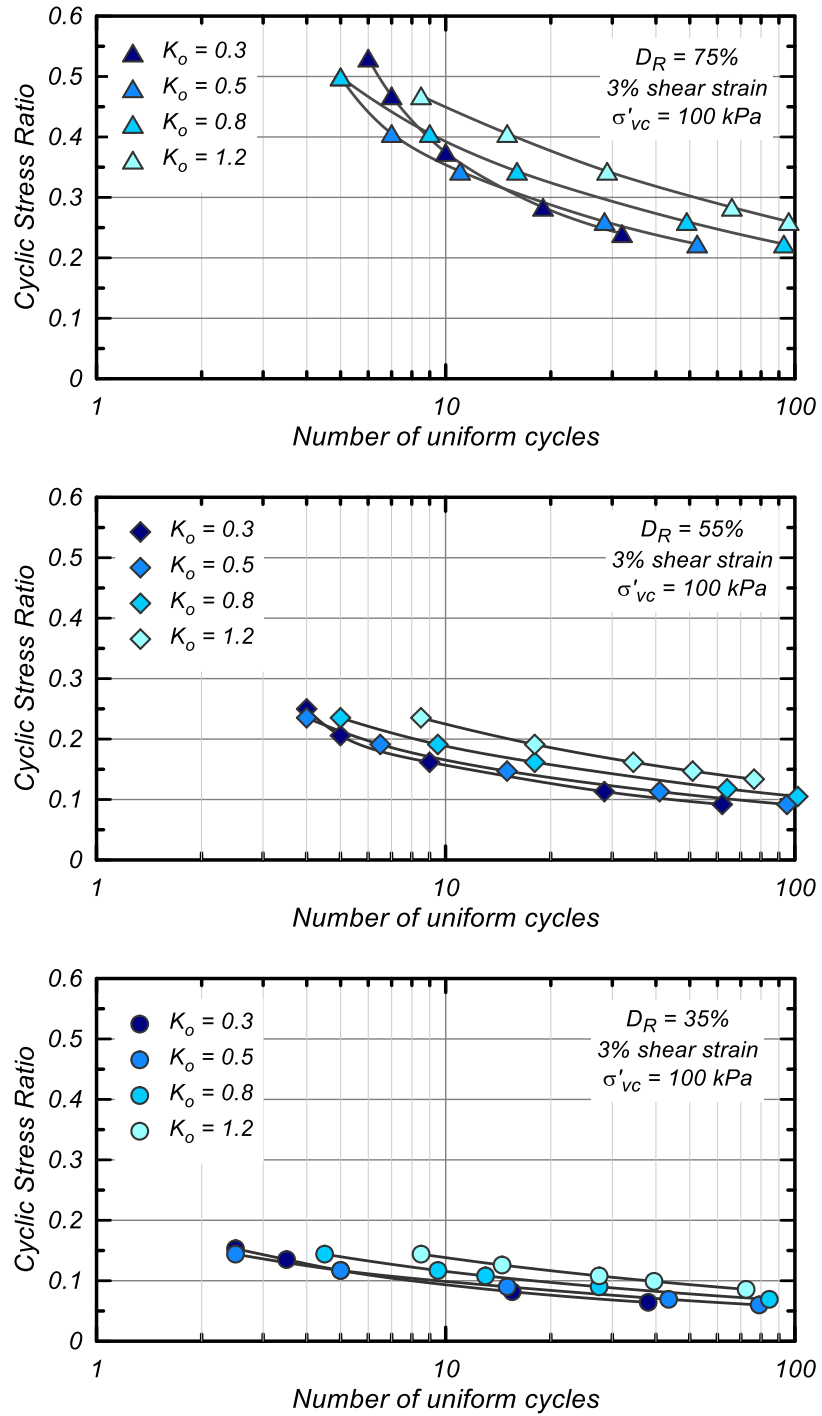
Figure 4.11. Cyclic stress ratios versus number of equivalent uniform loading cycles in undrained DSS loading to cause single-amplitude shear strain of 3% for $D_R = 35$, 55, and 75% with vertical effective consolidation stresses of 100 kPa and initial K_o values of 0.3, 0.5, 0.8, and 1.2.
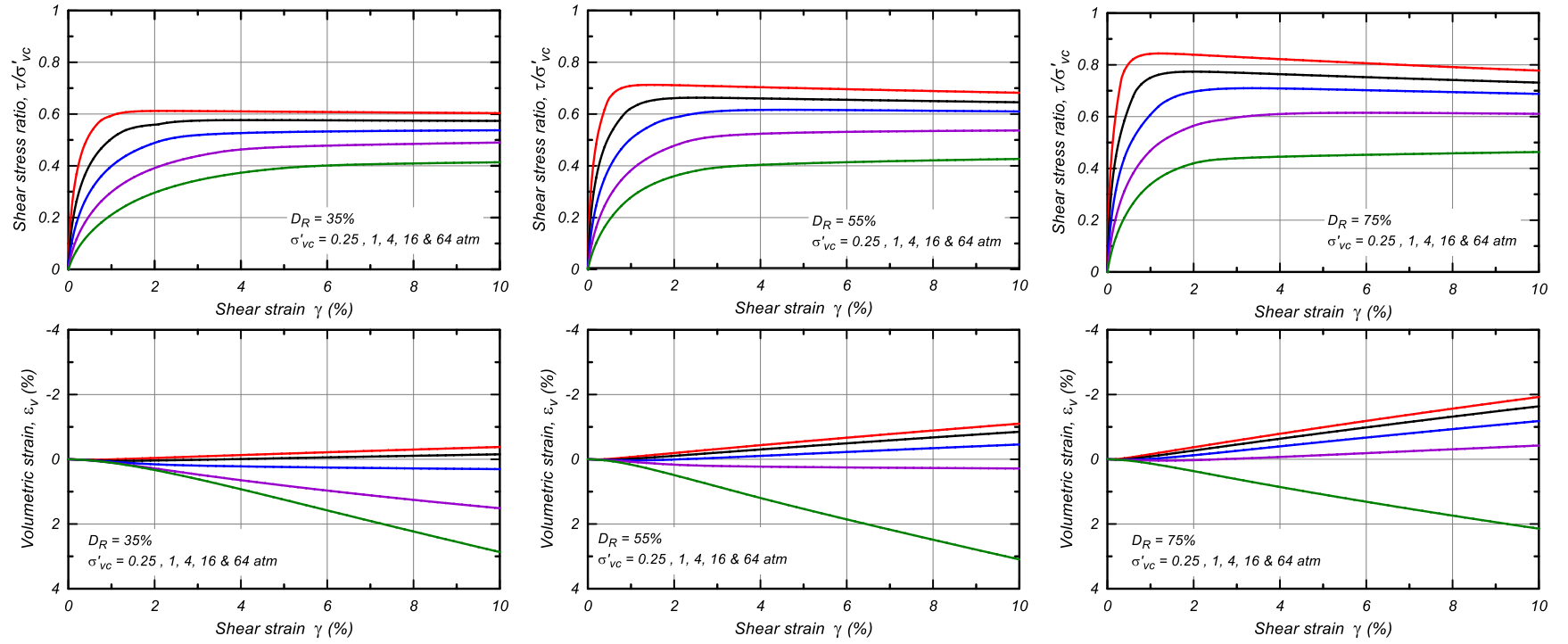
Figure 4.12. Drained monotonic DSS loading responses for D_R = 35, 55, and 75% with vertical effective confining stresses of ¼, 1, 4, 16, and 64 atm and K_o=0.5.
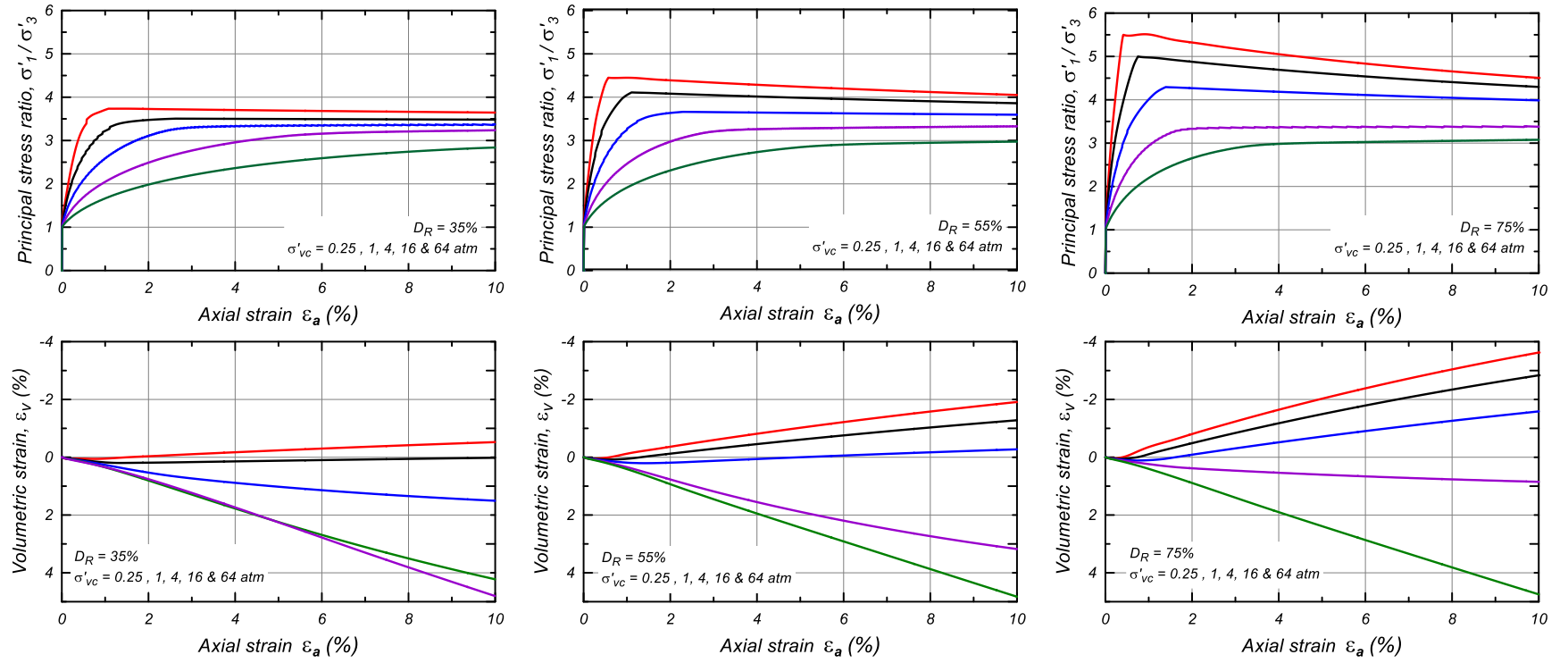
Figure 4.13. Drained monotonic PSC (plane strain compression) loading responses for D_R = 35, 55, and 75% with initial isotropic confining stresses of ¼, 1, 4, 16, and 64 atm.
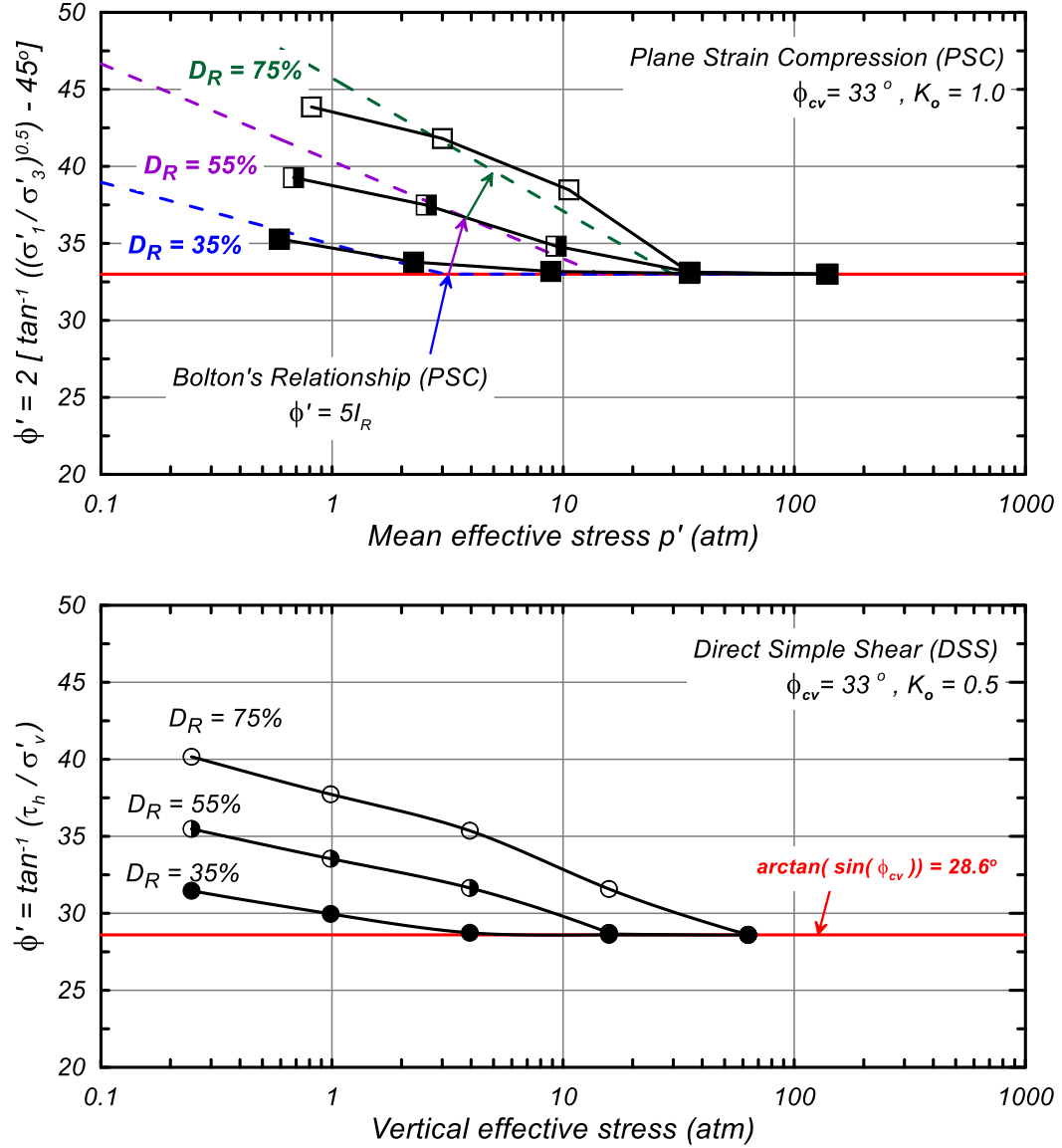
Figure 4.14. Peak friction angles from drained monotonic PSC and DSS loading responses for D_R = 35, 55, and 75% under effective confining stresses of ¼, 1, 4, 16, and 64 atm. For DSS loading, the friction angle is presented using the conventional interpretations that the horizontal plane is the failure plane (the actual plane of peak stress ratio is not horizontal in these simulations).

Figure 4.15. Undrained monotonic DSS loading responses for D_R = 35, 55, and 75% under vertical effective consolidation stresses of ¼, 1, 4, and 16 atm.
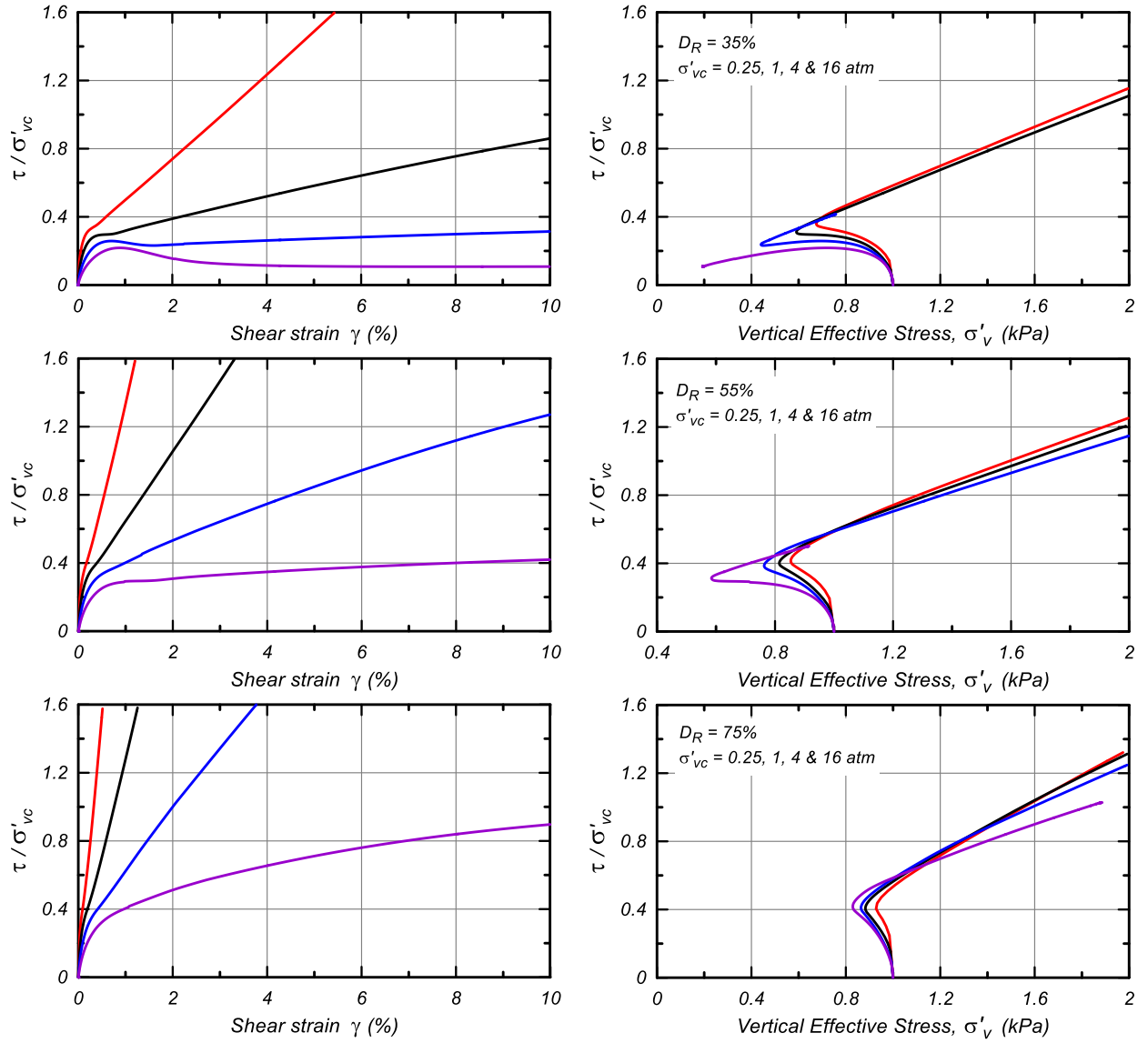
Figure 4.16. Normalized responses to undrained monotonic DSS loading for D$_R$ = 35, 55, and 75% under vertical effective consolidation stresses of ¼, 1, 4, and 16 atm.
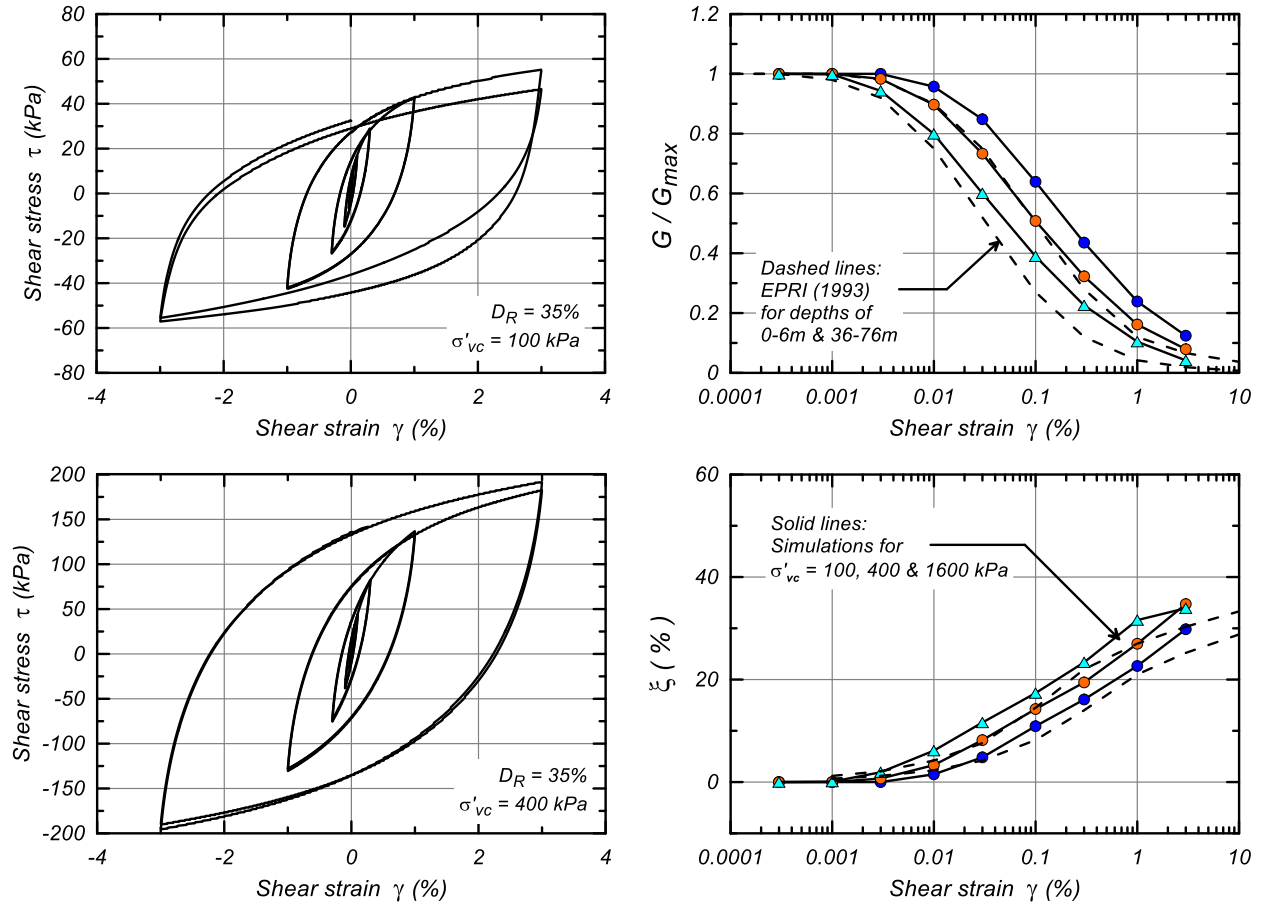
Figure 4.17. Drained strain-controlled cyclic DSS loading responses for $D_R = 35\%$ under vertical effective consolidation stresses of 1, 4, and 16 atm.
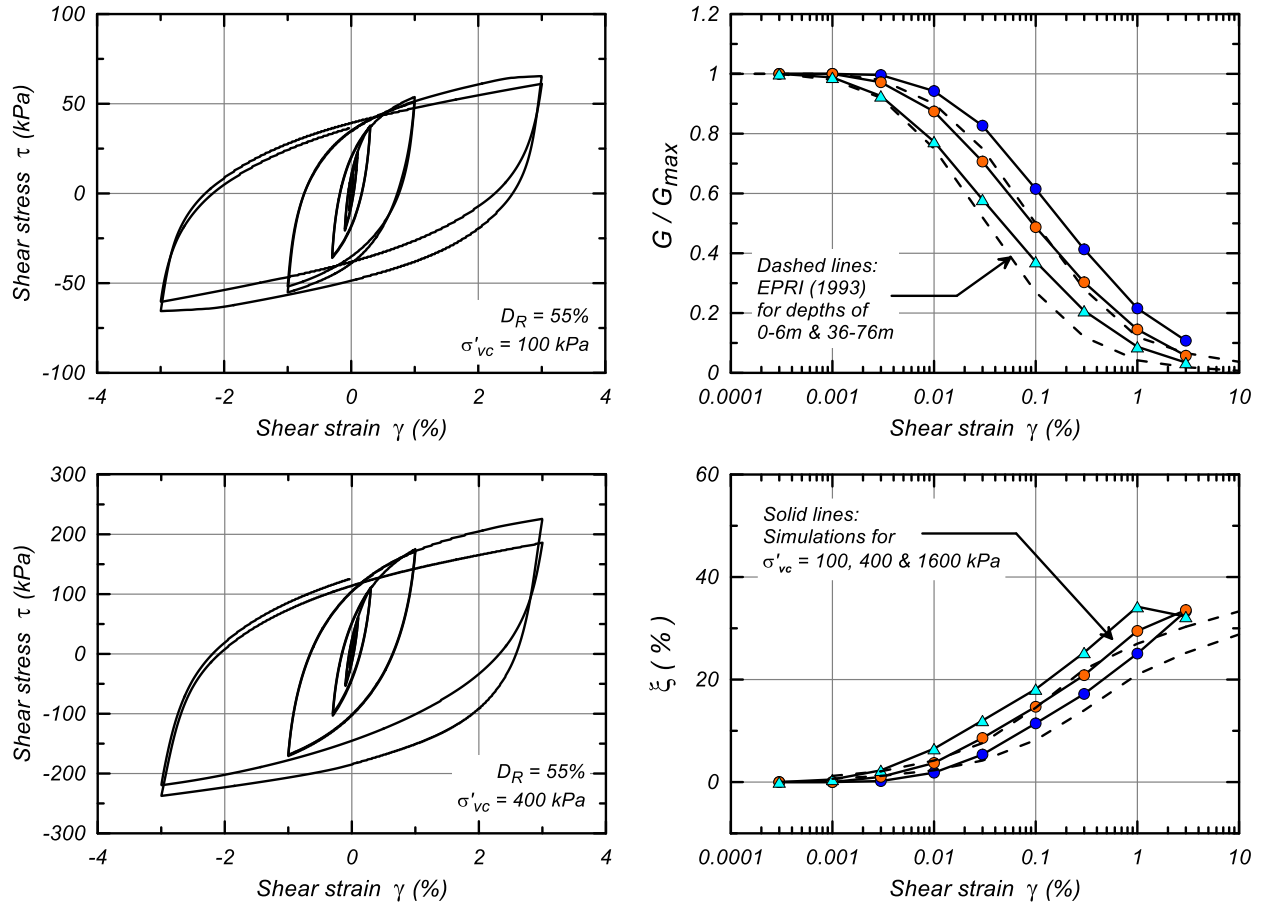
Figure 4.18. Drained strain-controlled cyclic DSS loading responses for $D_R = 55\%$ under vertical effective consolidation stresses of 1, 4, and 16 atm.
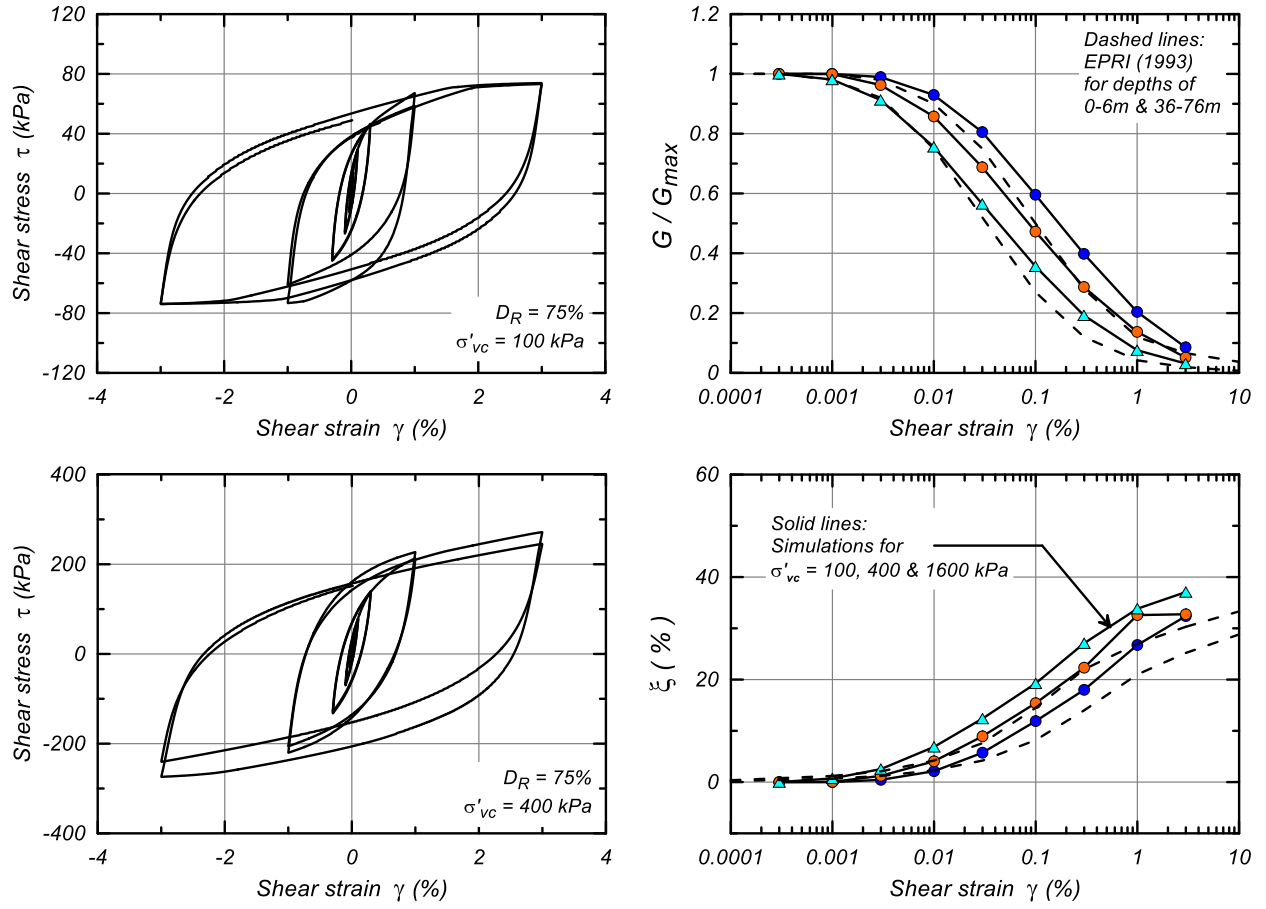
Figure 4.19. Drained strain-controlled cyclic DSS loading responses for $D_R = 75\%$ under vertical effective consolidation stresses of 1, 4, and 16 atm.
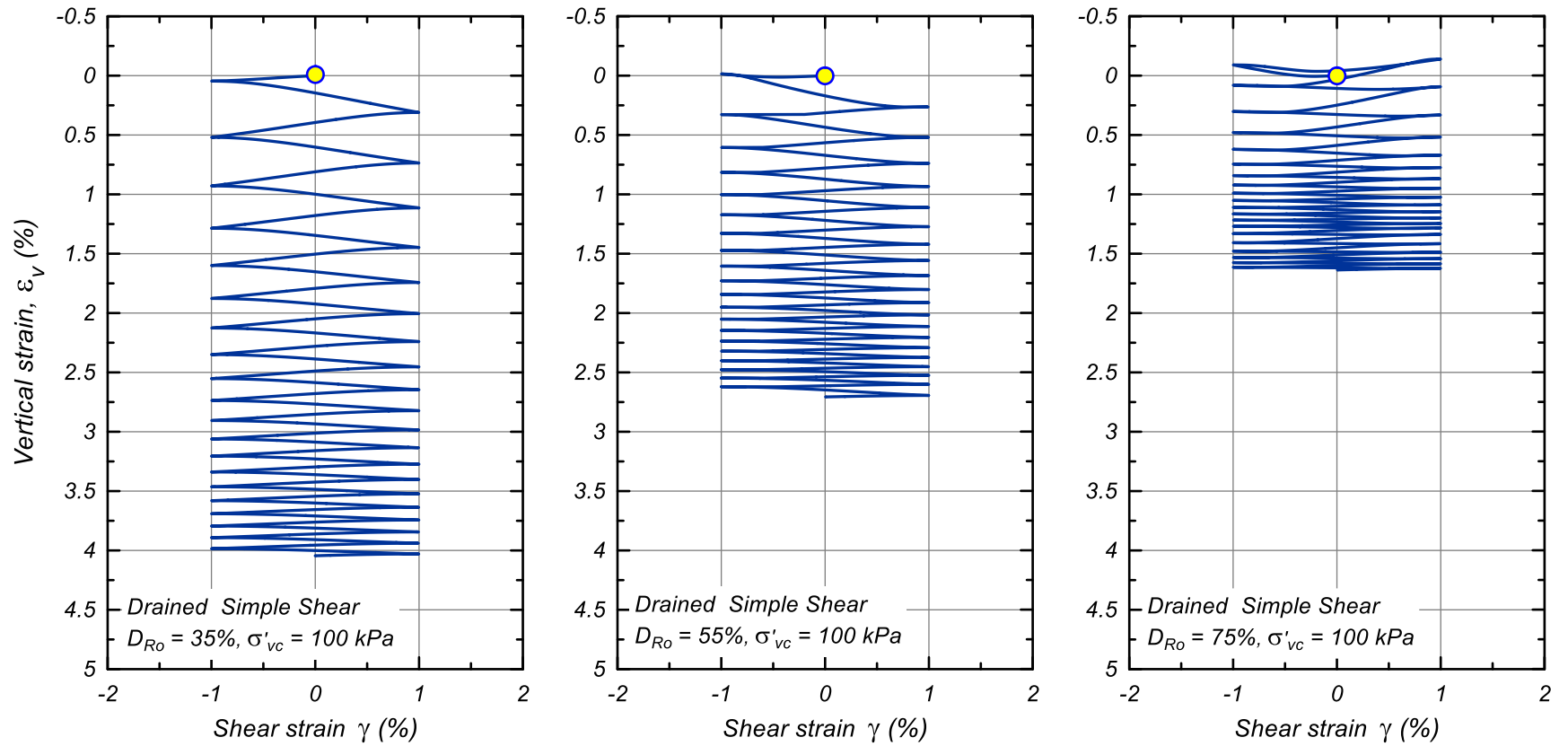
Figure 4.20. Volumetric strains during drained strain-controlled cyclic DSS loading for D_R = 35, 55, and 75% with a vertical effective consolidation stress of 100 kPa.

.
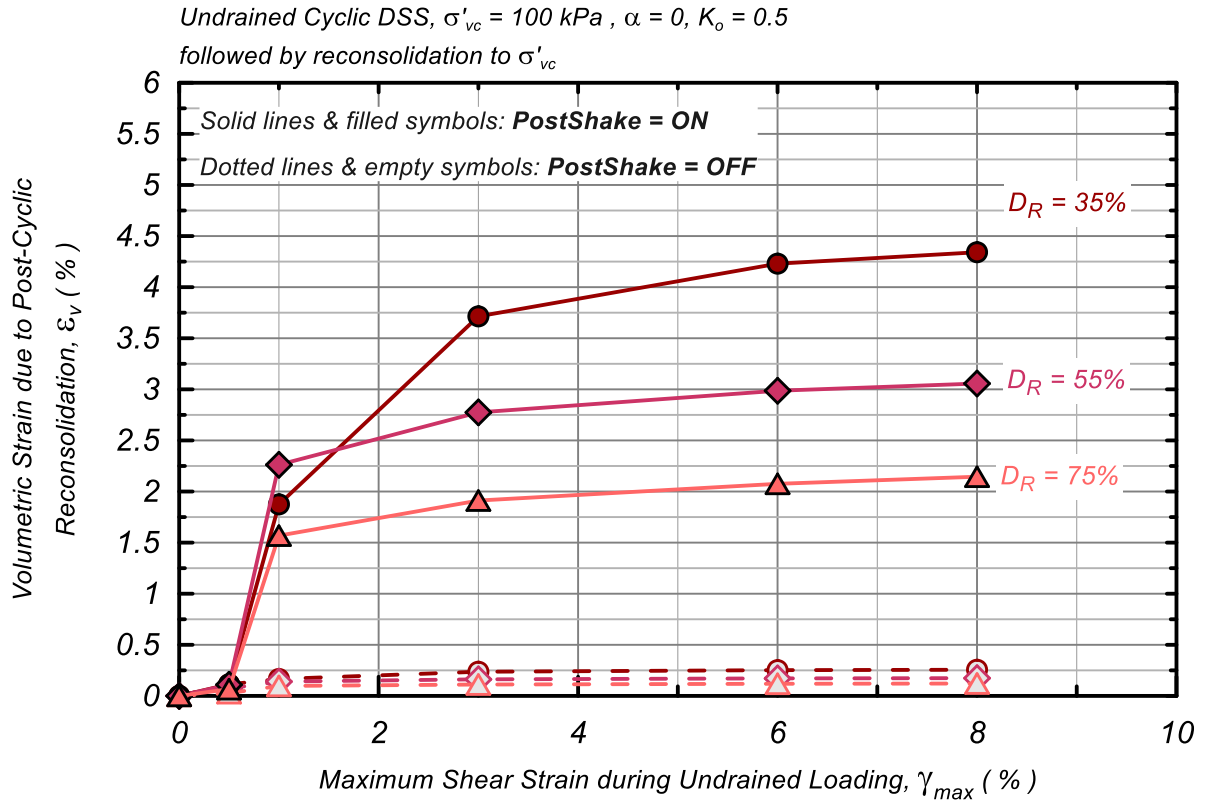
Figure 4.21. Volumetric strain due to post-cyclic reconsolidation versus the maximum shear strain induced during undrained cyclic DSS loading.
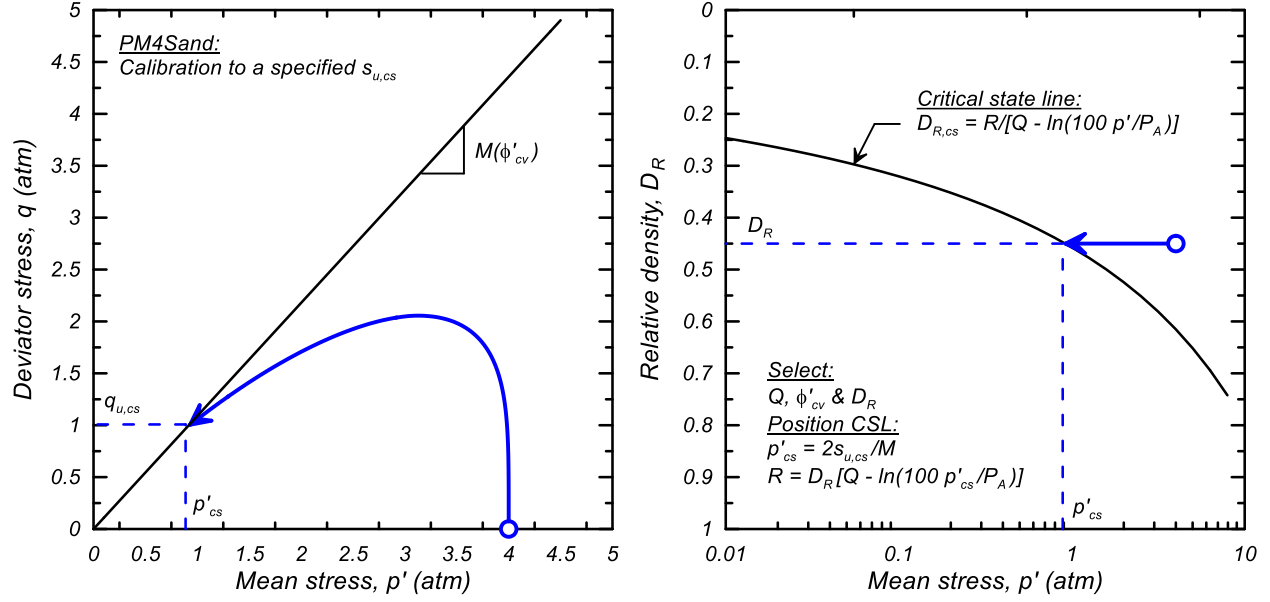
Figure 4.22. Calibrating PM4Sand to a specified undrained critical state shear strength by adjusting R (Boulanger and Ziotopoulou 2018)
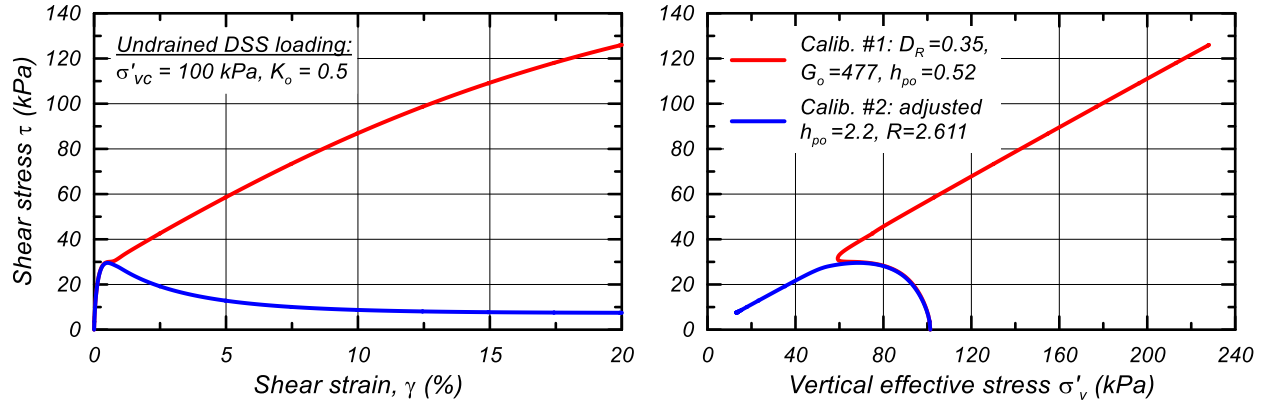
Figure 4.23. Monotonic undrained DSS responses for $D_R = 35\%$ two calibrations: Calibration 1 with defaults for all secondary parameters, and Calibration 2 with R based on $s_{u,cs} = 7$ kPa.
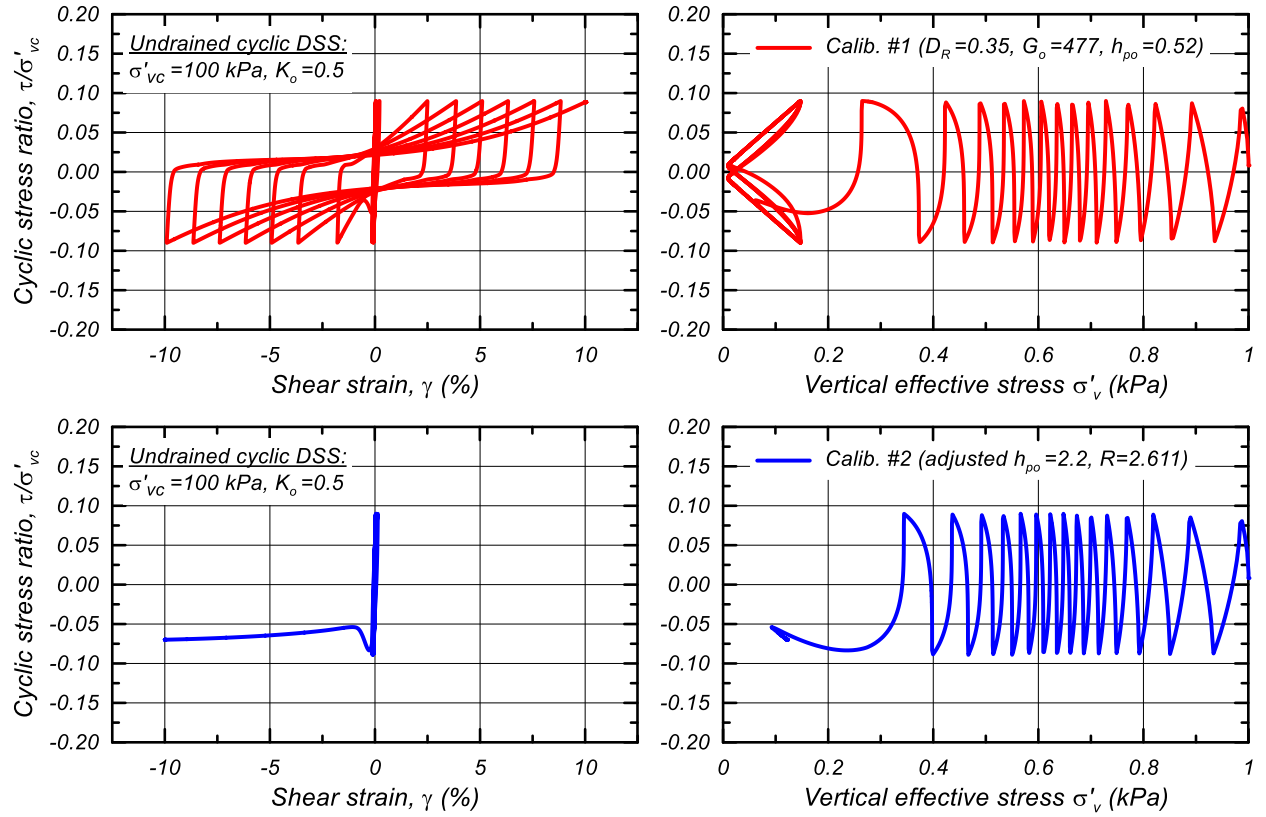
Figure 4.24.   Cyclic undrained DSS response for $D_R = 35\%$ at CSR = 0.09 for (1) Calibration 1 with default values for all secondary parameters, and (2) Calibration 2 with R based on $s_{u,cs} = 7$ kPa.

5. CONCLUDING REMARKS

The PM4Sand (Version 3.3) plasticity model presented herein is built upon the basic framework of the stress ratio-controlled, critical state-based, bounding surface plasticity model for sand presented by Dafalias and Manzari (2004). A series of modifications and additions to the model were incorporated by Boulanger (2010; Version 1), Boulanger and Ziotopoulou (2012 Version 2; 2015 Version 3; 2017 Version 3.1, 2023 Version 3.2) and further herein (Version 3.3) to improve its ability to approximate the stress-strain responses important to geotechnical earthquake engineering practice; in essence, the model was calibrated at the equation level to provide for better approximation of the trends observed in empirical correlations commonly used in practice. These constitutive modifications included:

- revising the fabric formation/destruction to depend on plastic shear rather than plastic volumetric strains;
- adding fabric history and cumulative fabric formation terms;
- modifying the plastic modulus relationship and making it dependent on fabric;
- modifying the dilatancy relationships to include dependence on fabric and fabric history, and provide more distinct control of volumetric contraction versus expansion behavior;
- providing a constraint on the dilatancy during volumetric expansion so that it is consistent with Bolton's (1986) dilatancy relationship;
- modifying the elastic modulus relationship to include dependence on stress ratio and fabric history;
- modifying the logic for tracking the initial back-stress ratio history;
- recasting the critical state framework to be in terms of a relative state parameter index;
- simplifying the formulation by restraining it to plane strain without Lode angle dependency for the bounding and dilatancy surfaces;
- incorporating a methodology for improved modeling of post-liquefaction reconsolidation strains; and
- providing default values for all but three primary input parameters.

The model (Version 3.3) was implemented as a user defined material in DLLs for use with the commercial programs FLAC 8.1 (Itasca 2019) and FLAC2D 9.00 (Itasca 2023).

The three primary model input properties are: an apparent D_R which affects the peak drained and undrained strengths and the rate of strain accumulation during cyclic loading; the shear modulus coefficient, G_o, which should be calibrated to the estimated or measured in-situ shear wave velocity; and the contraction rate parameter, h_{po} which is used to calibrate to the estimated in-situ cyclic resistance ratio after all other properties have been set.

The behavior of the model was illustrated by simulations of element loading tests covering a broad range of conditions, including drained and undrained, cyclic and monotonic loading under a range of initial relative densities, confining stresses, and initial shear stress conditions. The current formulation is limited to plane strain applications. Simulations presented in this report were completed using the dynamic link library (DLL) version *modelpm4sand005_64.dll* compiled on June 12, 2023 compatible with FLAC 8.1. The use of the DLL module *cmodelPM4Sand2D009.dll* compiled on June 12, 2023 in FLAC2D 9.00 showed that the results remain unaffected. The model

was shown to provide reasonable approximations of desired behaviors and to be relatively easy to calibrate.

ACKNOWLEDGMENTS

REFERENCES

Andrianopoulos, K.I., Papadimitriou, A.G., and Bouckovalas, G.D. (2009). "Explicit integration of bounding surface model for the analysis of earthquake soil liquefaction." International J. of Numerical and Analytical Methods in Geomechanics, DOI 10.1002/nag.875.

Andrus, R.D., and Stokoe, K.H. (2000). "Liquefaction resistance of soils from shear-wave velocity." J. Geotechnical and Geoenvironmental Eng., ASCE 126(11), 1015–025.

Arai, H. (2006). "Detection of subsurface V_s recovery process using microtremor and weak ground motion records in Ojiya, Japan." Third International Conference on Urban Earthquake Engineering, Tokyo Institute of Technology, Tokyo, Japan.

Beaty, M. (2009). "Summary of UBCSand Constitutive Model: Versions 904a and 904aR." Short Course on Seismic Deformation Analyses of Embankment Dams Considering Liquefaction Effects, September 22-24, 2009, Davis, California.

Been, K., and Jefferies, M. G. (1985). "A state parameter for sands." Géotechnique 35(2), 99–112.

Bolton, M. D. (1986). "The strength and dilatancy of sands." Géotechnique 36(1), 65–78.

Boulanger, R. W. (2022). "Nonlinear dynamic analyses involving soil liquefaction or cyclic softening." Proceedings, 20th ICSMGE State of the Art and Invited Lectures, Rahman and Jaksa (eds), Australian Geomechanics Society, Sydney, Australia, ISBN 978-0-9946261-6-5, 351-379.

Boulanger, R. W. (2010). "A sand plasticity model for earthquake engineering applications." Report No. UCD/CGM-10-01, Center for Geotechnical Modeling, Department of Civil and Environmental Engineering, University of California, Davis, CA, 77 pp.

Boulanger, R. W., (2003a). "Relating K_α to relative state parameter index." J. Geotechnical and Geoenvironmental Eng., ASCE 129(8), 770–73.

Boulanger, R. W. (2003b). "High overburden stress effects in liquefaction analyses." J. Geotechnical and Geoenvironmental Eng., ASCE 129(12), 1071–082.

Boulanger, R.W., and Beaty, M.H. (2016). Seismic deformation analyses of embankment dams: A reviewer's checklist. Proceedings, Celebrating the Value of Dams and Levees – Yesterday, Today and Tomorrow, 36th USSD Annual Meeting and Conference, United States Society on Dams, Denver, CO, 535-546.

Boulanger, R. W., and Idriss, I. M. (2004). "State normalization of penetration resistances and the effect of overburden stress on liquefaction resistance." Proc., 11th Intl. Conf. on Soil Dynamics and Earthquake Engineering, and 3rd Intl. Conf. on Earthquake Geotechnical Engineering, Doolin et al., eds, Stallion Press, Vol. 2, pp. 484-491.

Boulanger, R. W., and Idriss, I. M. (2011). "Cyclic failure and liquefaction: Current issues." 5th International Conference on Earthquake Geotechnical Engineering, Santiago, Chile, Jan 10-13.

Boulanger, R. W., Kamai, R., and Ziotopoulou, K. (2011). "Numerical modeling of liquefaction effects." Proc., Effects of Surface Geology on Seismic Motion, 4th IASPEI / IAEE International Symposium, August 23-26, University of California, Santa Barbara, CA.

Boulanger, R. W., Kamai, R., and Ziotopoulou, K. (2014). "Liquefaction induced strength loss and deformation: Simulation and design." Bulletin of Earthquake Engineering, Springer, 12: 1107-1128, DOI 10.1007/s10518-013-9549-x.

Boulanger, R. W., Montgomery, J., and Ziotopoulou, K. (2015). "Nonlinear deformation analyses of liquefaction effects on embankment dams." Perspectives on Earthquake Geotechnical Engineering, A. Ansal and M. Sakr, eds., Geotechnical, Geological and Earthquake Engineering 37, 247-283, Springer, DOI 10.1007/978-3-319-10786-8_10.

Boulanger, R. W., and Ziotopoulou, K. (2013). "Formulation of a sand plasticity plane-strain model for earthquake engineering applications." Journal of Soil Dynamics and Earthquake Engineering, Elsevier, 53, 254-267, 10.1016/j.soildyn.2013.07.006.

Boulanger, R.W., and Ziotopoulou, K. (2018). "On NDA practices for evaluating liquefaction effects." Proc., Geotechnical Earthquake Engineering and Soil Dynamics V, Geotechnical Special Publication 290, S. J. Brandenberg and M. T. Manzari, eds., ASCE, 1-20.

Byrne, P. M., Park, S. S., Beaty, M., Sharp, M., Gonzalez, L., Abdoun, T. 2004. "Numerical modeling of liquefaction and comparison with centrifuge tests." Canadian Geotechnical Journal. 41 (2): 193-211.

Cubrinovski, M., and Ishihara, K. (1998). "State concept and modified elastoplasticity for sand modelling." Soils and Foundations; 38(4): 213-225.

Dafalias, Y. F. (1986). "Bounding surface plasticity. I: Mathematical foundation and hypoplasticity." J. Engineering Mechanics, 112(9), 966-987.

Dafalias, Y. F., and Manzari, M. T. (2004). "Simple plasticity sand model accounting for fabric change effects." Journal of Engineering Mechanics, ASCE, 130(6), 622-634.

Dawson, E. M., W. H. Roth, S. Nesarajah, G. Bureau, and C. A. Davis. (2001). "A practice oriented pore pressure generation model." Proceedings, 2nd FLAC Symposium on Numerical Modeling in Geomechanics. Oct. 29-31, Lyon, France.

Desrues, J., Chambon, R., Mokni, M., and Mazerolle, F. (1996). "Void ratio evolution inside shear bands in triaxial sand specimens studied by computed tomography." Géotechnique, 46(3), 529–546.

Duku, P. M., Stewart, J. P., and Whang, D. H. (2008). "Volumetric strains of clean sands subject to cyclic loads." J. Geotechnical and Geoenvironmental Eng., ASCE, 134(8), 1073-1085.

Electric Power Research Institute (1993). Guidelines for site specific ground motions, Rept. TR-102293, 1-5, Pala Alto, California.

Howell, R., Rathje, E. M., and Boulanger, R. W. (2014). "Evaluation of simulation models of lateral spread sites treated with prefabricated vertical drains." Journal of Geotechnical and Geoenvironmental Engineering, ASCE, 04014076, 10.1061/(ASCE)GT.1943-5606.0001185.

Idriss, I. M., and Boulanger, R. W. (2006). "Semi-empirical procedures for evaluating liquefaction potential during earthquakes." J. Soil Dynamics and Earthquake Eng. 26, 115–30.

Idriss, I. M., and Boulanger, R. W. (2008). Soil liquefaction during earthquakes. Monograph MNO-12, Earthquake Engineering Research Institute, Oakland, CA, 261 pp.

Idriss, I. M., and Boulanger, R. W. (2010). "SPT-based liquefaction triggering procedures." Report UCD/CGM-10/02, Department of Civil and Environmental Engineering, University of California, Davis, CA, 259 pp.

Ishihara, K. (1993). "Liquefaction and flow failure during earthquakes." Géotechnique 43(3), 351–415.

Ishihara, K., and Yoshimine, M. (1992). "Evaluation of settlements in sand deposits following liquefaction during earthquakes." Soils and Foundations 32(1), 173–88.

Itasca (2019). FLAC – Fast Lagrangian Analysis of Continua, Version 8.1, Itasca Consulting Group, Inc., Minneapolis, Minnesota.

Itasca (2023). FLAC2D – Fast Lagrangian Analysis of Continua, Version 9.00, Itasca Consulting Group, Inc., Minneapolis, Minnesota.

Kamai, R. (2011). "Liquefaction-induced shear strain localization processes in layered soil profiles". PhD dissertation, University of California, Davis, 259pp.

Kamai, R. and Boulanger, R. W. (2012). "Single-element simulations of partial-drainage effects under monotonic and cyclic loading." Journal of Soil Dynamics and Earthquake Engineering, 35, 29-40.

Khosravifar, A., Elgamal, A., Lu, J., and Li, J. (2018). "A 3D model for earthquake-induced liquefaction triggering and post-liquefaction response." Soil Dynamics and Earthquake Engineering, 110: 43-52.

Konrad, J.-M. (1988). "Interpretation of flat plate dilatometer tests in sands in terms of the state parameter." Géotechnique 38(2), 263–77.

Kulhawy, F. H., and Mayne, P. W., 1990. Manual on Estimating Soil Properties for Foundation Design, Report EPRI EL-6800, Electric Power Research Institute, Palo Alto, CA.

Kutter, B. L., and Chen, Y.-R. (1997). "Constant p' and constant volume friction angles are different." ASTM Geotechnical Testing Journal, ASTM, 20(3), 304-316.

Lee, K. L., and Seed, H. B. (1967). "Drained strength characteristics of sands." J. Soil Mechanics and Foundations Div., ASCE 93(SM6), 117–41.

Li, X. S., and Wang, Y. (1998). "Linear representation of steady-state line for sand." J. Geotechnical and Geoenvironmental Engineering, 124(12), 1215-1217.

Liu, H.Y., Abell, J.A., Diambra, A., and Pisano, F. (2020). "Memory-enhanced plasticity modeling of sand behavior under undrained cyclic loading." Journal of Geotechnical and Geoenvironmental Engineering, 146(11): 04020122, 10.1061/(ASCE)GT.1943-5606.0002362.

Manzari, M. T., and Dafalias, Y. F. (1997). "A critical state two-surface plasticity model for sand." Géotechnique, 47(2), 255-272.

Marti, J. and Cundall, P.A. (1982). "Mixed discretization procedure for accurate solution of plasticity problems." Int. J. Num. Methods and Anal. Methods in Geomechanics, 6, 129-139.

Matsuya, A., Kazama, M., Sento, N. and Uzuoka, R. (2004). "Effect of initial shear stress on reconsolidation characteristics of sand subjected undrained cyclic shear." The Japanese Geotechnical Engineering Society, Proceedings of the 39th Japan National Conference on Geotechnical Engineering, pp. 497-498, July (in Japanese)

Papadimitriou, A. G., Bouckovalas, G. D., and Dafalias, Y. F. (2001). "Plasticity model for sand under small and large cyclic strains." J. Geotechnical and Geoenvironmental Engineering, 127(11), 973-983.

Richart, F. E., Jr., Hall, J. R., and Woods, R. D. (1970). "Vibration of soils and foundations." International series in theoretical and applied mechanics, Prentice-Hall, Englewood Cliffs, N.J.

Rowe, P. W. (1962). "The stress-dilatancy relation for static equilibrium of an assembly of particles in contact." Proc. R. Soc. London, Ser. A, 269, 500-527.

Sadrekamiri, A, and Olson, S. A. (2010). "Shear band formation observed in ring shear tests on sandy soils." J. Geotechnical and Geoenvironmental Engineering, ASCE, 366-375.

Schofield, A. N., and Wroth, C. P. (1968). Critical state soil mechanics, McGraw-Hill, New York.

Silver, M. L., and Seed, H. B. (1971). "Volume changes in sand during cyclic loading." J. Soil Mechanics and Foundations Div., ASCE 97(SM9), 1171–182.

Tasiopoulou, P., and Gerolymos, N. (2016). "Constitutive modeling of sand: Formulation of a new plasticity approach." Soil Dynamics and Earthquake Engineering, 82:205-221.

Wang, Z. L., Dafalias, Y. F., and Shen, C. K. (1990). "Bounding surface hypoplasticity model for sand." J. Engineering Mechanics, ASCE, 116(5), 983-1001.

Yang, M., Taiebat, M., Dafalias, Y. (2022). "SANISAND-MSf: a memory surface and semifluidized state enhanced sand plasticity model for undrained cyclic shearing." Géotechnique, 10.1680/jgeot.19.P.363

Yang, Z., A. Elgamal and E. Parra, (2003). "Computational model for cyclic mobility and associated shear deformation." J. Geotechnical and Geoenvironmental Engineering, ASCE, 129(12), 1119-1127.

Yoshimine, M., Robertson, P. K., and Wride, C. E. (1999). "Undrained shear strength of clean sands to trigger flow liquefaction." Canadian Geotechnical Journal, 36, 891-906.

Youd, T. L. (1972). "Compaction of sands by repeated straining." J. Soil Mechanics and Foundations Div., ASCE 98(SM7), 709–25.

Yu, P., and Richart, F. E., Jr. (1984). "Stress ratio effects on shear modulus of dry sands." J. Geotechnical Engineering, ASCE, 110(3), 331-345.

Ziotopoulou, K. (2010). "Evaluating model uncertainty against strong motion records at liquefiable sites", Masters thesis, University of California, Davis, 294pp.

Ziotopoulou, K., Boulanger, R. W., and Kramer, S. L. (2012). "Site response analyses of liquefying sites." Geo-Congress 2012: State of the Art and Practice in Geotechnical Engineering, R. D. Hryciw, A. Athanasopoulos-Zekkos, and N. Yesiller, eds., Geotechnical Special Publication No. 225, ASCE Geo-Institute, 1799-1808.

Ziotopoulou, K., and Boulanger, R. W. (2012). "Constitutive modeling of duration and overburden effects in liquefaction evaluations." Proc., Second International Conference on Performance-based Design in Earthquake Geotechnical Engineering, Taormina, Italy, May 28-30, paper 03.10.

Ziotopoulou, K., and Boulanger, R. W. (2013a). "Calibration and implementation of a sand plasticity plane-strain model for earthquake engineering applications." Journal of Soil Dynamics and Earthquake Engineering, 53, 268-280, 10.1016/j.soildyn.2013.07.009.

Ziotopoulou, K., and Boulanger, R. W. (2013b). "Numerical modeling issues in predicting post-liquefaction reconsolidation strains and settlements." 10th International Conference on Urban Earthquake Engineering, March 1-2, Tokyo Institute of Technology, Tokyo, Japan, 469-475.

Ziotopoulou, K., and Boulanger, R. W. (2016). "Plasticity modeling of liquefaction effects under sloping ground and irregular cyclic loading conditions." Soil Dynamics and Earthquake Engineering, 84 (2016), 269-283, 10.1016/j.soildyn.2016.02.013.

Ziotopoulou, K. (2014). "A sand plasticity model for earthquake engineering applications." PhD Dissertation, University of California, Davis.